The Application of Ionic Solutions of Graphene for the Synthesis of a Novel Platinum-Graphene Catalyst for the Oxygen Reduction Reaction for Hydrogen Fuel Cells

Gyen Ming Anthony Angel

Department of Chemical Engineering

UCL

A thesis submitted in partial fulfilment of the requirements of

University College London
for the award of

Doctor of Philosophy

30/08/2022

Declaration

I, Gyen Ming A. Angel, confirm that the work presented in this thesis is my own. Where information has been derived from other sources, I confirm that this has been indicated in the thesis.

Gyen Ming Anthony Angel

30/08/2022

Date

Acknowledgements

I would like to thank my supervisors Professor Dan Brett, Professor Paul Shearing and Professor Chris Howard for their support, advice and encouragement throughout this project. Special thanks go to Dr Patrick Cullen, with whom I started this work as an undergraduate summer project student in 2016; without his continued efforts, help and guidance this work would not have been possible. I would also like to thank Hector Lancaster and Dr Theo Suter for their assistance in the lab and in the analysis of some of the data presented in this thesis.

Thanks to all the colleagues I have worked and collaborated with over the last six years as part of the EIL and the CMMP groups. I owe special thanks to my friends in the F10a office: Becky Shutt, Ami Shah, Eva Aw, Hector Lancaster, Katrina Mazloomian, Kashim Bin Subhan, Fengfei Zhang and Zahra Rana. I would also like to thank my two undergraduate summer project students, Alex Marinov and Lara Seemungal.

Most of all, I would like to thank Izzie and my family for their steadfast support across the whole of this journey.

Abstract

Hydrogen fuel cells are a promising energy conversion technology, and a key part of the future green hydrogen economy required as part of the transition from fossil fuels to a more sustainable future. Fuel cells efficiently convert chemical energy to electricity without producing carbon dioxide emissions, making them candidates for the decarbonisation of a variety of applications including transport, heating, and power generation. The cost and durability of platinum fuel cell catalysts remain a barrier to the widespread commercial deployment of hydrogen fuel cells. Although optimising these properties has been the focus of decades of research, cost and performance targets set out by the US Department of Energy have not changed for many years and have yet to be met.

In this thesis, a novel, scalable method for the synthesis of a platinum nanoparticle catalyst supported by high-quality graphene is presented. The catalyst has been characterised with a range of techniques and its activity toward the oxygen reduction reaction has been measured using half-cell techniques. Its durability was assessed using accelerated stress tests following adapted US DoE protocols, the results of which showed that the novel graphene-supported catalyst far out-performed a state-of-the-art commercial platinum catalyst. The method was then improved upon to facilitate the scale up of the quantity of catalyst produced, and the resultant material was characterised and assessed as part of a membrane electrode assembly within a full hydrogen fuel cell.

Beyond fuel cell catalysts, this work demonstrates the first practical application of ionic solutions of two-dimensional materials, first reported by Cullen *et al., (*Nature Chemistry, 2016). As such, it lays the foundation for the use of ionic solutions of two-dimensional materials for a wide range of applications that require high-quality nanomaterials decorated with nanoparticles.

Impact Statement

Anthropomorphic climate change is the single largest issue of the 21st century, with fossil fuel emissions predicted to increase global average temperatures by as much as 4 °C, resulting in catastrophic effects on human civilisation and global ecosystems alike. The pressing need to reduce fossil fuel emissions has been outlined in many large-scale reports that represent the culmination of decades of science, and international agreements such as the 2015 Paris Agreement show there is the political will to enact change.

Despite these efforts and agreements, fossil fuel emissions are still increasing year-on-year and new technologies must be rapidly implemented at scale if there is to be a chance to limit global temperature increases to 1.5 °C, as set out by the Paris Agreement. Hydrogen is recognised as an important part of the transition away from fossil fuels, both in its use within industrial processes in place of natural gas, and as a method to store renewable energy that is produced intermittently. In principle, energy storage is achieved by using renewable electricity to power water electrolysers, which produce "green" hydrogen (produced without the need for fossil fuels). The hydrogen can then be transported and stored, and when the energy is required a fuel cell is employed to directly convert the chemical energy to electrical energy with water as the only by-product.

Hydrogen fuel cells are already in commercial use across a number of applications, including transport, stationary power and heating, but are limited by their high costs and a need for improved lifetimes. A key component in both the cost and lifetime of a hydrogen fuel cell is the catalyst, which is a high surface area amorphous carbon material decorated with platinum nanoparticles. Many years of research have been dedicated to improving the durability and platinum utilisation of these catalysts.

In this thesis, a novel, scalable method is presented to produce a catalyst for hydrogen fuel cells which makes use of graphene in place of traditionally-used carbons. The graphene-based platinum catalyst is shown to be highly durable under accelerated stress tests, with the results published and the

method patented, meaning that it could be licensed for scaled-up manufacturing by a UCL-backed start-up or by an existing company, leading to a potential improvement in fuel cell technology.

Beyond its application in catalysts for fuel cells, the work presented in this thesis shows that solutions of negatively charged 2D materials can directly reduce metal salts in a scalable fashion, which could be employed across a range of uses. These include other novel catalysts, such as those used in water electrolysis and Zn-air batteries, but also in the production of electrode materials for batteries and supercapacitors. Work is ongoing within our group to explore these applications with some exciting preliminary results.

Table of Contents

List of Figures

List of Tables

Chapter 1: Introduction

This chapter briefly introduces the problem of anthropogenic climate change driven by the burning of fossil fuels, and the role of hydrogen as a fuel in a transition away from fossil fuels. An overview of the hydrogen fuel cell is then presented, followed by an overview and outline of the thesis.

1.1 Motivation

For more than the last one hundred and fifty years, human development has been driven by the ability to derive large amounts of energy from the burning of fossil fuels.[1] Essential in providing the source of electricity and heat used in every aspect of modern life, fossil fuels continue to be the world's primary energy source.[2,3] However, burning fossil fuels produces carbon dioxide and other contaminants, which has led to unprecedented changes in the Earth's atmosphere, resulting in major, damaging changes to the Earth's climate system.[4] With both the planet's population and its energy demands growing rapidly, it is estimated that more than 50% more energy will be required[2] in 2035 than was used in 2009, and as such modern renewable energy solutions must be greatly improved upon in order to meet the demands of a sustainable future.

1.2 Hydrogen as a fuel

Hydrogen fuel represents a promising part of the solution to the world's growing energy challenge. As the population moves from a reliance on fossil fuels to renewable energy sources[5], as shown in Table 1-1, there will also be a greater need for energy storage and conversion in order to compensate for the intermittent nature of sources such as wind and solar power.

Table 1-1 *Past and projected global renewable energy consumption, adapted from [5].*

	2001	2010	2020	2030
Total consumption (million tons oil equivalent)	10,038	10,549	11,425	12,352
Biomass	1080	1313	1791	2483
Large hydro	22.7	266	309	341
Geothermal	43.2	86	186	333
Small hydro	9.5	19	49	106
Wind	4.7	44	266	542
Solar thermal	4.1	15	66	244
Photovoltaic	0.1	2	24	221
Solar thermal electricity	0.1	0.4	3	16
Marine (tidal/wave/ocean)	0.05	0.1	0.4	3
Total RES	1,365.5	1,745.5	2,964.4	4289
Renewable energy source contribution (%)	13.6	16.6	23.6	34.7

During periods of excess electricity generation, the additional electricity can be used by an electrolyser to split water into its constituent elements, thus storing it as chemical energy in hydrogen. Hydrogen fuel can be stored in underground caverns, tanks and pipelines in the form of pressurised gas or liquid. The transmission of energy in the form of pressurised hydrogen gas via pipelines allows for the delivery of high capacities at low transmission losses, compared with high-voltage transmission lines.[6] The stored energy can then be converted back into electrical energy via the use of a hydrogen fuel cell.[1]

1.2.1 The Hydrogen Fuel Cell

Proton Exchange Membrane (PEM) hydrogen fuel cells have been a significant focus of research due to their promise as a highly efficient way of converting stored chemical energy, in the form of hydrogen, into useful electrical energy without the production of fossil fuels. They are already in limited commercial use across a range of applications, most notably as replacements to conventional combustion engines in vehicles.[7] Schultz *et al*. calculated that if the entire surface traffic fleet were to use hydrogen in place of traditional fossil fuels, emissions of nitrogen oxide and carbon monoxide could be reduced by 50%, and thus would result in a significant improvement in global air quality.[4] However issues including cost and durability must be addressed for hydrogen fuel cells to enter mainstream use.[8]

Fig. 1-1 presents a simplified schematic of a hydrogen fuel cell, taken from Ref. [9].

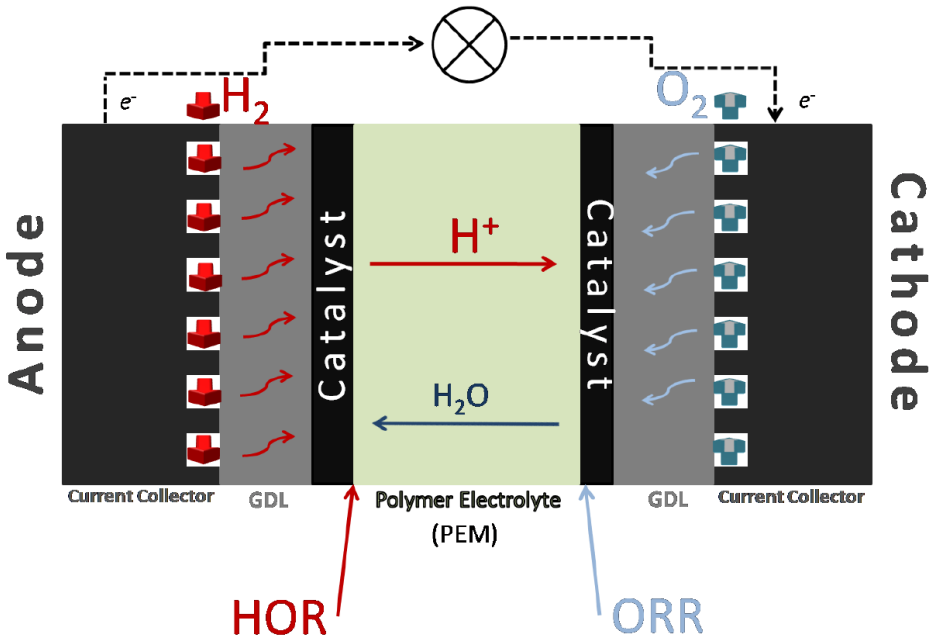

Figure 1-1 *schematic of a polymer electrolyte membrane fuel cell, taken from Ref. [9]. Hydrogen oxidation reaction (HOR) occurs at the anode, and oxygen reduction reaction (ORR) at the cathode*

Hydrogen fuel is fed into the cell and arrives at the catalyst layer of the anode, where the hydrogen oxidation reaction (HOR) occurs, splitting hydrogen into H^+ ions and electrons. The electrons flow through the circuit, producing a current, while the positive H^+ ions travel through the acidic polymer electrolyte membrane. Oxygen is introduced at the cathode, and via the oxygen reduction reaction (ORR), it reacts with the H^+ ions to produce water, which is the only waste product of the process.[10] The chemical reactions involved in the hydrogen fuel cell are summarised in Table 1-2.

Table 1-2 *Summary of chemical reactions that occur in a hydrogen fuel cell.*

	Chemical Reaction	Standard Potential (V_{RHE})
Anode	$H_{2(g)} \rightarrow 2H^+_{(aq)} + 2e^-$	0
Cathode	$½O_{2(g)} + 2H^+_{(aq)} \rightarrow H_2O_{(l)}$	1.23
Overall Cell	$H_{2(g)}) + ½O_{2(g)} \rightarrow H_2O_{(l)}$	1.23

At both the anode and the cathode, a catalyst is used to facilitate the electrochemical reactions by reducing their associated activation energy barriers. In a typical commercial catalyst, platinum (Pt) nanoparticles are dispersed over carbon-black[11] to increase the surface area of platinum available for catalysis, and to slow particle agglomeration.[12] A transmission electron micrograph of a commercial Pt/C catalyst is presented in Fig. 1-2 (Ref. [13]), showing platinum nanoparticles, with diameters on the order of a few nanometres, supported by an amorphous carbon-black material.

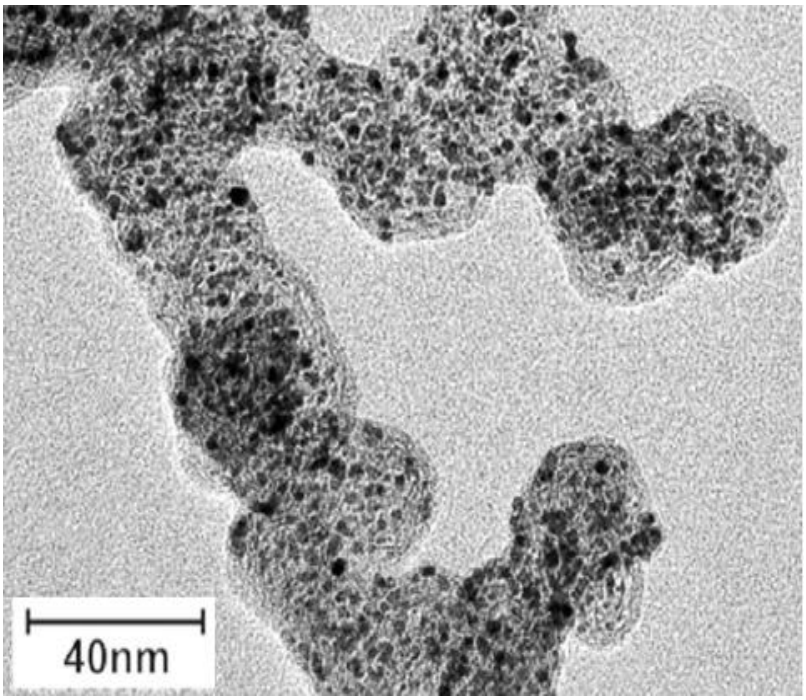

Figure 1-2 *A transmission electron micrograph of a commercial platinum on carbon catalyst. The lighter, larger spheres are the carbon black support material, with the platinum nanoparticles visible as the darker, smaller circles Taken from Ref. [13].*

Despite their widespread usage in commercial fuel cells, alternatives to Pt/C catalysts are still being extensively researched in order to address two long-standing issues: cost and durability. To reduce the cost, the amount of platinum required must be reduced, and to improve durability, the stability of both the platinum nanoparticles and the support material must be improved (see Chapter 2). The following Section 1.3 outlines the work presented in this thesis: the development of a novel graphene-supported platinum catalyst as an alternative to existing Pt/C catalysts.

1.3 Outline and Aims of the Thesis

The aim of the work presented in this thesis was the development of a catalyst for the oxygen reduction reaction, the rate-limiting reaction in a hydrogen fuel cell. To improve on the durability of existing fuel cell catalysts, graphene[14] was chosen as a support material for platinum nanoparticles for its high surface area[15], electrical conductivity[16] and chemical stability in acidic conditions[17] typical of a PEM fuel cell.

At the core of the methods in this work is the liquid exfoliation of a graphite intercalation compound in a polar aprotic solvent, tetrahydrofuran (THF), forming a graphenide solution containing negatively charged graphene sheets and positively charged metal ions.[18,19] This method reduces the number of energy-intensive steps typically required in the synthesis of graphene materials, thus ensuring the high-quality nature of the graphene produced.

The catalyst is produced via the on-sheet reduction of platinum salt by the negatively charged graphene present in the graphenide solution, in a one-pot, scalable synthesis. Rather than having to use an additional reduction agent, the use of the negatively charged graphene sheets to reduce the platinum salt results in highly stable nanoparticles.

The combination of high-quality graphene and highly stable nanoparticles meant that the graphenide derived catalyst exhibited excellent catalytic activity and best-in-class durability when rigorously stress tested with Department of Energy protocols at the half-cell level. These results were the foundation of a patent (EP3752458**)** and were published in the journal Nanoscale in 2020 (*"Realising the electrochemical stability of graphene: scalable synthesis of an ultra-durable platinum catalyst for the oxygen reduction reaction"*, Angel *et al.* 2020, https://doi.org/10.1039/D0NR03326J).

Chapter 2 begins with an outline of the chemical reactions that occur in a fuel cell, the role of platinum as a catalyst for the oxygen reduction reaction and reviews literature concerning the use graphene as a catalyst support material for platinum nanoparticles. The literature review first considers work where

the catalyst was tested at a half-cell level using rotating disk electrochemistry techniques, and then surveys papers where membrane electrode assemblies were produced and full fuel cell testing was conducted. The latter section of the literature review was then adapted for a section of a review paper written during the disruption caused by the Covid-19 outbreak and was published in Advanced Energy Materials in 2021 ("*Engineering Catalyst Layers for Next-Generation Polymer Electrolyte Fuel Cells: A Review of Design, Materials, and Methods"*, Suter *et al. 2021* ***https://doi.org/10.1002/aenm.202101025*).**

Chapter 3 provides a theoretical background for each experimental technique used throughout the thesis, as well as their practical experimental details and analysis techniques. This includes the synthesis, physical characterisation and electrochemical testing conducted at half and full cell levels.

The synthesis and characterisation of graphenide-derived platinum on graphene (GD-Pt/G) is described in Chapter 4. Raman spectroscopy is used to investigate the changes in graphitic materials at each step of the synthesis method. Transmission electron microscopy (TEM) is used to further investigate GD-Pt/G, measuring the nanoparticle size and distribution. X-ray photoelectron spectroscopy is employed to estimate the loading weight of platinum present in GD-Pt/G.

Chapter 5 reports the half-cell electrochemical testing of GD-Pt/G using rotating disk electrochemical techniques, followed by accelerated stress tests. Identical location TEM before and after cycling is presented as evidence for the stability of platinum nanoparticles.

Research that took place in the limited timeframe of the PhD following the return to the lab post-Covid-19 lockdowns, is presented in Chapter 6. The work describes the modification to the methods described in earlier chapters to scale up the production of GD-Pt/G for testing at the full cell level and presents the characterisation and testing of the scaled-up material.

The thesis concludes with Chapter 7, which summarises the findings of the research and discusses ongoing and future work.

Chapter 2: Electrocatalysts for Hydrogen Fuel Cells

*In this chapter, an overview of the components and the fundamental thermodynamics of the hydrogen fuel cell is presented. This is followed by an explanation of the mechanisms for the HOR and ORR and the role of platinum catalysts is justified, largely following descriptions given in references [*10,20*]. Problems with existing platinum catalysts are outlined, including a description of observed corrosion mechanisms, and graphene is suggested as a potential solution to these problems. A survey of existing graphene-supported platinum catalyst literature is presented. Finally, the objectives of this project are reiterated.*

2.1.1 Fuel Cell Components

The central focus of this work is development of a catalyst for a hydrogen fuel cell. As explained in Chapter 1, a catalyst comprising of platinum nanoparticles supported by carbon black is typically used at both the anode and the cathode of the fuel cell.

For the reactions to occur, there must be contact between the platinum nanoparticles and three components: electrons, protons, and the reactant gases. The boundary at which these three components meet is known as the triple-phase boundary (TPB).[21] To ensure as many of the platinum nanoparticles are in contact with a triple-phase boundary as possible, the Pt/C catalyst is mixed with a proton-conducting ionomer polymer in solution to form a catalyst ink. The resultant catalyst ink is deposited onto a microporous layer (MPL) and gas diffusion layer (GDL), which are often manufactured and sold together as a single component. The ink is deposited such that the loading of platinum is on the order of 0.2 mg_{pt} cm^{-2}.[10] The microporous layer contains hydrophobic PTFE mixed with carbon nanospheres and is designed to maximise gas transport and electrical conductivity while also allowing excess water generated to be expelled, reducing the occurrence of electrode flooding.[10] The GDL is typically a weave of porous carbon fibres that allow for facile gas transport while maintaining electrical conductivity. The

combination of the catalyst layer, MPL and GDL is referred to as a gas diffusion electrode (GDE).[21]

By sandwiching a solid electrolyte membrane between two GDEs, typically using a hot press, a membrane electrode assembly (MEA) is formed. The membrane is commonly made from perfluorosulfonic acid (PFSA) ionomers (most often Nafion, DuPont), which allows for the conduction of protons from one electrode to the other while inhibiting the flow of electrons and gases across the cell, reducing the chance of dangerous direct mixing of the reactant oxygen and hydrogen gases. Figure 2-1 below presents photographs of the spray coater and hot press used in this project.

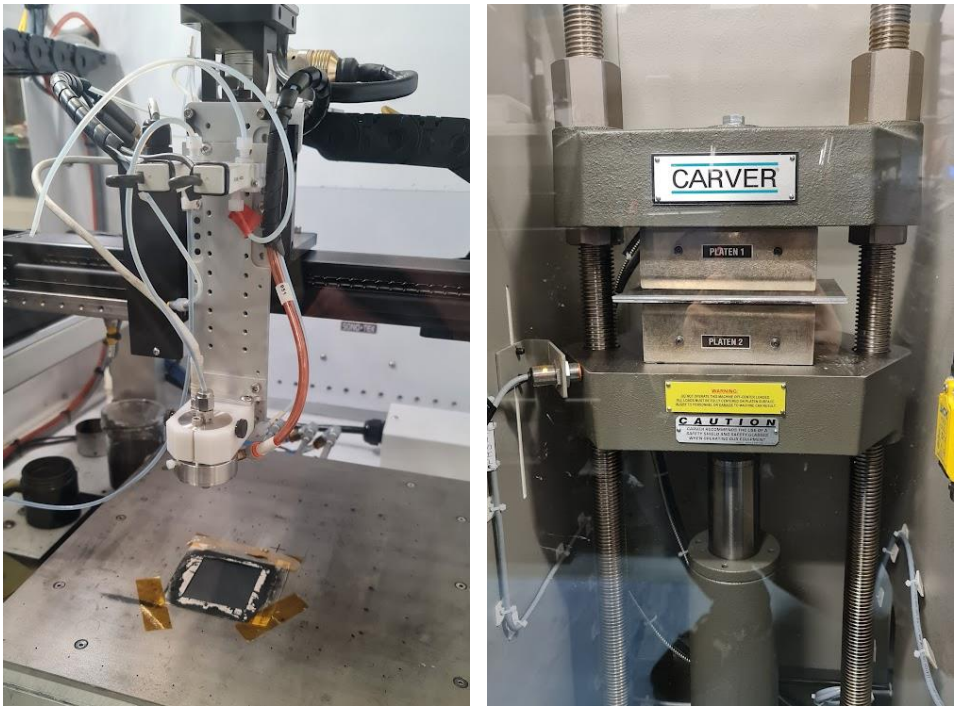

Figure 2-1 Left: *Ultrasonic spray coater used in this work, depositing catalyst ink on a gas diffusion electrode.* ***Right:*** *Hot press used in this work for the joining of the cathode and anode gas diffusion electrodes with a commercial nafion membrane*

The MEA is compressed between two bipolar plates, also known as flow field plates, which serve a range of functions within the fuel cell. Their primary role is to deliver gases to the GDEs: flow field channels within the plates allow for the transport of reactant gases through the cell to the catalyst layers and the removal of water away from them. They are made of either carbon composites or metal to allow for electrical connection between the catalyst layers and the rest of the fuel cell, acting as current collectors. The material

chosen must also be chemically stable and corrosion resistant such that they can withstand constant contact with water that is produced by the cell during operation.

The MEA and bipolar plates are held in place between two end plates, which contain inlets and outlets for the gases. In the experimental set up used in this work, a heating element is also inserted to control the temperature of the cell. A schematic of the components of the fuel cell and a photo of an assembled lab fuel cell[22] are shown in Figure 2-2.

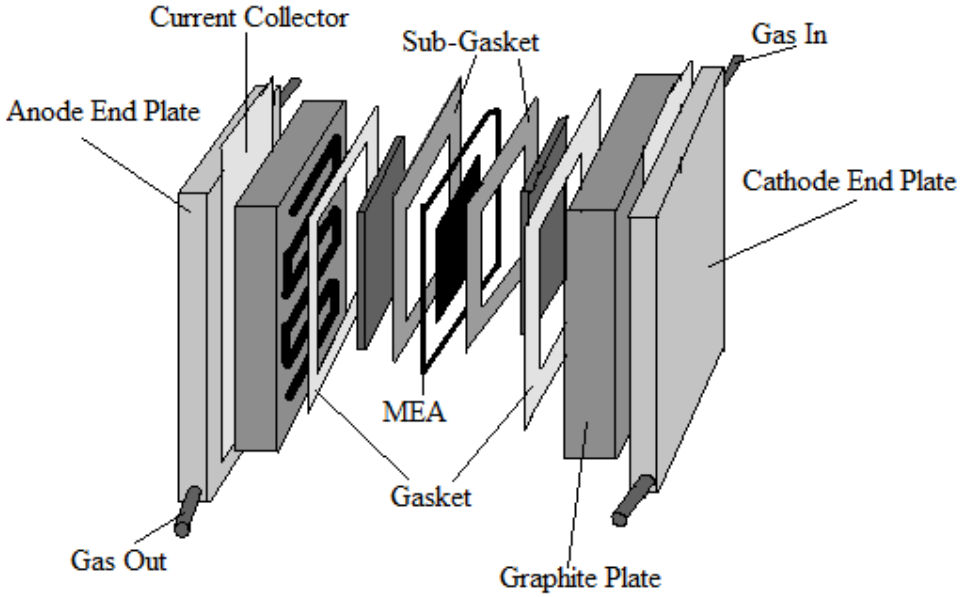

Figure 2-2 top: *schematic of fuel cell components, taken from ref [*174*]. **bottom**: photo of the fuel cell test system used in the work presented in this thesis*

2.1.2 Fuel Cell Thermodynamic Fundamentals

The overall reaction in a hydrogen fuel cell is the exothermic reaction of hydrogen and oxygen to produce water and heat, as described in Equation 1.1.[10]

$$H_2 + \frac{1}{2}O_2 \rightarrow H_2O + Heat \quad (2.1)$$

The difference between the enthalpies of formation of the products and reactants (h_f) gives the overall enthalpy of the chemical reaction, ΔH. At 25 °C the enthalpy of formation of water is -286 kJ mol^{-1}, and for elements it is zero by definition.

$$\Delta H = (h_f)_{H_2O} - \left(h_f\right)_{H_2} - \frac{1}{2}\left(h_f\right)_{O_2} = -286\ kJ\ mol^{-1} \quad (2.2)$$

The Gibbs free energy of the reaction (ΔG_f) is defined as the difference between the Gibbs free energy of products and Gibbs free energy of the reactants. The Gibbs free energy of the reaction varies with both temperature and pressure,

$$\Delta G_f = \Delta G_f^0 - RT\ ln\left[\frac{p_{H_2}p_{O_2}^{1/2}}{P_{H_2O}}\right] \quad (2.3)$$

Where ΔG_f^0 is the change in Gibbs free energy at standard pressure, R is the universal gas constant (8.314 J kg^{-1} K^{-1}), T is the temperature of the cell in Kelvin, and p_X are the partial pressures of the reactants and products (x = H_2, O_2, H_2O). If the fuel cell is reversible, where it is assumed that all Gibbs free energy is converted to electrical energy, the reversible fuel cell potential (E) is

$$E = -\frac{\Delta G_f}{nF} \quad (2.4)$$

Where F is the Faraday constant (96485 C) and n is the number of electrons, which for this reaction is 2. The temperature dependence of the reversible fuel cell potential is known as the Nernst potential[10], and is defined by the Nernst equation:

$$E = -\frac{\Delta G_f}{2F} = \frac{-1}{2F}\left\{\Delta G_f^0 - RT\ ln\left[\frac{p_{H_2}p_{O_2}^{1/2}}{P_{H_2O}}\right]\right\} \quad (2.5)$$

At 1 atm and 25 °C, ΔG_f^0 = -237200 J mol^{-1} and the reversible (Nernst) potential is

$$E = \frac{-\Delta G_f^0}{2F} = \frac{237200\ J\ mol^{-1}}{2 \times 96485\ As\ mol^{-1}} = 1.229\ V \quad (2.6)$$

By dividing the Gibbs free energy of the reaction by the enthalpy of the reaction, at standard temperature and pressure the theoretical efficiency of the fuel cell can be calculated to be 83%.

2.1.3 The Polarisation Curve

The theoretical open-circuit voltage (OCV) is defined as the difference between the Nernst potential of the cathode and the Nernst potential of the anode and can be shown to have the same value as the reversible cell potential (E = 1.229 V). [10]

During fuel cell operation, the cell voltage drops below the theoretical voltage due to irreversible losses. The drops in cell voltage can be represented by a polarisation curve, which plots change in cell voltage as a function of current load, as shown in the Figure 2-3.[23]

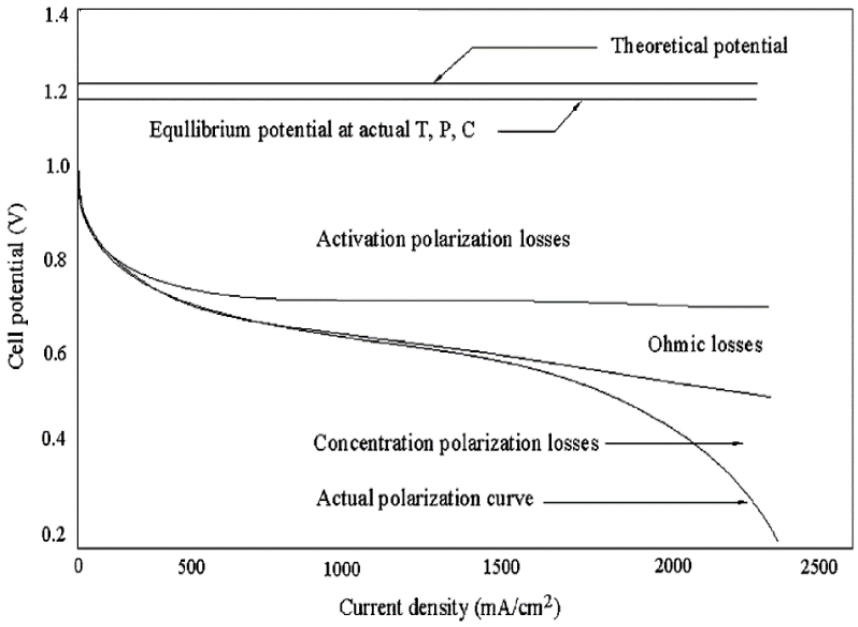

Figure 2-3 *Theoretical polarisation curve for a PEFC, adapted from ref. [23]*

Even when no current is drawn, the measured open-circuit voltage of an assembled fuel cell is lower than that of the theoretical potential of the cell. The irreversible losses are a result of mixed potentials, fuel crossover and internal resistance and shorting. On the cathode side, the mixed potentials are a combination of the oxygen reduction reaction (E_{ORR} = 1.229 V) and the formation of PtO ($E_{Pt/PtO}$ = 0.88 V), which results in a potential of about 1.06 V. Any hydrogen that permeates through the Nafion membrane can react with oxygen, also resulting in a mixed potential that reduces the OCV.[10]

As a current load is initially drawn from the fuel cell, activation polarisation losses are observed on the polarisation curve. These losses are a result of the energy required to overcome the activation energy of the oxygen reduction reaction and are in large part determined by the choice of catalyst and its electrochemical surface area, which is determined both by its nanostructure and by the macrostructure of the catalyst layer.[21]

Following activation losses, the losses observed in the region between 0.7 and 0.5 V are due to increases in resistance which are a result of the increase in current, and as such are known as Ohmic losses. The ohmic losses are dependent on the conductivity of the catalyst layer and the contact between the components within the fuel cell.[21]

In the region between 0.5 and 0.3 V, the decrease in potential is a result of the limit of the rate at which reactants can permeate the MEA and reach the catalyst nanoparticles, which is increased by the higher current load. As such, this region is known as the mass transport region. The faster the gases can diffuse through the electrode structure and react at the catalyst surface, the lower the mass-transport losses, and as such the losses are largely dictated by the structure of the electrode. [21]

The work in this thesis focuses on the development of a novel catalyst for ORR. For a polarisation curve to be obtained experimentally, a full fuel cell must be assembled, which requires a substantial amount of catalyst material for each test. As such, rotating disk electrochemistry (described in Chapter 3) is used to screen new materials, owing to the relative ease of testing and the requirement for less material, before full cell testing is performed. [21]

2.2 The HOR and ORR in Acidic Media

As hydrogen molecules reach the anode they come into contact with the surface of the catalyst layer, and at active catalyst surface sites (represented as *), the H-H bonds break and hydrogen atoms become adsorbed (H^*). This is shown in Equation 2.7.

$$^1/_2\, H_2 + {}^* \rightarrow H^* \quad (2.7)$$

This is the start of the HOR mechanism. The adsorbed hydrogen atom then gives up a single electron which is conducted away from the anode, flows through the circuit and arrives at the cathode. The resultant H^+ ion travels through the polymer electrolyte membrane to the cathode.

$$H^* \rightarrow H^+ + e^- + {}^* \quad (2.8)$$

Equation 2.8 completes the second half of the HOR mechanism. At the cathode, the hydrogen ion, electron and oxygen combine via the oxygen reduction reaction. This can occur via two different pathways, known as the dissociative "four-electron" pathway or the associative "two-electron" pathway. These processes are summarised in Fig. 2-4.[20]

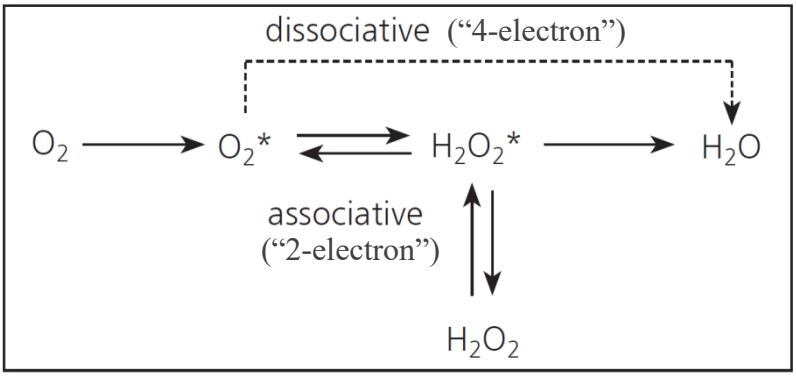

Figure 2-4 *Associative and dissociative mechanisms of the ORR in acid. Adapted from Ref. [20].*

The first step in both pathways occurs when the oxygen reaches the catalyst, where it adsorbs to a catalyst site. In the dissociative pathway, this results in the breaking of the O=O bond, as described in Equation 2.9.

$$^1/_2\, O_2 + {}^* \rightarrow O^* \quad (2.9)$$

The adsorbed *O** are reduced and pronated by the e^- and the H^+ that were produced by the HOR, producing *OH** (Equation 2.10).

$$O^* + H^+ + e^- \rightarrow OH^* \quad (2.10)$$

The adsorbed *OH** is further reduced and pronated, producing water which leaves the catalyst surface, as described by Equation 2.11.

$$OH^* + H^+ + e^- \rightarrow H_2O + {}^* \quad (2.11)$$

If instead, the reaction follows the associative pathway, the O=O bond does not break, and instead O_2 adsorbs to the catalyst surface. The adsorbed O_2* is pronated and reduced to give HO_2*, which then may result in the production of H_2O_2 after being further pronated and reduced (Equation 2.12).

$$HO_2{}^* + H^+ + e^- \rightarrow H_2O_2{}^* \quad (2.12)$$

The H_2O_2* can then desorb to form H_2O_2, which diffuses into the PEM and results in the degradation of the fuel cell.[7,10] Therefore, a good catalyst material must favourably catalyse the dissociative pathway rather than the associative pathway. This is known as selectivity, and is one of the key characteristics required of any catalyst material. The others are catalytic activity, stability and poisoning resistance.[20] From the above descriptions of the HOR and ORR mechanisms, it is clear that the ORR mechanism, having many more stages, is the more complex of the two. As a result, its kinetics are sluggish compared with those of the HOR. This means that much less catalyst loading is required at the anode, and catalysts for ORR are the primary focus of research.[24–29]

2.3 Platinum Catalysts for ORR

To achieve high catalytic activity, the catalyst material must allow the adsorption of species in such a way that the bonding between the catalyst and the adsorbed species is not too strong or too weak. If the bonding is too strong the adsorbed species won't leave the catalyst surface, blocking the catalytically active sites and limiting the rate at which the reaction can take place. If the bonding is too weak, the species may not adsorb effectively to

the catalyst. Therefore, to optimise catalytic activity, it is necessary to use a material that adsorbs the species strongly enough to break the chemical bonds as in Equations 2.7 and 2.9, but not so strongly that the resultant species can't be released once the reaction has occurred. This concept is known as the Sabatier principle, and is typically represented with a "volcano" plot showing various metals' activity toward the ORR as a function of oxygen bonding energy, as seen in Fig. 2-5, taken from Ref. [*20*].

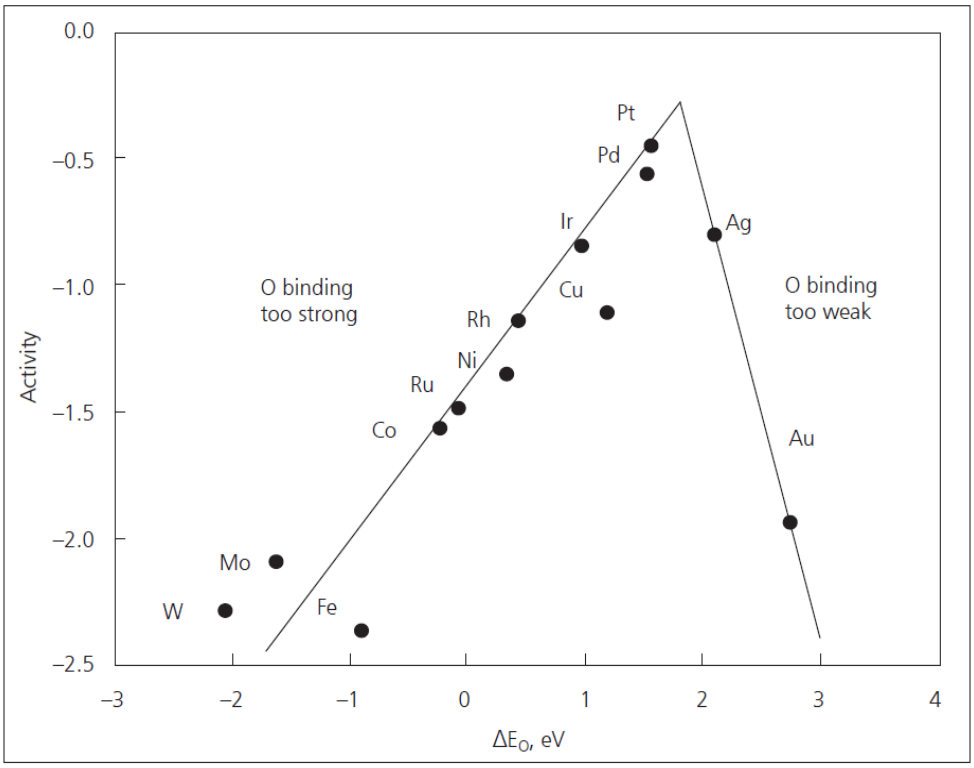

Figure 2-5 *ORR activity plotted as a function of oxygen binding energy, taken from Ref. [20].*

As can be seen in the diagram, the metal with the highest activity for the catalysis of the ORR is platinum, which can be seen closest to the peak of the volcano plot. Metals to the left of platinum on the graph bond with oxygen more strongly, and those to the right of platinum bond more weakly: in both cases this results in lower activity than platinum. Platinum also shows good selectivity for the dissociative ORR pathway, as O_2 typically has its O=O bond broken when adsorbed on platinum. This stops O_2 from adsorbing intact, which is the start of the associative pathway. Combining these properties with good stability for acidic conditions, it becomes clear that platinum is the most suitable pure metal for the catalysis of ORR. However, platinum is a rare

metal that is expensive and as such, much work has been done to minimise the amount of platinum required in fuel cells.

To maximise platinum activity, it is necessary to use it in nanoparticle form, in which its surface area-to-volume ratio can be optimised. The optimal size for platinum nanoparticles is *ca.* 2 nm, as smaller nanoparticles have higher strain and therefore weaker oxygen binding, moving their activity closer to the peak of the volcano plot.[30] However, below 2 nm, there is a higher proportion of low coordination number Pt atoms, which bond strongly with oxygen and result in lower catalytic activity.

This leads to a problem: to reduce surface energy, nanoparticles of all sizes tend to agglomerate into larger particles, reducing the catalytic activity of the platinum and impacting the lifetime of the fuel cell. To limit this process and to maximise the utilisation of the platinum, it is typically decorated onto a carbon-based support, such as in the case of commercial catalysts where carbon black is used.

The durability of these commercial carbon-supported catalysts remains a significant challenge. In the 0.6-1 V_{RHE} potential range, typical of regular fuel cell operating conditions, platinum nanoparticle degradation dominates, whereas in the 1-1.6 V_{RHE} potential range carbon corrosion becomes the dominant mechanism.[31] These mechanisms are shown in Fig. 2-3 (Ref. [32]).

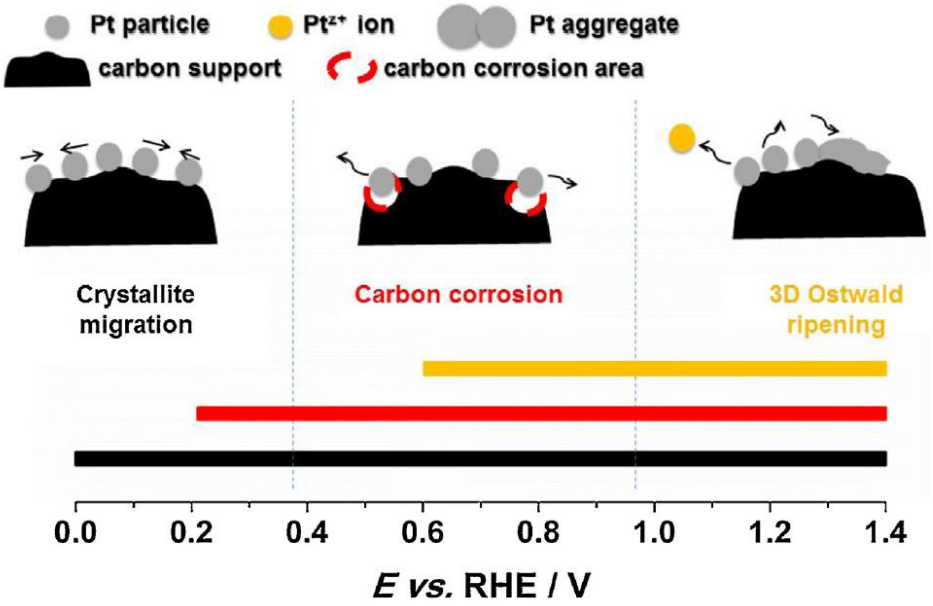

Figure 2-6 *Potential ranges of degradation mechanisms of Pt/carbon catalysts, taken from Ref. [32].*

Platinum nanoparticles are able to migrate and agglomerate across the full range of typical fuel cell potentials. The dissolution of Pt nanoparticles occurs via the dissolution of Pt oxides that form after the oxidation of the platinum surface. This occurs above 0.6 V_{RHE} and slows above 1.1 V_{RHE} due to the formation of a protective oxide film. The dissolved platinum can also be redeposited in a process known as Ostwald ripening, leading to further growth of the nanoparticles and a decrease in catalytic activity.[32] Carbon corrosion occurs via the reaction with oxygen to produce carbon dioxide. Carbon corrosion is thermodynamically possible for E>0.207 V_{RHE} but is kinetically slow, so dominates as the Pt dissolution slows above 1.1 V_{RHE}.

The US Department of Energy (DoE) has set out protocols and targets for accelerated stress tests (ASTs) of platinum catalyst layers in membrane electron assemblies (MEAs), tested as part of a working fuel cell, the targets of which are summarised in the tables below.[33]

Metric	Frequency	Target
Catalytic activity (mass activity)	Beginning and end of test	<40% loss of initial activity
Polarisation Curve	After 0, 1k, 5k, 10k, and 30k cycles	<30mV loss at 0.8 Acm^{-2}
Cyclic Voltammetry	After 10, 100, 1k, 3k, 10k, 20k, and 30k cycles	<40% loss in initial electrochemical surface area

Table 2-1 *Summary of targets set by the US DOE for MEA catalytic AST performance in the 0.6 – 0.95 V_{RHE} range, adapted from [*33*].*

Metric	Frequency	Target
Catalytic activity (mass activity)	Beginning and end of test	<40% loss of initial activity
Polarisation Curve	After 0, 10,100, 200, 500, 1k, 2k, and 5k cycles	<30mV loss at 1.5 Acm^{-2}
Cyclic Voltammetry	After 0, 10,100, 200, 500, 1k, 2k, and 5k cycles	<40% loss in initial electrochemical surface area

Table 2-2 *Summary of targets set by the US DOE for MEA catalytic AST performance in the 1 – 1.5 V_{RHE} range, adapted from [*33*].*

For testing the normal operating conditions of the fuel cell, the DoE protocol uses cyclic voltammograms, scanned between 0.6-0.95 V_{RHE} for 30,000 cycles, and to simulate the start-up and shut down of a fuel cell the test is modified to run between 1-1.5 V_{RHE} for 5000 cycles. The dominant corrosion mechanisms in the 0.6-0.95 V_{RHE} test impact the size and distribution of the platinum nanoparticles, whereas during the 1-1.5 V_{RHE} test the decrease in activity is associated with the corrosion of the carbon support material.

For rotating disk electrode experiments, it has been found that to reliably reproduce trends in durability seen in full fuel cell stack tests, it is necessary to cycle between 1-1.6 $V_{RHE.}$[34,35]

These targets, set in 2016, remain the same as those set in 2007, and as such it is clear that more research is required to produce more stable catalysts by replacing the supporting carbon with an alternative material. One of the most promising new support materials is graphene and the reasons for this are explored in the following section.

2.4 Graphene as a Catalyst Support Material

2.4.1 Graphene: Synthesis and Properties

Since its isolation[14] in 2004, graphene has become a major research focus due to its unique electronic and mechanical properties, with a wide range of potential applications. It is composed of a two-dimensional array of carbon atoms and as such can be thought of as the building block for other carbon structures. Fig. 2-7 (Ref. [36]) shows a layer of graphene, graphite, consisting of many layers of graphene, a graphene sheet rolled into a cylinder is a carbon nanotube, and a fullerene composed of wrapped graphene.[37]

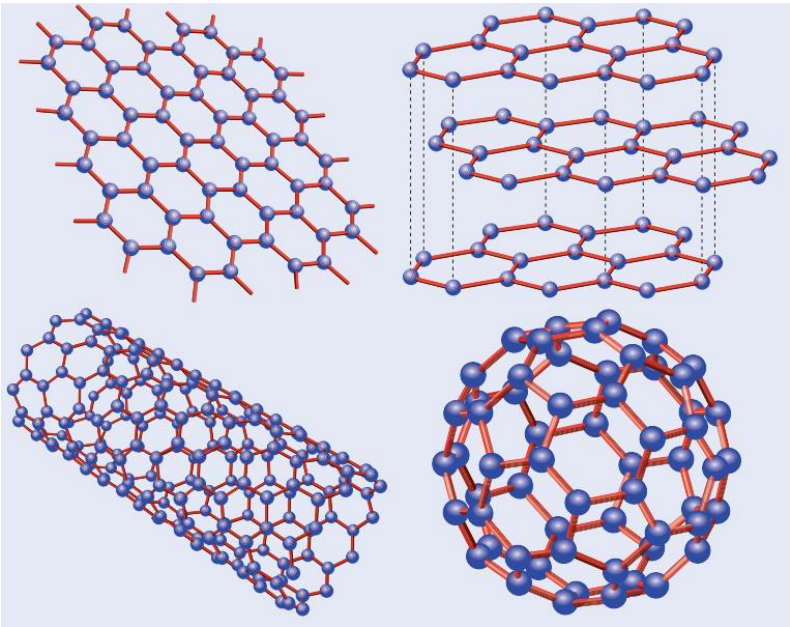

Figure 2-7 *(top left) shows a layer of graphene, (top right) graphite, consisting of many layers of graphene, (bottom left) a graphene sheet rolled into a cylinder is a carbon nanotube, and (bottom right) fullerene composed of wrapped graphene. Taken from Ref. [36].*

Within the graphene layer, each carbon atom has four bonding electrons, of which three are used in covalent bonds with neighbouring carbon atoms. This leaves one electron per carbon atom free, producing a field of delocalised electrons, allowing graphene to conduct electricity. Furthermore, because graphene is zero-gap conductor where its charge carriers behave as if they were massless,[38,39] graphene charge carrier mobility has been measured to be as high as 200,000 $cm^2\ V^{-1}\ s^{-1}$ in defect-free graphene.[39] Combining its excellent conductivity with a large theoretical surface area[24] of 2630 $m^{-2}\ g^{-1}$,

high breaking strength and chemical resistance[17], graphene shows promise as a catalyst support material that could both lower the catalyst-metal loading required and extend the lifetime of the catalyst layer.[25]

2.4.2 Half-Cell testing of Metal-Graphene Catalysts

One of the various challenges in the commercialisation of graphene is the ability to synthesise large amounts via a scalable method that produces a consistent graphene material. As a result, the majority of existing literature uses rotating disk electrochemistry to benchmark the catalytic activity of their materials, as this technique requires much less mass of material when compared to complete full cell membrane electrode assembly testing. This section reviews a number of studies in which the novel materials were assessed using RDE techniques, with the following section (2.4.3) reviewing studies that were successful in scaling their work to the MEA level.

Much of the initial work with graphene, including its discovery, was via what has become famously known as the "scotch tape" method, in which graphene is obtained by mechanically exfoliating graphite using adhesive tape.[14] While this method is useful in obtaining pristine graphene samples that are fit for purpose for experiments measuring intrinsic properties of graphene, it is time-consuming and labour-intensive, meaning that other methods are required to produce graphene for applications. These methods can roughly be split into two categories: "bottom-up" synthesis where graphene is grown on a substrate, and "top down" where a carbon material precursor, such as graphite oxide, is exfoliated via various methods to obtain graphene.[40,41]

Of the bottom-up methods, common examples include epitaxial growth and chemical vapour deposition. These methods typically require harsh reaction conditions, such as high vacuum environments and temperatures, but also produce high-quality graphene with few defects. Though some work has been done in the scale-up of these methods[42], the resultant graphene is typically limited in size by the substrate used, and as such these methods are more often used in the production of small electronic devices rather than electrochemical applications.[40,41]

Nonetheless, in 2018 Abdelhafiz *et al.*[26] published work showing a particularly interesting example of a novel platinum/graphene catalyst for ORR. In this work, rather than disperse platinum across a carbon support material, platinum was grown controllably, by layer, on a gold substrate, and then a graphene layer was grown epitaxially on top. The epitaxial nature of the produced platinum/graphene composite produced an electronically coupled catalyst in which the graphene appears "chemically transparent". The authors suggested that reactants approaching from the graphene end, rather than the platinum end, still undergo catalysis as if they were in contact with the platinum layer itself. Furthermore, the strain placed on the platinum crystal structure by the graphene enhances its activity toward ORR, and the graphene acts as a protective cap that inhibits the corrosion of the platinum, with the material showing no change in activity or structure after a 1000 cycle accelerated stress test. The authors go as far as to claim "infinite" corrosion resistance to activity loss due to the corrosion mechanisms listed in Section 2.3; however, it should be noted that 1000 cycles is but a small fraction of the requirements listed by the US DoE, and as such much longer ASTs are required to support this claim. Despite its promising activity and corrosion resistance, the fact that this method requires platinum and graphene to be grown under harsh conditions on a gold substrate also limit its application in commercial-scale use both in terms of ease of scale-up and in cost of raw materials.

2.4.2.1 Reduced Graphite Oxide

Of the various top-down approaches, the most common is the chemical reduction and exfoliation of graphite oxide (GO) to reduced graphene oxide (rGO). This allows for significant amounts of material to be produced, making it suitable for electrochemical applications.[43] First, a variation of a modified Hummer's method[44] is used in which graphite is directly oxidised by a strong oxidising agent such as potassium permanganate. After various steps of cleaning and drying, the graphite oxide can then be exfoliated and reduced to give rGO in steps typically involving high-energy ultrasonication and heating.[41,45] Finally, the active catalyst metal, often platinum, is added by reducing a metal precursor with a separate reducing agent, usually requiring

further heating, cleaning and drying. The finished metal-rGO catalyst powder is then re-dispersed as an ink via a further step of ultrasonication, and can then be deposited for electrochemical testing.[46–55]

Reduced graphene oxide-supported catalysts form the large majority of ongoing research. One difficulty in the use of rGO is that the layers of graphene tend to restack, hindering oxygen diffusion throughout the catalyst and slowing ORR activity.[28] One solution was presented in work by Li *et al.* in 2012. A platinum-rGO catalyst was synthesised following a procedure similar to that described above, and then was composited with a high-surface-area carbon black (CB) material.[28] This was achieved simply via the stirring of the Pt/rGO composite with carbon black in IPA overnight. Using transmission electron microscopy, shown in Fig. 2-8 (a) and (b), they found that platinum nanocrystals had been loaded uniformly on rGO with negligible aggregation.[28]

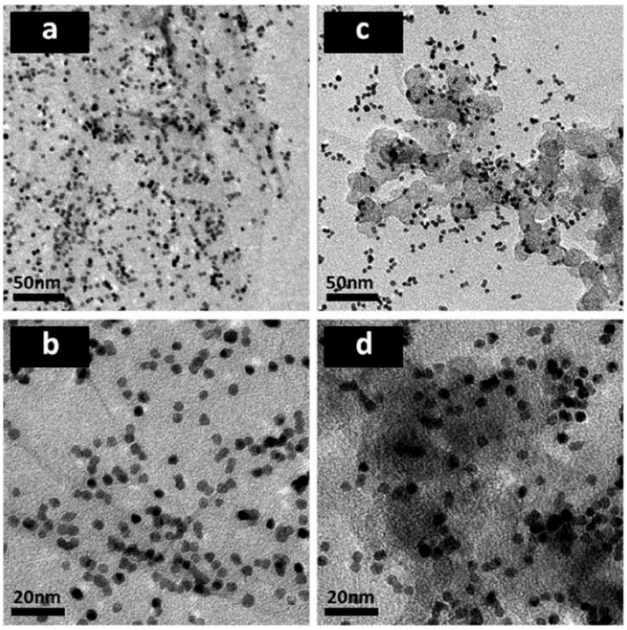

Figure 2-8 *(a), (b) Transmission electron micrographs of Pt/rGO at various length scales. (c), (d) Micrographs of Pt/rGO/CB composites. Taken from Ref. [*28*].*

Furthermore, it can be seen in Fig. 2-5 (c) and (d) that the Pt/rGO/CB composites showed a thorough mixing of the materials, and that the platinum remained on the rGO without becoming detached onto the carbon black. It was found that although none of the Pt/rGO samples performed as well as a

commercial Pt/C catalyst, the samples with carbon black mixed in performed better than those without.

The authors justified this by suggesting that carbon black particles enlarge the gaps between restacked rGO sheets, thus improving oxygen diffusion throughout the catalyst. It was observed that the more carbon black added to the sample, the better it performed. After accelerated stress tests of 20,000 cycles, it was found that while the commercial Pt/C catalyst lost ca. 51% of its initial activity, the Pt/rGO/CB sample retained more than 80% of its activity, confirming the importance of rGO in the durability of the Pt/rGO/CB catalyst.

Chen et al. further develop the principle of increasing the spacing between restacking rGO layers by using silicon carbide nanoparticles intercalated into the structure.[56] This was achieved by stirring silicon carbide nanoparticles and Pt/rGO aqueous suspension overnight, and found to produce a "novel 3D sandwiched architecture" in which the SiC nanoparticles effectively inhibit the restacking of the rGO sheets. The composite Pt/rGO/SiC material was found to exhibit enhanced activity compared with a commercial catalyst in both rotating disk electrode and fuel cell tests. They claim this was due to the sandwiched structure leading to greatly enhanced mass transport when compared with Pt/rGO and commercial Pt/C. The durability of the samples was investigated using a 10,000 cycle accelerated stress test, and although the Pt/rGO/SiC sample performed better than the commercial Pt/C sample tested, a 60% loss in electrochemical surface area was measured, meaning it falls short of the targets set by the US DoE and outlined in Section 2.2.

Research is also being conducted beyond the study of platinum nanoparticles supported by rGO, such as studies considering platinum nanowires and alloys. One such study was conducted by Wang *et al.*[57], who modified graphite oxide with sulphur, which then served as nucleation sites for the growth of platinum nanowires (termed "SG-PtNW"), SEM of which is presented in Figure 2-9. It was found that longer platinum nanowires were grown when an increased amount of platinum was used during the synthesis process. The SG-PtNW sample was found to exhibit better activity toward ORR than a commercial Pt/C sample, as platinum nanowires have a larger number of exposed

platinum atoms compared with spherical Pt nanoparticles typical of the Pt/C commercial sample. However, the work presented does not include any corrosion data, and as such it is difficult to evaluate how the increased number of exposed platinum atoms affects the rate at which the platinum dissolves and agglomerates, which is essential in understanding how the catalyst may degrade with cycling.

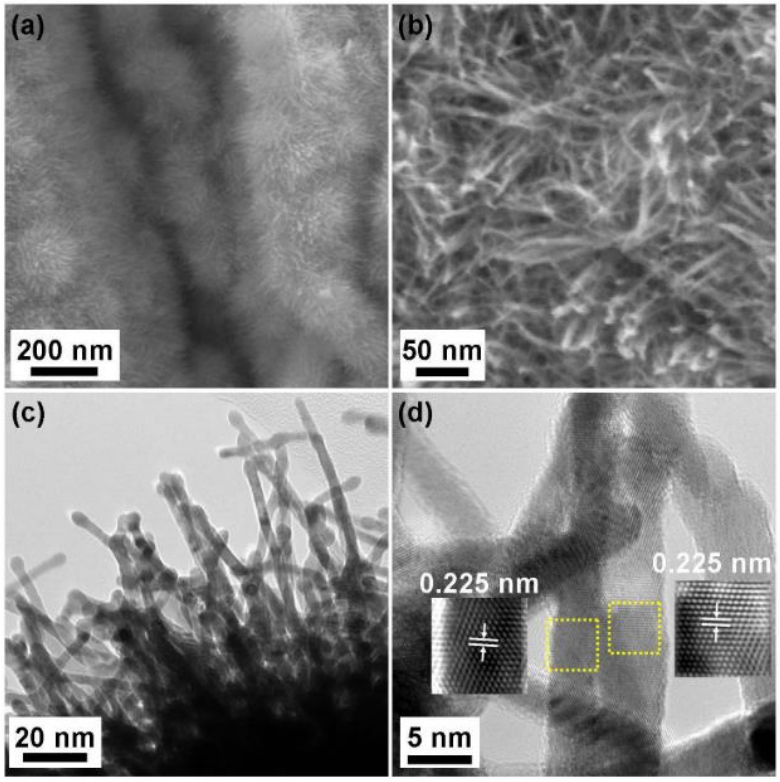

Figure 2-9 *(a,b) SEM and (c,d) TEM of SG-PtNW catalyst produced by Wang et al.*[57] *The images show a high density of platinum nanowires on the surface of sulfur doped graphene. The nanowires are shown in (d) to be single crystals, grown along the <111> direction, with the distance between the planes found to be 0.225 nm.*

By modifying the conditions and metal precursors added during the synthesis of the catalyst, it is possible to produce alloys of platinum with other metals supported by rGO, following a similar process as outlined previously. In one such example, rather than just adding a platinum precursor to a GO dispersion, Sun *et al.* added both a platinum and palladium precursor. These precursors were reduced simultaneously, resulting in the production of dendritic platinum/palladium nanoparticles on rGO.[50] The dendritic structure of the platinum/palladium nanoparticles provides a larger number of catalytic sites than spherical platinum nanoparticles as are typical of a commercial Pt/C catalyst, resulting in improved catalytic activity toward the ORR.

Furthermore, in chronoamperometric tests in which the catalysts were held at 0.1 V for 10,000 s showed that the Pt/Pd catalyst exhibited better durability than the commercial Pt/C.

Although rGO shows promise as a catalyst support material, the methods used to produce rGO-supported catalysts share many energy-intensive steps in common, often including repeated sonication, ultra-centrifugation and high temperatures, which are difficult to scale up. Furthermore, this leads to a high number of defects in the rGO structure, which negatively impacts the catalyst durability[58], particularly at higher voltages associated with fuel cell start-up and shut-down (1-1.6 V_{RHE}). As a result, RDE accelerated stress tests are typically only carried out across the 0.6-1 V_{RHE} range, and rarely for more than a few thousand cycles, to mitigate the damage that occurs over long cycles and higher loads. A summary of various graphene-supported catalysts with their associated corrosion tests and results are summarised in Table A1 presented alongside data from this work.

2.4.3 Full cell testing of metal-graphene composite catalysts

Testing graphene support materials in an MEA requires a larger amount of material to be synthesised compared to RDE (10s of milligrams vs fraction of a milligram respectively), and as such the literature is dominated by work investigating the use of graphite oxide. While graphite oxide and its derivatives have higher resistivity than high-quality graphenes produced via methods such as CVD, its relatively low cost, facile synthesis and solubility in water make it readily available for scale up.[59] Oxygen functionalisation defects on the GO surface mean that nanoparticles can be grafted onto the support without the need for acid treatment[60], although some studies have found acid treatment is an effective way to introduce further functionalisation that improves catalysis.[61] This has been reported to lead to stronger "anchoring" interactions between the surface functional groups and the platinum nanoparticles, resulting in improved platinum catalyst stability. However, the presence of oxygen functional groups and surface defects are widely reported to negatively impact the stability of the carbon support material upon cycling.[21]

In one such study conducted by Ghosh *et al*., functionalised rGO was compared with Pt/C in half and single cell tests.[62] Graphite oxide was prepared using modified Hummer's method and exfoliated via thermal shock at 1050 °C followed by sonication in DMF solution, before being washed and dried to obtain reduced graphene oxide nanosheets. The platelets were then further functionalised by sonication in an aqueous solution of citric acid, which was then filtered, washed and heat-treated at 300 °C. Platinum nanoparticles were then added via reduction of a platinum precursor using $NaBH_4$, producing catalysts with a Pt loading of 20 wt.%. FTIR was used to show that the acid treatment process introduced carboxyl, hydroxyl and carbonyl groups, which are responsible for anchoring metal ions during synthesis, and increase the hydrophilicity of the material, allowing for better dispersion for catalyst ink preparation. In fuel cell tests, the graphene and functionalised graphene supports were compared against a Pt/C catalyst and were found to have maximum power densities of 426, 455 and 314 mW cm^{-2} respectively. The improved maximum power densities are reflected in the larger ECSAs, measured using cyclic voltammetry, which suggest that the functionalisation reduces the restacking of the graphene sheet and ensures that the platinum nanoparticles remained well-anchored during initial fuel cell conditioning. However, the ECSA and MEA performance of the commercial Pt/C sample presented are much lower than is typically expected, making it difficult to compare these results with existing literature.

2.4.3.1 Reduced Graphene Oxide and Spacers

Graphenes of all kinds have a strong tendency to restack due to van der Waals forced between individualised sheets, and agglomerate in aqueous solutions.[63] The restacking of the graphene is a more significant problem in full-cell testing, where the 3D morphology of the MEA plays an important role, when compared to RDE testing in which the catalyst layer is deposited as a thin film. Restacking leads to the formation of low-porosity catalyst layers, limiting the accessibility of the platinum nanoparticles and reducing the number of triple-phase boundaries formed.[21] Therefore, in the majority of rGO catalyst supports, a spacer is again required to optimise performance. The spacer is often a different, less stable carbon phase, the amount of which

needs to be carefully balanced to optimise for both durability and performance. [64]

The most commonly used additive is carbon black. Work by Park *et al.* used readily available commercial carbon black as a spacer between rGO, examining the impact of varying the amount of carbon black added.[65] Platinum-decorated reduced graphene oxide (Pt/rGO) was synthesised by oxidising natural graphite flake, which was then reduced using heat treatment under inert gas to produce wrinkled graphene sheets, and then an ethylene glycol reduction method was used to deposit Pt nanoparticles. Catalyst inks were then prepared by ultrasonication of Pt/rGO with Nafion solution, DI water, methanol and varying amounts of carbon black. In fuel cell tests conducted with an 8 cm^2 MEA, it was found that the double layer capacitance increased as the carbon black content increased from 0% to 50%, indicating an increase in the interface between catalyst and ionomer. On the other hand, the measured ECSA increase significantly from 32 m^2 g^{-1} to 50 m^2 g^{-1} as carbon black content increased to ca. 25 wt. % carbon black, and then decreases as carbon black increases further. The authors suggest that excess carbon black in the catalyst layer can block platinum nanoparticles and limit catalytic performance. Using AC impedance spectroscopy, the charge transfer resistances of Pt/rGO was found to be 3.1 times higher than that of CB + Pt/rGO, indicating that carbon black increases the number of three-phase boundaries. The authors suggest this was the result of exposing more of the platinum nanoparticles, thus increasing interfacial oxygen kinetics. However, it should be noted that again in this study, the reported Pt/C activity was below what is expected of a commercial Pt/C MEA.

To improve the cycling stability of a commercial Pt/C, Jung *et al.* synthesised a hybrid material containing varying amounts of Pt/GO and Pt/CB.[64] Using cyclic voltammetry in a half-cell system, the authors measured the ECSA of the hybrid catalysts before and after 60 minutes of CV cycling between 0.4 and 1.2 V at 50 mV s^{-1}. Although the ECSA of the catalyst decreased with an increasing amount of Pt/GO added to the Pt/C catalyst, the durability increased consistently, with the highest durability measured for the 100% Pt/GO sample. Importantly, it was found that adding a relatively low amount of Pt/GO (20% by mass) significantly improved the durability of the catalyst,

with further amounts of Pt/GO added resulting in diminishing returns in increases in durability, at the cost of a large drop in initial ECSA.

To investigate the stability of the hybrid material further, an accelerated deactivation test was carried out in a full cell system by applying a voltage of 1.4 V for 3 hours. The Pt/C catalyst saw a 45.4% loss in current density at 0.6 V, compared with only a 17.7 % decrease exhibited by the hybrid catalyst containing 20% Pt/GO. The majority of the activity loss measured in polarisation curves of the Pt/C material was observed at high current densities, which the authors suggest was caused by the agglomeration or loss of platinum nanoparticles. The authors therefore suggest that the increased durability of the hybrid catalyst is a result of GO impeding the loss of Pt nanoparticle surface area. This is supported by TEM of the catalyst layers obtained before and after the accelerated degradation test, which found very little agglomeration of the nanoparticles in the hybrid catalyst, compared with the Pt/C catalyst. Although not discussed by the authors, it is likely that the choice of 1.4 V for the stability test would also have caused corrosion of carbon in both the commercial and novel materials. Therefore, some of the difference in the relative change in performance between the two materials may have also been a result of the difference in carbon-corrosion stability of the rGO compared to the carbon black. Without further detailed analysis of the catalyst layer before and after testing, or measurements of CO_2 from the exhaust of the system, it is impossible to deconvolute the influence of these factors on the stability of the novel composite.

Rather than introducing an additive such as carbon black after the synthesis of a Pt/rGO catalyst, Şanlı *et al.* showed that introducing carbon black before platinum deposition is also an effective method of producing hybrid catalysts.[66] The synthesis method is summarised in the schematic presented in Figure 2-10. The work explains that initially mixing carbon black to GO prevents graphene restacking during the Pt impregnation steps of the synthesis, and results in better platinum utilisation and lower mass transfer resistance compared with both Pt/CB and Pt/rGO samples tested. It was again found that a weight ratio of 75:25 produced the highest measured activity in fuel cell tests, where an MEA loaded with 0.5 mg Pt cm^{-2} obtained a

maximum power density of 654 mW cm^{-2} and a Pt utilisation efficiency of 2.58 kW g_{Pt}^{-1}.

Building on this work, the group published a development of this method with further improved performance. Kaplan *et al*. again mixed carbon black and graphite oxide mechanically before using microwave-assisted reduction method to reduce H_2PtCl_6 to produce Pt/rGO/CB.[67] The resulting best-performing hybrid catalyst (75:25 rGO:CB) achieved a maximum power density of 1091 mW cm^{-2}. Using EIS, both the charge transfer resistance and total resistance were found to be lowest for this catalyst when compared with both Pt/C and Pt/rGO.

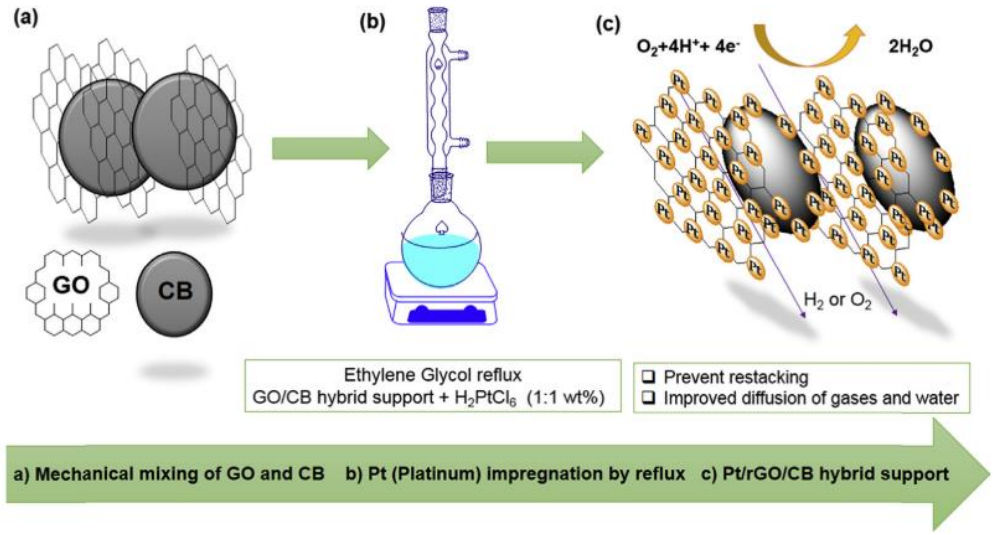

Figure 2-10 *Schematic detailing the syntheis process used by Şanlı et al. to produce a composite of carbon black and graphene decorated with platinum nanoparticles, where the carbon black has been introduced before the deposition of nanoparticles to impede the restacking of the graphene.* [66]

2.4.3.2 Graphene nanoplatelets as a catalyst support

Despite its successes, reduced graphene oxide is as such still fundamentally limited by the defects produced during its synthesis[68] and has yet to truly demonstrate improved durability under the high voltage loads experienced during the start-up and shut-down of a fuel cell. As such, other, less defective graphenes are also being explored as carbon support materials for catalyst nanoparticles.

Graphene nanoplatelets (GNPs), typically produced via the exfoliation of intercalated graphite, retain a much more graphitic structure compared with rGO, resulting in improved mechanical and electronic properties compared

with GO.[69] Furthermore, its highly graphitic nature means that there are fewer defects to initiate carbon corrosion from, and increased π bonding strength with Pt nanoparticles. [68,70–76] The combination of these effects in theory should result in the desired improved corrosion resistance required.

This was first demonstrated by Shao *et al.* in 2010 at half cell level, who compared the activity and durability of Pt/GNPs against that of Pt/CNT and commercial Pt/C catalysts.[68] GNPs were prepared via microwave-aided intercalation of sulfuric acid, followed by exfoliation using ultrasonication and milling, and then functionalised with poly(diallyldimethylammonium chloride) (PDDA) in order to stabilise platinum nanoparticles. Platinum nanoparticles were then added to both the GNP and MWCNT catalyst supports via a standard ethylene glycol reduction method, achieving a loading of 20 wt.%. In RDE experiments, the Pt/GNP sample exhibited both the largest kinetic current at 0.9 V, and the highest retained ECSA and kinetic current, after an accelerated durability test consisting of 44 hours of potential steps between 1.4 V and 0.85 V. While the Pt/CNT and Pt/C experienced a relative decrease of 75% in both ECSA and kinetic current, Pt/GNP showed a 40% and 20% decrease in ECSA and kinetic current respectively. Physical characterisation verified the high level of graphitisation and low number of defects present in the GNPs compared with both Pt/CNT and Pt/C samples, which the authors suggest is the reason for its enhanced durability under carbon corrosion conditions.

Although these results were promising, it wasn't until 2016 that GNPs were examined in full single-cell tests. Şanli *et al.* compared a number of graphene supports, including rGO and commercially-obtained GNPs, in combination with a number of platinum nanoparticle impregnation methods, such as sodium borohydride reduction and ethylene glycol reflux.[77] TEM imaging showed that ethylene glycol and ascorbic acid reduction methods produced suitable Pt nanoparticle distributions (average size 2-3 nm), whereas the sodium borohydride reduction method resulted in Pt islands that were on average 15 nm in diameter, which were much too large for efficient catalysis. Although Pt/GNP showed similar ECSA values to a commercial Pt/C sample in half-cell tests, in single-cell polarisation curve tests the GNP sample

displayed large mass transport losses at higher current densities due to restacking preventing efficient oxygen diffusion throughout the MEA.

To prevent this, the group explored the use of carbon black as a spacer material. In the first of two papers published in 2019, Arici *et al*. compared an in-house Pt/C sample with Pt/GNP and Pt supported by a 50:50 mix of GNP:C.[78] Platinum nanoparticle deposition was achieved by the direct impregnation of a $Pt(dba)_3$ complex, which was then reduced at room temperature under a hydrogen atmosphere. In RDE tests, the hybrid of GNP/C exhibited the largest kinetic current and mass activity, showing a significant improvement over GNPs on their own (120 versus 47 mA mg^{-1}_{Pt}). The improvement in activity translated directly into single-cell polarisation curve tests, where Pt/GNP-C obtained a maximum power density of 377 mW cm^{-2}, compared with 178 and 247 mW cm^{-2} for Pt/GNP and Pt/C respectively, suggesting that the addition of carbon black effectively inhibits the restacking of the GNPs.

The use of carbon black as a spacer for GNPs was further optimised in another paper published later in 2019 by the same group. *Daş et al.* performed a similar study to Arici *et al.*, although this time using a super-critical CO_2 reduction method to produce optimally sized nanoparticles and investigating a number of GNP:CB ratios ranging from 100:0 to 0:100.[69] In half-cell corrosion tests, samples were subjected to a potential hold at 1.2 V for 24 hours, with CVs and LSVs recorded before and after. Of all the samples that contained C, the 60:40 GNP:C showed the highest durability, with a 20.22 % decrease in ECSA, compared with a 50.78 % decrease measured for the Pt/C catalyst. Polarisation curve tests showed that the 60:40 GNP:C ratio was the best performing of all the hybrid GNP:C materials and outperformed both Pt/GNP and a commercial Etek Pt/C catalyst, as shown in the polarisation curves presented in the Figure 2-12. The H60 sample (60:40 GNP:C) exhibits the greatest maximum power density (0.48 W cm^{-2}), and greatest current density obtained at 0.2 V (ca. 2000 mA cm^{-2}). The increased performance of the 60:40 GNP:C sample is attributed to the relatively high surface area and small pore volume, which resulted in higher accessibility and therefore utilisation of active platinum nanoparticles.

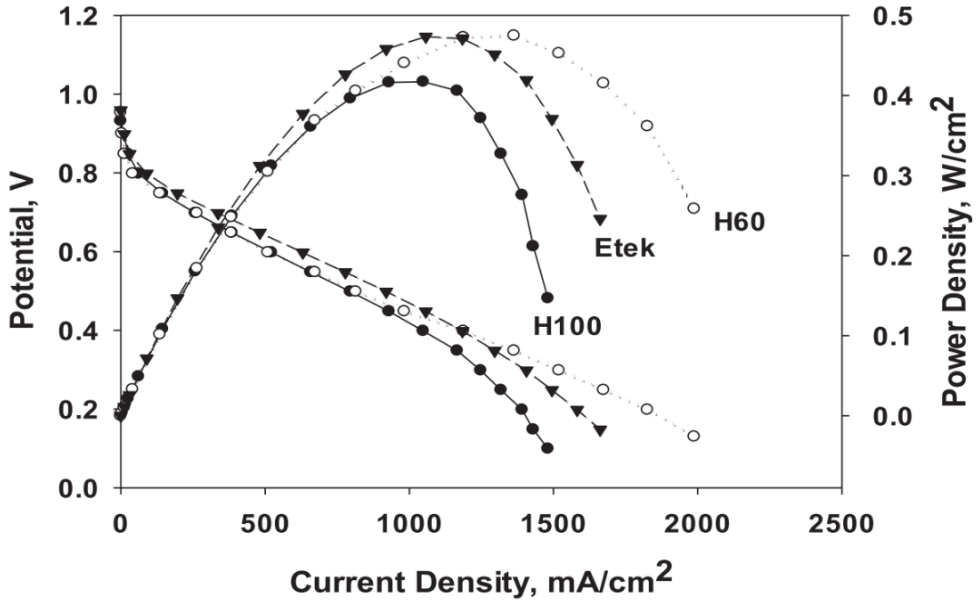

Figure 2-11 *Polarisation curves and associated power curves of Pt/GNP (H100), Pt/GNP:C (H60, 60:40 ratio of GNP/C) and commercial Etek Pt/C (Etek). Taken from ref [69].*

2.4.3.3 Three-dimensional graphene composites

To circumvent the problem of graphene restacking altogether, research has been conducted into novel three-dimensional, graphene structures[79–81] which exhibit their own unique properties, including high specific surface areas[82,83] and porosities.[84] In 2013, Liu *et al*. developed a graphene foam through a simple synthesis method via the combustion of sodium ethoxide, which produced a black powder that was washed, dried and subsequently heat-treated to reduce oxygen content.[83] After the addition of Pt nanoparticles, the material was tested in both half and single cell experiments. Although half-cell tests were promising with an ECSA 50% greater than a commercial Pt/C catalyst (101 $m^2\ g^{-1}$), and a mass activity 30% higher (176.1 A g_{pt}^{-1}), fuel cell tests showed a need for optimisation, with significant mass transport losses observed in the high current density region.

More recently, Karuppanan *et al*. have achieved more promising results with an N-doped graphene foam, obtaining a maximum power density of 394 mW cm^{-2} in single cell tests, compared with 201 mW cm^{-2} obtained for a commercial Pt/C catalyst.[84] A polyurethane sponge template was immersed in an aqueous solution of reduced graphene oxide, urea, hydrazine hydrate and ammonia, before being heat-treated to produce a free-standing graphene foam. After a hydrothermal polyol reduction method was used to decorate the foam with platinum nanoparticles, the foam was sonicated with DI water, IPA and 5 wt% Nafion solution, spray-coated onto Toray carbon paper to form a cathode catalyst layer. SEM of the material is presented in Figure 2-13. The improved activity compared with Pt/C observed in single-cell polarisation curve tests was attributed to the nitrogen doping and 3D foam structure. The 2D graphene sheets present in the foam network gave rise to high electronic conductivity, while nitrogen-doping stabilises the platinum nanoparticles and enhances the electrocatalytic activity. The porous foam structure provides a

high specific surface area and allows for efficient mass transport and adequate ionic contact with the electrolyte.

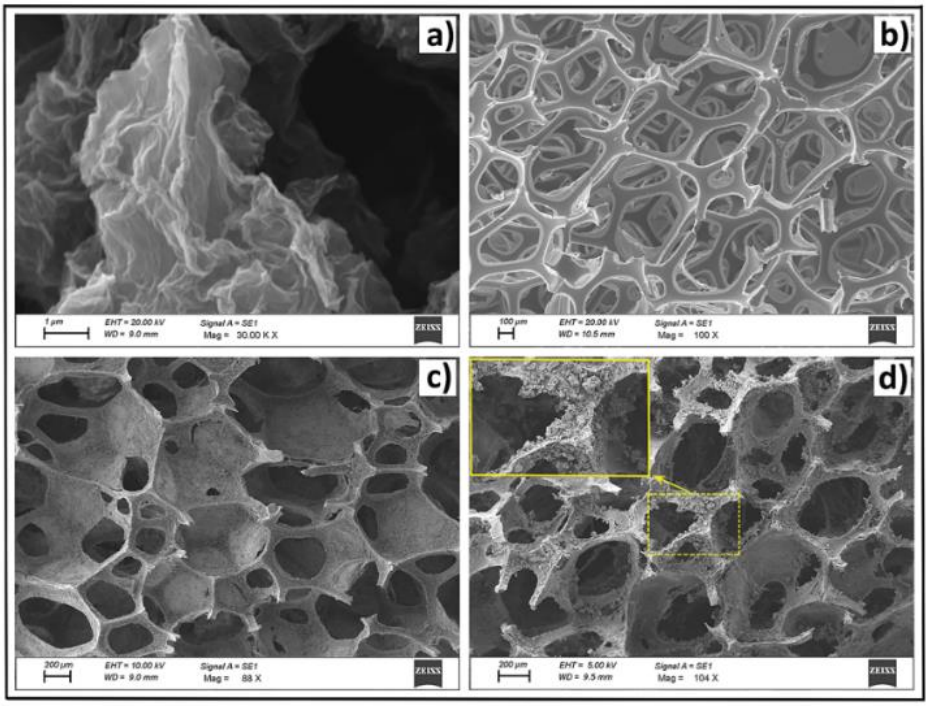

Figure 2-12 *SEM micrographs of a) N-graphene, b) bare PU foam used as substrate, c) Pt@N-graphene on PU foam, and d) carbonised Pt@N-graphene foam.* [84]

2.4.3.4 Summary of rGO and GNP support materials

All of the metal-graphene catalysts explored in these sections showed some improvement in activity, as measured by power density, when compared with the commercial Pt/C catalysts presented alongside them in their respective studies. The improvements are generally attributed to the novel nanomaterials' higher conductivities, specific surface areas and platinum utilisation. Of the many varieties of graphene, graphene nanoplatelets and reduced graphene oxides are both readily produced at scale and have been shown to be effective catalyst supports and as such have been studied with full-cell tests. When combined with a spacer to inhibit restacking, the hybrid, spaced catalysts show higher mass transport through the catalyst layer, allowing for the effective use of graphene's unique properties.

However, it is difficult to compare between studies due to the widely varying parameters used when testing novel catalysts, meaning that a true assessment of which catalyst is the best performing is impossible. Despite various

standardised testing protocols put forward by bodies such as the US DoE, in the studies detailed in this section of the review, no two studies used identical sets of parameters for obtaining polarisation curves, with operating temperatures ranging from 40 to 80 °C, cathode gases differing between pure oxygen and air, and catalyst platinum loading differing in every instance. This is most clearly reflected in the power densities obtained not for the novel materials themselves, but in the commercial Pt/C samples used to benchmark their activity. The values presented for Pt/C vary across the studies from *ca.* 178 to 700 mW cm^{-2}.

Furthermore, despite the corrosion resistance of carbon nanomaterials being a key property that drives the motivation for research into their use, only one paper followed corrosion testing protocols as set out by any fuel cell-related body, with the rest using in-house protocols that varied from each other. As a result, the improved stability of both rGO and GNPs have yet to be thoroughly demonstrated, and it is clear that there is still value in exploring alternative graphene synthesis methods.

2.4.4 Liquid-phase exfoliation to produce graphene catalyst supports

If a graphene-supported catalyst is to be durable enough to meet requirements, other synthesis methods should be explored. One that has shown promise as a scalable route to producing graphene is known as liquid-phase exfoliation[40,41,85], first demonstrated by Coleman *et al.* in 2008 via the sonication of graphite in NMP.[86] Of particular interest to this project is liquid-phase exfoliation using intercalated compounds, and specifically graphite intercalation compounds (GICs), where graphite is typically intercalated with an alkali metal and then dispersed in an appropriate solvent to produce graphenide solutions[18,19,87,88] consisting of negatively charged graphene

sheets and positively charged metal ions. A summary of this process is shown in the Figure below, taken from Ref. [89].

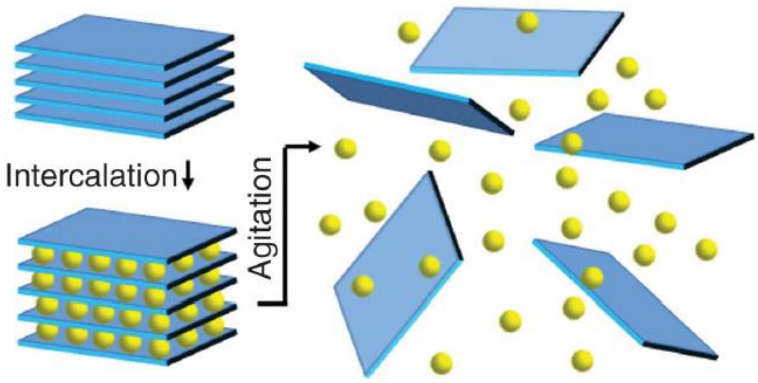

Figure 2-13 *Liquid phase exfoliation of a layered material (blue) via the intercalation of an alkali metal (yellow) and subsequent dispersion in an appropriate solvent via physical agitation, typically in the form of ultrasonication. Taken from Ref. [89].*

Important research in the area of using GICs to obtain graphenide solutions as part of a synthesis route to graphene-supported metal catalysts has been conducted by Penicaud *et al.*[90]. They first intercalate graphite by heating it with potassium at 180 degrees Celsius for five hours within an argon glovebox. This produces a GIC with one layer of potassium ions between each layer of graphite (KC_8), known as a "stage 1" graphite intercalation compound.[91] The GIC is then stirred in THF for 24 hours, and then centrifuged for thirty minutes to remove bulk material and the upper solution was retained as the graphenide solution. To obtain iron catalyst nanoparticles, an iron precursor was dispersed in THF, added to the graphenide and stirred for a further 24 hours before being removed from the glovebox. Deionised water was added, and the sample was purified by four rounds of 1 hr, 10,000 RPM ultracentrifugation and redispersion. Finally, the finished powder (Fe(np)/nCs) was obtained via freeze-drying. This process is summarised in Fig. 2-7, taken from Ref. [90].

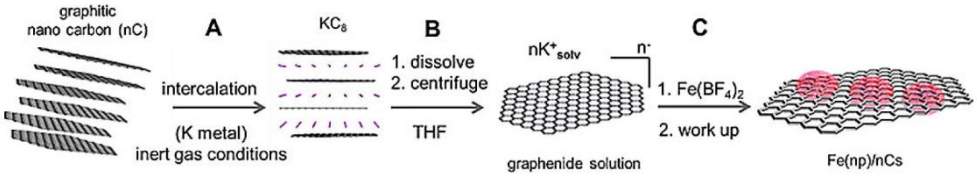

Figure 2-14 *A summary of the synthesis process used by Penicaud et al. to produce graphene sheets decorated with iron nanoparticles from a graphite intercalation compound. Taken from Ref. [*90*].*

This process results in the synthesis of graphene sheets separated and decorated by iron nanoparticles. Here, it is important to note that the metal precursor was reduced directly by the graphenide itself, rather than through the use of a reducing agent. This is advantageous as the amount of charge available to reduce the metal precursor is dictated by the finite charge of the graphenide solution. Therefore, the reaction is self-limiting, which in turn limits the size of the nanoparticles and dictates how they are formed. This differs from procedures where a reducing agent is used, where the nanoparticle size and distribution can vary greatly with the concentration and temperature. Furthermore, it leads to the formation of small nanoparticles directly on the carbon framework, resulting in a stronger binding of the nanoparticles to the surface than would result otherwise.[88] The catalytic activity of the Fe(np)/nCs for ORR was found to be higher than previously reported for Fe catalysts. This was attributed to the small size of the nanoparticles obtained via this method. However, the durability of the catalyst has yet to be reported, and the method outlined here also involves many steps of sonication and ultracentrifugation, which is similarly difficult to scale as in the synthesis methods used for rGO outlined previously. Moreover, its consequences on the presence of defects and the resultant corrosion of the material are unknown.

In contrast, work developed at UCL by Cullen *et al.*[18] has found that it is possible to obtain true ionic solutions of 2D materials without the need for any mechanical input energy, thereby avoiding the problems with scalability that arise due to repeated steps of sonication and ultracentrifugation. In the work by Cullen *et al.*, a range of layered materials, including graphite, are intercalated using the "metal-ammonia" method. The layered material is

loaded into a tube with an alkali metal, and then ammonia is condensed to form a metal-ammonia solution. In the metal-ammonia solution, electrons from the alkali metal are solvated by the liquid ammonia, and then redistribute onto the material layers. In order to balance the charge, the alkali metal ions intercalate between the layers, producing an intercalated layer material. The ammonia is then removed from the sample, leaving a powder than can be dissolved in a polar aprotic solvent in a process that is thermodynamically driven, and therefore spontaneous. This produces a stable solution of negatively charged, pristine monolayers. In the case of graphite, this solution is known as a graphenide solution.

By modifying this method, the work presented in this thesis shows that it is possible to use these graphenide solutions analogously to the work conducted by Penicaud *et al.* to directly reduce metal salt precursors. This results in the synthesis of metal nanoparticles distributed across monolayer sheets of graphene, suitable for catalytic applications. This method carries the same advantages incurred by directly reducing metal precursors with negatively charged sheets, without the disadvantages of requiring many steps of sonication and ultracentrifugation. This ensures that the supporting graphitic material remains defect-free, allowing for greater electrochemical stability to be achieved.

Chapter 3: Experimental Theory and Methods

This chapter describes the supporting theory and experimental procedures required to prepare the initial graphite, intercalate it without potassium, dissolve it in a polar solvent and react it with platinum chloride to produce graphenide-derived platinum on graphene (GD-Pt/G). The techniques used to characterise and electrochemically test GD-Pt/G are then described.

3.1 Preparation of Materials and Solvents

To synthesise the graphene-supported metal catalysts, first graphite was intercalated with potassium via the "metal-ammonia" method. This produced the graphite intercalation compound (GIC) $KC_{24}(NH_3)_{1.3}$. By adapting methods developed by Milner *et al.* and Cullen *et al.*[18,19], the GIC was dissolved in THF to produce a charged "graphenide" solution, which contains negatively charged graphene sheets and positively charged potassium ions. The negatively charged graphene sheets were then used to directly reduce platinum (II) chloride, resulting in the production of a ready-to-use ink of THF containing restacked graphene sheets decorated with platinum nanoparticles, referred to here as GD-Pt/G (graphenide-derived).

3.1.1 Outgassing of graphite

Before graphite can be intercalated with an alkali metal, it must first be outgassed to remove adsorbed water and oxygen which would otherwise cause side reactions during the intercalation process. Graphite (~325 mesh, Sigma) was first outgassed using a roughing pump (*ca.* 1 mbar) at a temperature of 300 °C, to remove the majority of adsorbed water and oxygen. After 24 hours, the graphite was moved onto a Pfeiffer turbopump and outgassed at 300 °C until the base pressure of the turbopump (*ca.* 1×10^{-6} mbar) was reached.

3.1.2 Cleaning of Glassware

All glassware was cleaned before use. Glassware was washed with de-ionised water, acetone and isopropanol and then baked in an oven at 80 °C for a minimum of thirty minutes.

3.1.3 Preparation of solvents

For purchased tetrahydrofuran to be suitable for the dissolution of graphite intercalation compounds, it was necessary to further dry the as-received anhydrous solvents using molecular sieves to remove trace water that would otherwise react with the alkali metal present in the GIC. First, the molecular sieves (Aldrich 3 Å) are regenerated to remove atmospheric water. The molecular sieves are placed in a tube furnace at 120 °C and attached to a roughing pump at a pressure of *ca.* 1 mbar.

After 24 hours, enough water is removed from the molecular sieves such that the roughing pump can be changed for a turbopump, allowing for much greater levels of vacuum to be achieved. The sieves are kept at a temperature of 120 °C until the pressure on the turbopump has reached 1×10^{-5} mbar. The temperature is then increased to 300 °C and the beads are left until the pressure on the turbopump has reached base, *ca.* 1×10^{-6} mbar. At this stage, the molecular sieves are sufficiently dry and are brought inside of the glovebox alongside the as-bought, sealed THF, where they are added to the THF so that approximately $1/5^{th}$ of the volume of the bottle is molecular sieves. The bottle is then left for at least two days to allow for the solvent to become sufficiently dry before use.

3.2 Synthesis of Graphite Intercalation Compounds

There are two common methods used to intercalate graphite with potassium, the "vapour transport" method and the "metal-ammonia" method. In the vapour transport method, graphite and potassium are mixed together, placed under vacuum, and heated to ca. 200 °C, resulting in the vaporisation of the potassium metal which then intercalates into the graphite. This produces a binary graphite intercalation compound. The "metal-ammonia" method instead dissolves the potassium into liquid ammonia, which then facilitates the intercalation of graphite and produces a tertiary intercalation compound of graphite, potassium and ammonia, as described below.

The work in this thesis focuses on the production of graphenide-derived platinum on graphene, GD-Pt/G, synthesised using a graphite intercalation compound produced via the metal-ammonia method, following earlier work by our group.

3.2.1 Metal-Ammonia Method

The "metal-ammonia" method for the intercalation of graphite uses the ability of liquid ammonia to dissolve alkali metals to produce a metal-ammonia solution. Within these solutions, the ammonia solvates a large number of electrons from the alkali metal, meaning that they have a very high reduction potential. Metal-ammonia solutions can reduce and intercalate a wide range of materials, including graphite. This occurs as the solvated electrons within the metal-ammonia solution are accepted by the π-orbitals of the graphite resulting in negatively charged graphene sheets, which are charge-balanced by the intercalation of the positive alkali metal atoms between the graphene sheets. This is described by Equation 3.1:

$$\boldsymbol{nM^{+} + ne^{-} + xNH_3 + yC \rightarrow (x-z)NH_3 + nM^{+}C_y^{n-}(NH_3)_z} \quad (3.1)$$

Where M^+ and e^- are produced as a result of being solvated by ammonia. Metal-ammonia solutions are metastable, and some of the solution will break down via the following reaction:

$$\boldsymbol{M^{+}_{(Solvated)} + NH_3 + e^{-}_{(Solvated)} \leftrightarrow MNH_2 + \frac{1}{2}H_2} \quad (3.2)$$

Potassium-intercalated graphite is a well-studied system (the stoichiometry was determined by Solin *et al.* in the 1980s [124]), and its use in producing graphenide solutions has been reported in the literature, including by work within UCL, and as such it was chosen in place of a different alkali metal.[18,19] In practice, intercalation achieved by first loading potassium and outgassed graphite powder into a "glass to metal" tube (part no. Kf25) in the molar ratio of *ca.* 1:24 K:C, based on the desired stoichiometry of the product, $KC_{24}(NH_3)_{1.3}$. small excess of potassium is used decrease the likelihood of the synthesis of higher stage GICs. The tube is then sealed with a Swagelok valve assembly, and attached to a purpose-built gas rig, shown in Figure 3-1.

With the sample tube valve still closed, the rig is evacuated to *ca.* 1 x 10^{-6} mbar using a turbopump to remove air from the system. The sample tube valve is then opened and argon within the tube is removed, leaving the graphite powder and potassium at a pressure of ca. 1 x 10^{-6} mbar.

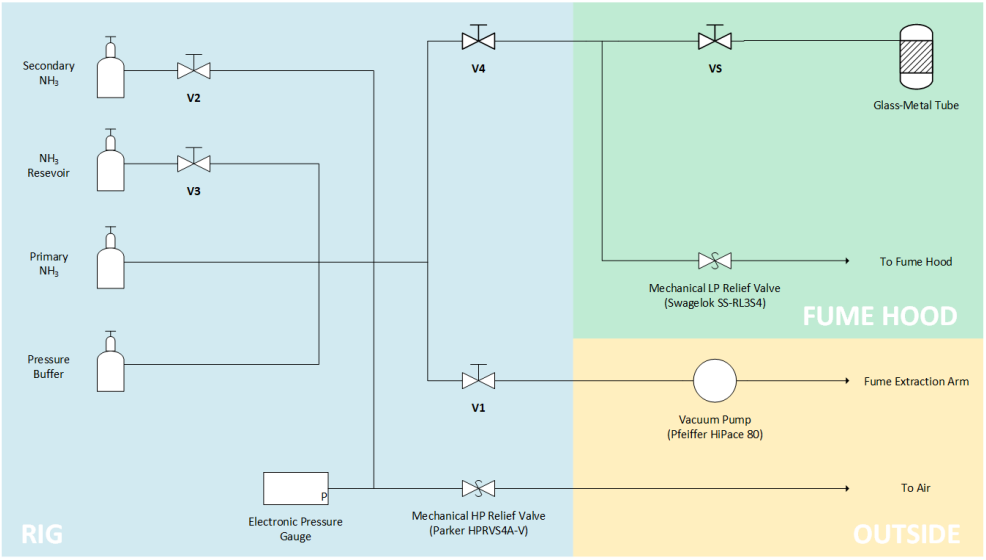

Figure 3-1 *A process flow diagram of the ammonia rig used within this work for the intercalation of graphite with potassium and ammonia, produced by Hector Lancaster*

Following the evacuation of all gases from the system, the sample tube is then placed in an isopropanol bath held at -50 °C and anhydrous ammonia gas is gradually condensed into the sample tube until the powder and metal are sufficiently covered by liquid ammonia. The liquid quickly turns a deep-blue colour characteristic of a dilute metal-ammonia solution, as shown in the photo presented in Figure 3-2 (top).[92] After approximately 24 hours, the

solution turns from deep-blue to colourless, which indicates that the intercalation has completed.

Following the completion of the intercalation, the ammonia is then transferred back into its source lecture bottle through the rig. This cryopumping process is achieved by freezing the source bottle of ammonia with liquid nitrogen, and gradually allowing ammonia to evaporate from the sample tube and freeze into the ammonia lecture bottle. Once the sample appears dry within the sample tube, the sample tube is isolated from the system by closing the sample tube valve. The frozen ammonia lecture bottle is then evacuated using the turbopump to remove any residual hydrogen gas formed by side reactions in the metal-ammonia solution.

Finally, the closed sample tube is taken from the rig and returned to the glovebox, where the graphite intercalation compound powder can be removed for later use. The blue colour of the $KC_{24}(NH_3)_{1.3}$ powder, distinct from the dark grey of the starting graphite, can be observed in the bottom photo in Figure 3-2.

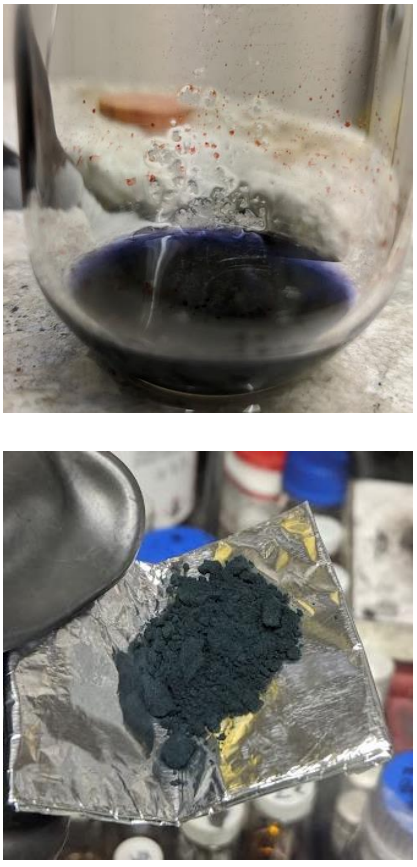

Figure 3-2 Top: *A photo of metal-ammonia solution containing potassium, liquid ammonia and graphite, in which the characteristic blue colour of the solution can be seen.* ***Bottom:*** *$KC_{24}(NH_3)_{1.3}$ powder*

3.3 Synthesis of Platinum-Graphene Catalysts

Following the intercalation of graphite with potassium, graphite intercalation compounds were dissolved in THF and then reacted with a platinum salt to produce graphene sheets decorated with platinum nanoparticles.

3.3.1 Production of Charged Graphenide Solutions

Once the graphite was intercalated, it was ready to be dissolved. In order to dissolve the graphite intercalation compound, a polar, aprotic and dry solvent is required. The solvent must be polar so that it can solvate cations and anions, and must be aprotic and dry so that the graphite intercalation compounds does not react with the solvent. The graphite intercalation compound was brought back into a glovebox and THF was added at a concentration of 5 mg ml^{-1}.

In order to increase the concentration of the negatively charged graphene platelets in a timely manner, thirty minutes of bath sonication was applied, as in a method previously reported.[19] The resultant solutions were allowed to settle in the glove box for a further 24 hours before the supernatant was extracted for use, leaving behind undissolved material. A photo of a GIC solution with a $PtCl_2$/THF solution (described in 3.3.2) is shown below.

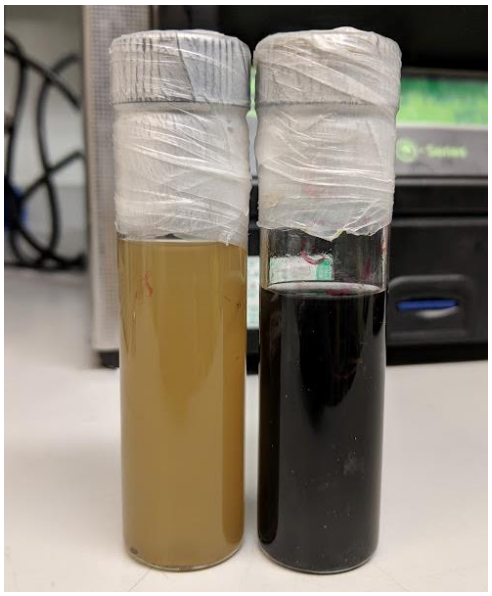

Figure 3-3 *A graphenide solution before having been left to settle (right, black) next to a $PtCl_2$ solution (left, yellow), both prepared in THF solvent*

3.3.2 Reaction of Graphenide solutions with metal salts

$PtCl_2$ was added to THF inside the glove box at a concentration of 1 mg ml^{-1}. This was then sonicated for 30 mins, keeping the temperature below 30 °C.

In the glovebox, the $PtCl_2$ dispersion was added to charged graphene liquid in excess, assuming a 100 % yield of GIC to graphenide production. The reaction is suggested to occur as described in Equation 3.1.

$$2[KC_{24}(NH_3)_{1.3}] + PtCl_2 = Pt(0) + C_{48} + 2KCl + 1.3NH_3 \quad (3.3)$$

As undispersed powder remained in the bottle the supernatant was taken from, this is an overestimate (*i.e.* the $PtCl_2$ is in stoichiometric excess). This was left to react under gentle stirring overnight. The full reaction scheme is shown in Figure 3-4.

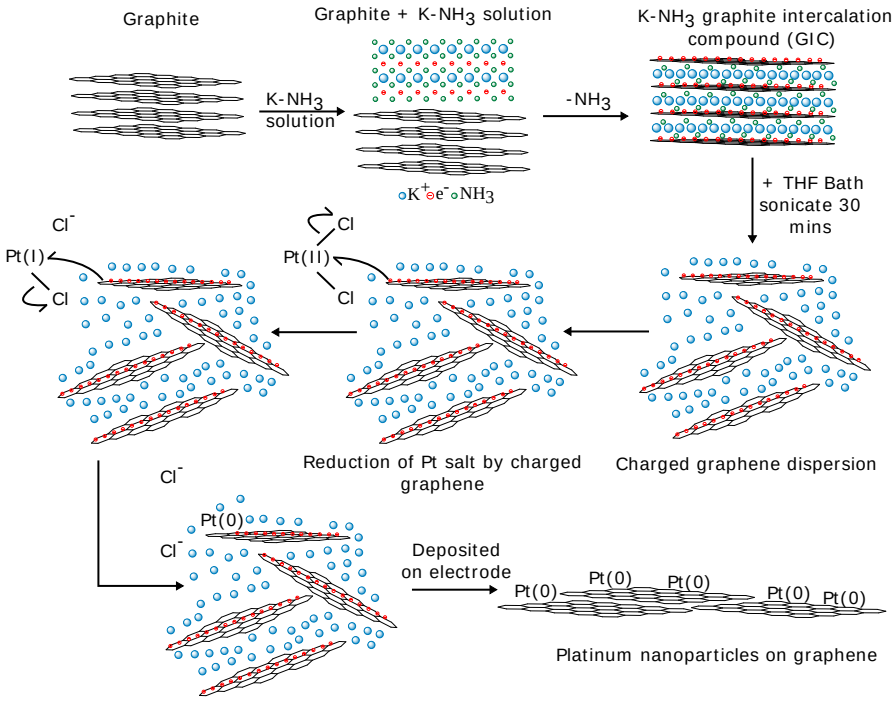

Figure 3-4 *Reaction scheme for reduction of $PtCl_2$ by graphenide to produce Pt(0) nanoparticles on graphene*

3.4 Physical Characterisation Techniques

The following section provides an outline of the underlying theory and experimental details for the various physical characterisation techniques used throughout this work.

3.4.1 Raman Spectroscopy

Raman spectroscopy is used to probe the rotational and vibrational modes of materials by scattering monochromatic laser-source light from the surface.[93] An incident photon from the laser interacts with the material, causing a perturbation to the system in which the energy of the system is increased by the energy of the incident photon, E_{photon}. The perturbed system is unstable and as such the photon is emitted, returning the system to a stable state, as presented in Figure 3-5.

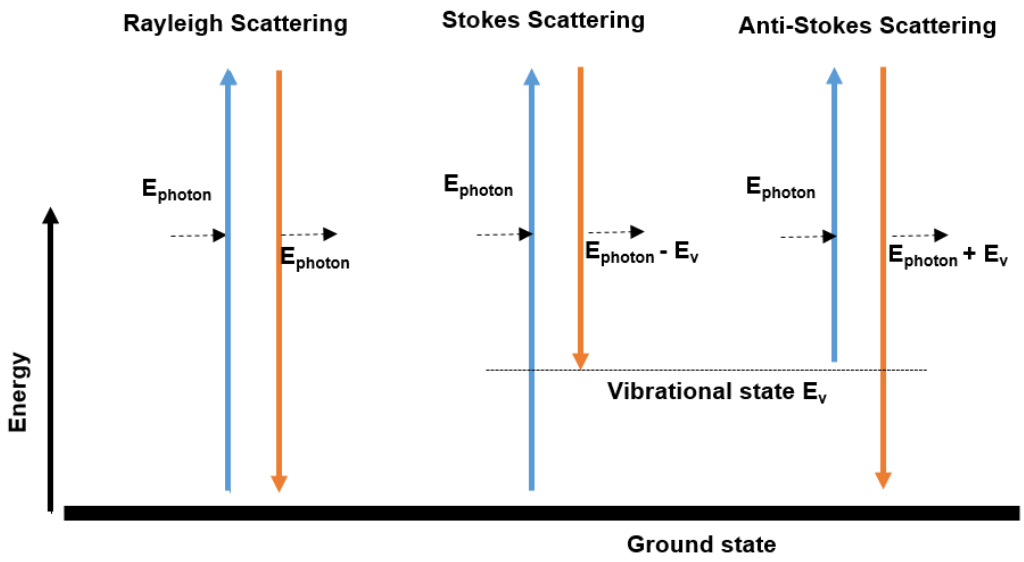

Figure 3-5 *Diagram showing the interactions of an incident photon with a material, resulting in Rayleigh, Stokes and Anti-Stokes scattering. E_v is defined as the energy of the vibrational state shown.*

In the majority of cases, the system returns to its initial state, which is known as elastic, or Rayleigh, scattering. However, it is possible for the incident photons to interact with vibrational states of the system, resulting in either the loss or gain of energy through interactions with phonons. This is known as the Stokes and anti-Stokes processes respectively. As a result, the photons are scattered inelastically, known as Raman scattering. By measuring the

intensity of the Raman scattering as a function of the difference between the scattered and incident photon energy (the Raman shift), characteristic Raman spectra can be obtained, giving insight into the material's structure and properties

Raman spectroscopy has been used extensively to study graphite and graphene in their various forms[93,94] as the shapes and intensities of the characteristic Raman peaks can be used to investigate many properties, including thickness, flake size and doping level.[95–97] An example of the Raman spectra of defect-free graphite and graphene are shown in the Fig. 3-3.[95]

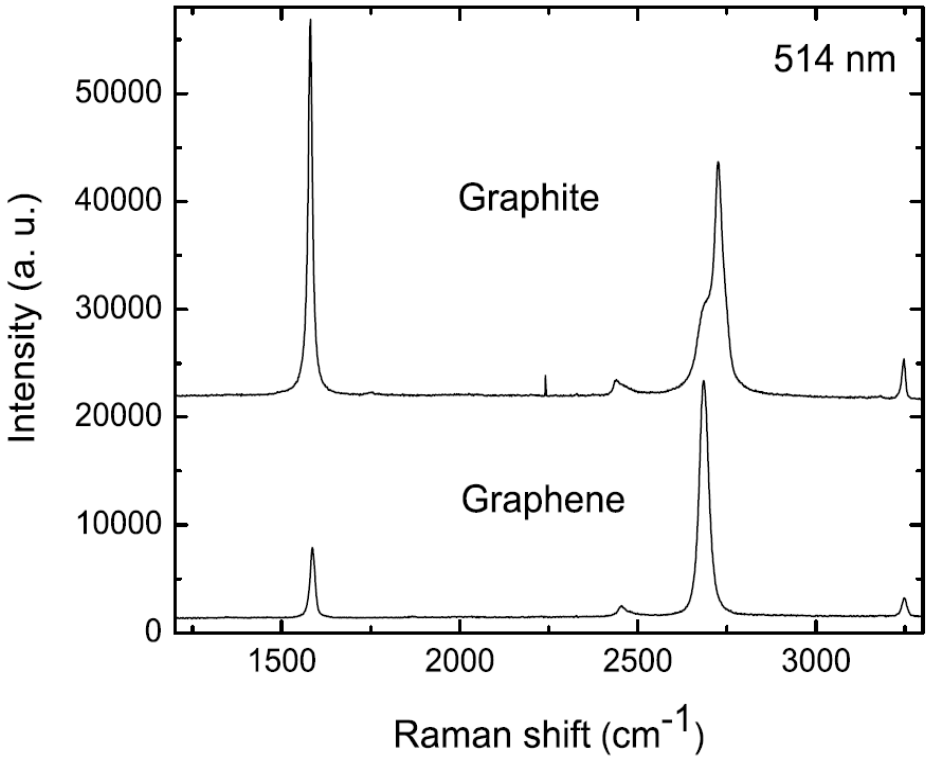

Figure 3-6 *Raman spectra of defect-free graphite and graphene, measured with a 514 nm laser. Figure taken from Ref. [*95*].*

The most prominent peaks seen in both defect-free graphite and graphene spectra are the G peak at ca. 1580 cm^{-1} and the 2D peak at ca. 2680 cm^{-1}. It is also possible to observe the D peak at ca. 1350 cm^{-1} at the edge of a defect-free sample. The G peak arises due to in-plane bond stretching of sp^2 carbon atoms and as such is observed in all graphitic materials.[94] In the case of graphite intercalation compounds doped with potassium, important in this work, it has been shown that the G peak varies significantly with doping. For

low levels of potassium doping, the G peak remains similar in full width at half maximum (FWHM) but shifts up toward *ca.*1600 cm^{-1}, such as in the case of KC_{24}. As the doping increases further, the position the peak then shifts downward toward ca. 1500 cm^{-1} and the FWHM increases to ca. 180 cm^{-1} in the case of KC_8 [97]. These trends are presented in Fig. 3-7.

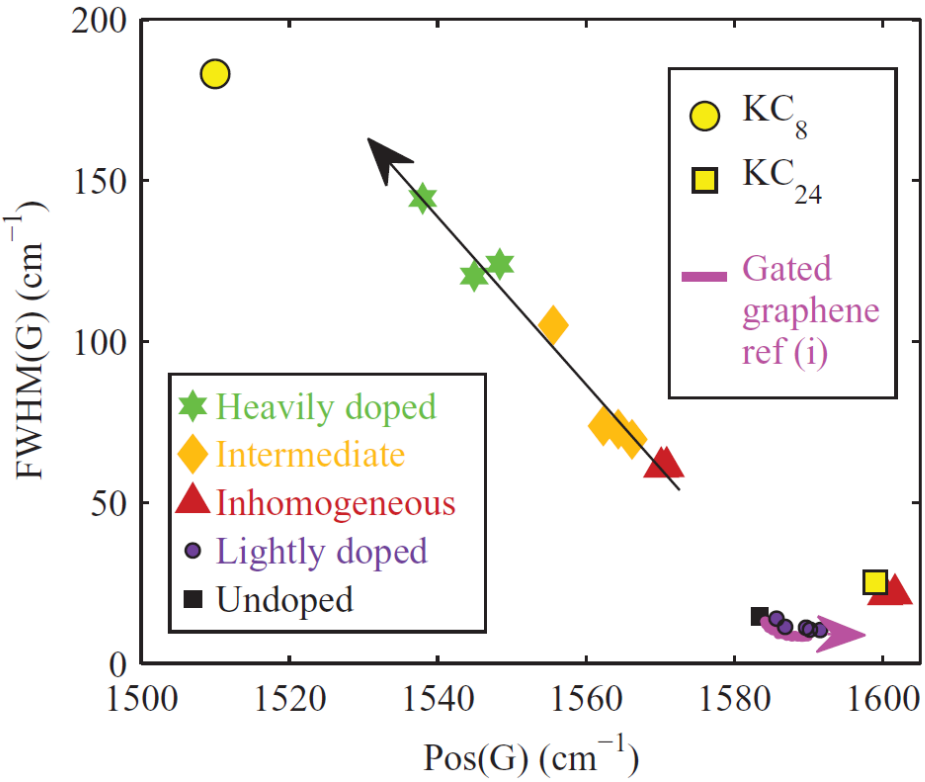

Figure 3-7 *the position and FWHM of the G peak of various potassium-doped graphite samples, ranging from lightly doped to heavily doped with potassium. Raman spectroscopy was performed with a 514.5 nm laser using a Renishaw inVia micro-Raman spectrometer. Figure taken from Ref. [97].*

It can be observed Fig. 3-8(a) that the intensity of the G peak decreases almost linearly from graphite to graphene, and as such can be used as an indicator of the number of layers present.[98] This method of determining the thickness of graphene can be advantageous as the Raman spectrum is an intrinsic property of the material and is therefore independent of the substrate the graphene sample is mounted on.

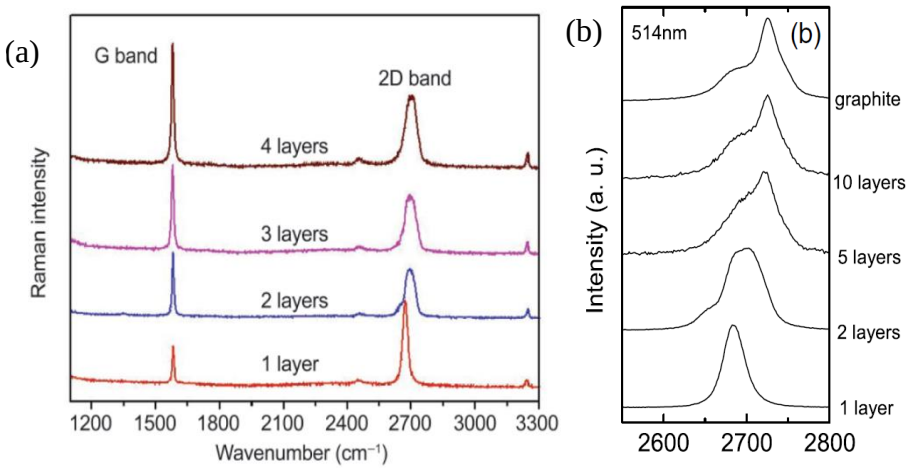

Figure 3-8 *(a) Displays the changing Raman spectra from 4 layer graphite to single layer graphene for both the G and 2D peaks, taken from Ref. [98]. (b) shows the evolution of the 2D peak in detail from bulk graphite to single layer graphene, taken from Ref. [95].*

The 2D peak is an overtone of the disorder-induced D peak[93] and its shape and position vary depending on the nature of the graphitic material. As the process involves two phonons with opposite wave vectors such that the momentum is conserved, it can arise without the presence of defects, and as such is present in all graphene spectra.[93] The change of the 2D peak with the number of layers, from bulk graphite to graphene, is shown in Fig. 3-8(b). In the case of the spectra of graphite, a primary peak is observed at *ca.* 2725 cm^{-1}, with a shoulder at *ca.* 2680 cm^{-1}. As the number of layers decreases, the peak shifts to *ca.* 2680 cm^{-1}, and the shoulder disappears such that the peak can be fitted with a single Lorentzian curve. This is also the case in turbostratically restacked graphite and graphene[93], where the FWHM is twice as large as for graphene, and its position is shifted to *ca.* 2700 cm^{-1}. Furthermore, the ratio of the G to 2D peak intensities, I(G)/I(2D), can be used to infer the number of layers present, with a value above 1 for bulk graphite.[99]

3.4.1.1 Experimental procedures and analysis

Graphite intercalation compound powders were loaded into 1 mm borosilicate glass capillaries within the glovebox, and then sealed with wax to ensure they remained air-free. Metal-graphene samples were obtained from solution via drop-casting onto glass slides which were then dried overnight in ambient conditions. Graphite powder samples were loaded onto glass slides as-received.

All Raman spectra were obtained on a Renishaw InVia Microscope (shown below) using a 488 nm laser and a 2400 l/mm diffraction grating. The intensities of all spectra presented in Section 4.1 are normalised to the G-peak of each sample.

Obtained spectra were analysed using Origin and Python code for single spectra, and Python code for maps with the help of Hector Lancaster.

Figure 3-9 *The Renishaw InVia Microscope used throughout the project*

3.4.2 X-Ray Diffraction

X-ray diffraction (XRD) is a non-destructive technique used to characterise crystalline materials. In XRD, a monochromatic X-ray is incident on the sample and interacts with the electrons of the atoms, resulting in x-ray scattering. By using an incident X-ray with a wavelength that is comparable to inter-planar distances within crystalline samples, the scattered X-rays diffracted by the planes within the crystal can interfere constructively. The resultant measured scattered X-rays produce a diffraction pattern which can be used to characterise the crystal. This phenomenon is described by Bragg's law, which arises from equating the path difference between the incident and reflected X-rays with an integer multiple of the incident wavelength, as shown in Figure 3-8.[100]

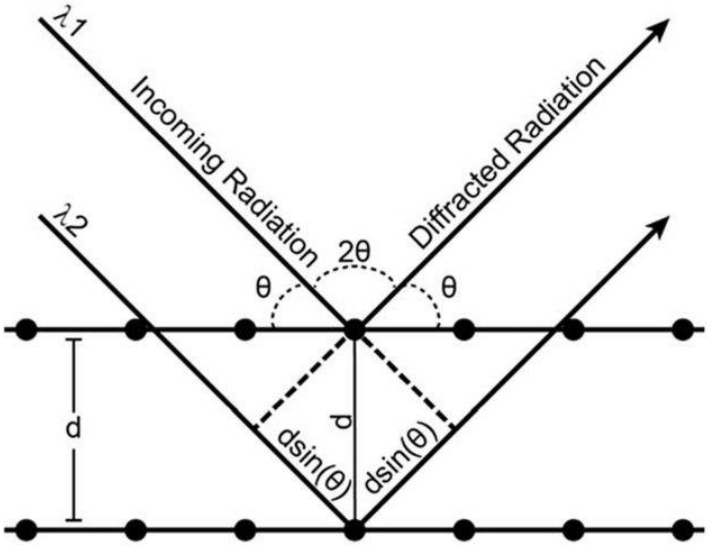

Figure 3-10 *Diagram depicting the scattering of X-Rays incident at angle from two Miller planes with indices (h k l), distance d apart. Figure taken from ref [*100*]*

Bragg's law is shown in Equation 3.4:

$$n\lambda = 2d\,sin(\theta) \quad (3.4)$$

Where n is an integer, λ is the wavelength of the incident radiation, d_{hkl} is the distance between Miller planes with indices (h k l), and θ is the angle of incidence of the X-ray. A peak in the diffraction pattern is therefore observed at each angle that corresponds to any Miller plane that satisfies Bragg's law, and as such powder diffraction is often used to ensure that there is a random selection of crystal orientations present in the sample.

By comparing the positions of measured peaks in a diffraction pattern with either theoretically calculated values or values from various crystal databases, it is possible to identify and index the peaks, allowing for information about the sample's constituent compounds to be obtained. The intensity of the measured diffraction pattern peaks is proportional to the electron density, with planes intersecting areas of higher electron density producing larger intensities.

It is possible to rewrite Bragg's law in terms of the scattering vector *Q*; this form is independent of the wavelength of the incident radiation. For layered materials such as graphite and graphite intercalation compounds, the (00L) peaks are evenly spaced in *Q*.

$$\boldsymbol{Q = k_f - k_i = 2k\,sin(\theta) = \frac{4\pi sin(\theta)}{\lambda} = \frac{2\pi}{d}} \quad \textbf{(3.5)}$$

Where k_i and k_f are the incident and scattered X-ray wave vectors respectively. This is shown graphically in Figure 3.11. [101]

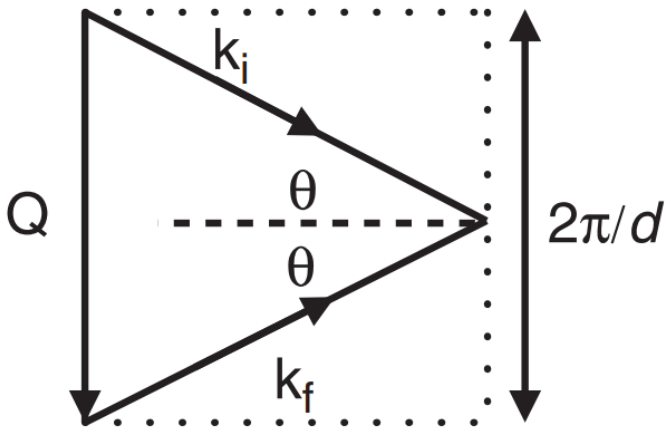

Figure 3-11 *Vector Diagram depicting the the scattering vector Q, which is the difference between the scattered wave vector k_f and the initial wave vector k_i., taken from Ref. [*175*]*

3.4.2.1 Experimental procedures and analysis

Graphite intercalation compounds were loaded into borosilicate capillaries (0.7 mm) and then sealed with wax to ensure that they remained air-free and so would remain intercalated. Capillary XRD was performed with Stoe Stadi-P Capillary Powder XRD in transmission mode with $K_{\alpha 1}$ radiation from a copper source.

Data was analysed using Origin and Rigaku smartlab software.

3.4.3 X-Ray Photoelectron Spectroscopy

X-ray photoelectron spectroscopy (XPS) is a spectroscopic technique that uses X-ray radiation to probe materials, giving quantitative information about the elemental composition of the sample. This is achieved by irradiating the sample with monochromatic x-ray radiation under vacuum, which causes electrons to be emitted due to the photoelectric effect.[102] By measuring the kinetic energy of the emitted electrons, the binding energy of the electrons can be calculated using Equation 3.X

$$\boldsymbol{E_{Binding} = h\nu - \phi - E_{Kinetic}} \quad (3.6)$$

Where E_{binding} is the binding energy of the electron, the energy of the X-ray photon is defined by the product of Planck's constant h and its frequency ν, $\boldsymbol{\phi}$ is the work function of the material and E_{kinetic} is the kinetic energy of the emitted electron.

The electrons emitted from the sample are from core atomic orbitals and as such have characteristic binding energies specific to specific atomic orbitals of each element. As such, it is possible to determine to elements present within a sample from the measured spectra of intensity plotted against binding energy. Furthermore, because the intensity is related to the number of electrons emitted and thus in turn to the amount of each element within a sample, it is possible to estimate the percentages of each element present. The binding energy of the electron emitted is also affected by the local electronic environment, meaning that information about an atom's bonding or coordination can be obtained.

XPS is limited to the characterisation of the surface level of materials, owing to the limited mean free path of the ejected free-electrons, which is on the order of nanometres. Although this can be circumvented by "etching" of the surface using Ar+ ion bombardment, the technique is best suited to samples that are roughly homogenous and where the surface is approximately representative of the sample bulk.

3.4.3.1 Experimental procedures and analysis

XPS data presented in this thesis was obtained using a Thermo Scientific K-Alpha machine, equipped with a monochromatic Al Ka X-ray source of 1486.6 eV energy, spot size 400 μm. A flood gun was used when recording XPS data to compensate for the build-up of charge on the sample surface that occurs as a result of ejected electrons.

GD-Pt/G powder was obtained by filtering the GD-Pt/G in THF solution using Omnipore PTFE membranes (0.1 μm, 47 mm). The filtered powder was then left to dry under ambient conditions. The GD-Pt/G powder was pressed onto a small square of indium, which in turn was then pressed onto the XPS sample plate for analysis.

Data was analysed using CasaXPS software. The platinum Pt 4f primary region was used in the analysis of platinum samples, which contains a doublet of two peaks corresponding to Pt 4f7/2 and Pt 4f5/2. The fitting of these peaks was confined with an energy separation of 3.35 eV and an intensity ratio of 4:3 ($4f_{7/2}$: $4f_{5/2}$) as described by spin-orbit coupling.

3.4.4 Transmission Electron Microscopy

In Transmission Electron Microscopy (TEM), a beam of high energy electrons is incident through a thin sample of the material and interacts with it. The transmitted beam can then be measured to obtain micrographs of the material, where regions with higher atomic number or thickness appear darker due to higher electron absorption. As the mass, and therefore the momentum, of the incident electrons is much higher than that of photons, the de Broglie wavelength of electrons is much smaller than that of light used in an optical microscope. As a result, the images obtained can be resolved to nanometre scales.

TEM is common in the characterisation of nanoscale materials, and allows for different structures to be identified and distinguished. Often, in the study of platinum-based catalysts, micrographs obtained via TEM are used to digitally measure the size of nanoparticles observed, and calculate particle size distributions for the materials[68,103–105].

TEM can also be used for ex-situ testing of catalyst materials through the use of "identical location" TEM (ILTEM) experiments. TEM grids with physical labels engineered into their mesh are used to locate identical areas of the material before and after accelerated stress tests, where the ILTEM grid is used as the working electrode of the electrochemical cell.[13,32] This allows for direct comparisons of matching particle distributions and support material structures, allowing for a more direct investigation of the changes in the catalyst throughout the test. An example of ILTEM of commercial Pt/C is presented in Figure 3-12, taken from Ref. [32]. The sample was imaged before and after 800 potential cycles between 0.05 and 0.5 V_{RHE}. Crystallite migration, platinum nanoparticle detachment and carbon corrosion were all observed across the sample area, and are marked in the figure by white, blue, and red features respectively.

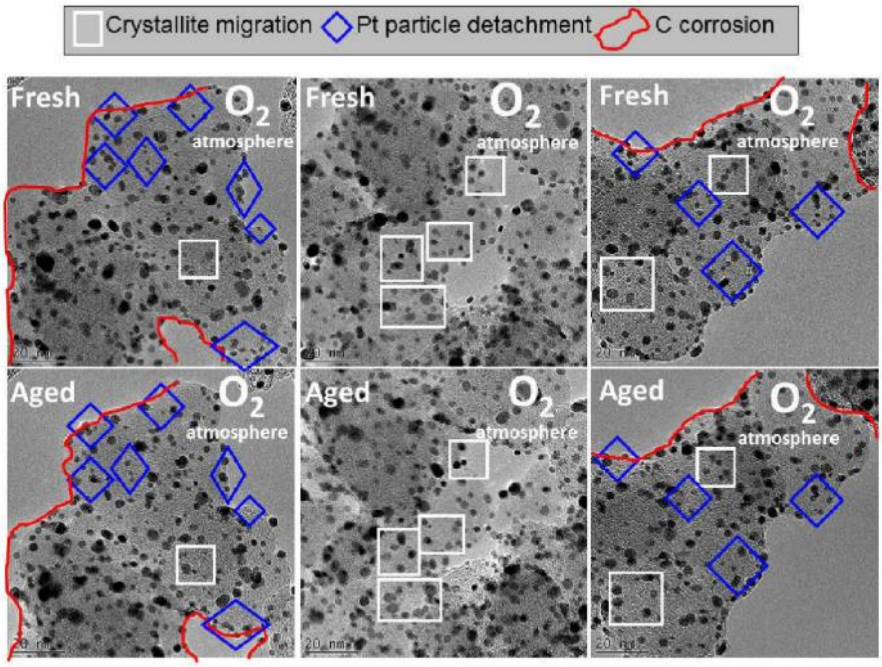

Figure 3-12 *Identical location TEM of a commercial Pt/C catalyst before and after aging, with changes in features marked (see key). Taken from Ref. [32].*

Energy-dispersive X-ray (EDX) spectroscopy is often done alongside TEM, and uses the high energy beam of electrons to excite electrons from inner shells of the atoms within the material, which are then ejected. This can cause outer-shell electrons to then release energy in the form of X-rays so that they can de-excite to fill the holes left by the ejected inner-shell electrons. The energy differences between the electron shells are characteristic of each element; by measuring the released X-rays it is possible to determine what elements are present in the sample. By measuring this data at a large number of points, it is possible to map out areas of a material by its composite elements.

3.4.4.1 Experimental procedures and analysis

Materials prepared in solution were drop-cast onto a Cu mesh holey carbon grid and allowed to dry for a minimum period of 48 hours. For ILTEM corrosion studies, gold mesh "finder grids" were used. TEM and EDX were performed on a Jeol JEM 2100 equipped with a LaB_6 source. Images were processed using Gwyddion and plot-digitiser software packages and stitched together with Inkscape. The radial distribution function was calculated by measuring the distance from each nanoparticle from the other, and then normalising the values to the average number of nanoparticles per unit area.

3.4.5 Scanning Electron Microscopy

In an SEM, a focused beam of electrons is scanned across the surface of a sample in a raster pattern. The electrons from the beam interact with the surface of the sample and are scattered elastically (back-scattered electrons, BSEs) or can interact inelastically, causing atoms on the surface of the sample to become excited. The relaxation of the excited surface atoms emits secondary electrons (SEs) of energy on the order of 50 eV. The intensity of the emitted electrons is measured as a function of location, allowing for an image to be obtained. Secondary electron emission is highly localised to the position of the incident electron beam, allowing for high resolution images of the surface to be obtained. If the hole left by the emitted secondary electron is filled by the de-excitation of a higher-level orbital electron, a characteristic X-ray can be produced, the energy of which can be measured using EDX to identify the elements present in a sample.

3.4.5.1 Experimental procedures and analysis

To prepare samples for cross-sectional SEM analysis, a small piece was cut from each MEA and set in epoxy resin. The encased samples were left to dry overnight under vacuum to reduce the presence of bubbles. Once set, the samples were mechanically polished using 280, 400, 600 and 1000 grit sandpaper (five minutes per sheet of sandpaper) before being polished using three grades of diamond polish (1, 3, 6 angstroms), 20 minutes per grade. As epoxy resin is not electrically conductive, it was then necessary to coat each sample in a thin layer of carbon using a Leica EM ACE600 machine. SEM was performed with a 20 KeV ZEISS MERLIN field emission gun scanning electron microscope (FEG-SEM) equipped with two EDS detectors. Micrographs and EDS maps were analysed and processed using Aztec software (Oxford Instruments).

3.4.6 Thermogravimetric analysis

Thermogravimetric analysis (TGA) is a type of thermal analysis in which the temperature of a sample is varied and the associated mass change is measured.[106] This can be used to observe a range of chemical and physical changes of the sample, such as phase transitions and thermal decomposition temperatures. In catalyst research, it is often used to determine the amount of metal loading present on the catalyst support material.

In a typical lab TGA machine, a small mass of the sample (*ca.* 5 mg) is loaded into a crucible, which is placed on a precision balance located inside a furnace. In a top-loading TGA, as used in this work, a thermocouple and the crucible are supported on a support rod above the balance. Depending on the required measurement, the sample is then heated in an appropriate atmosphere (such as nitrogen or air); in a top-loading TGA the gases flow upward from below the pan. The temperature-control elements are placed in parallel to the flow stream to not impede flow, with the overall design of the TGA optimised to minimise turbulence near the crucible. During the experiment, a programme of heating, isothermal holds and cooling are executed, the mass is measured, and plots of mass vs time and mass vs temperature are obtained. Generally, below 250 ˚C, physisorbed and chemisorbed water evaporates, volatile compounds decompose, and trapped gases evolve. Above this, compounds decompose at varying temperatures, leaving features that can be observed in the change in mass. The remaining material left will include non-volatile inorganic ashes and metals. Following this, if the experiment is carried out in an oxidising environment, metallic compounds can oxidise and a gain in mass can be observed.[106]

When determining the mass loading of metal nanoparticle on a carbon catalyst, the sample is heated above the combustion temperature of the carbon support, leaving only platinum in the crucible. The loading weight fraction of metal is therefore obtained by measuring the final mass at the end of the mass/time or mass/temperature plot and dividing it by the initial mass.

An example of TGA mass/temperature plots of graphitic nano carbon and nano carbon-derived metal catalysts are exhibited in Figure 3-13.[107]

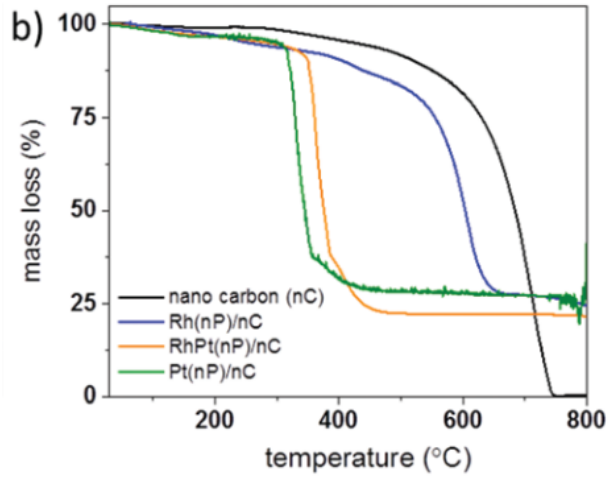

Figure 3-13 *Thermogravimetric analysis of three metal-nanocarbon catalysts, shown alongside bare nanocarbon. Taken from Ref. [*107*]*

In the plot it can be seen that the mass of each sample decreases as the temperature increases, until a final plateau is observed once only the metal remains in the crucible. While nano carbon can be seen to combust at a temperature of *ca.* 600 ˚C, the combustion of the nanocarbon metal-containing samples is lowered by the catalytic effects of the metal nanoparticles.[107]

3.4.6.1 Experimental procedures and analysis

Dry powder samples were loaded into 70 μL alumina crucibles (Mettler Toledo, Leicester, UK), with approximately 2-5 mg of powder used for each sample. TGA experiments were carried out using a TGA/DSC 3+ machine (Mettler Toledo, Leicester, UK). Samples were heated in air from room temperature to 900 ˚C at a rate of 2 ˚C min^{-1}, and then held isothermally at 900 ˚C for 6 hours. The data obtained were processed using Origin 2017 software.

3.5 Electrochemical Techniques

3.5.1 Rotating Ring Disk Electrode Experiments

In rotating disk electrode (RDE) and rotating ring-disk electrode (RDDE) experiments, the catalyst material to be tested is loaded onto the working electrode. Working electrodes are typically constructed of a cylindrical PTFE shaft with a small piece of glassy carbon inserted at the top, of which only a small flat surface is exposed, known as the "disk". The area of the disk is typically of the order of 0.25 cm^2. The catalyst material is prepared as an ink, which is dried onto the glassy carbon disk of the working electrode and dried at room temperature while being rotated to ensure an even film is deposited.[108]

The working electrode is screwed into a rotator shaft and used as part of a three-electrode cell, alongside a counter electrode and a reference electrode. For a given reduction reaction occurring at the surface of the working electrode, the opposite oxidation reaction occurs at the same rate at the counter electrode. This allows the counter electrode to provide the current required at the working electrode, and as such virtually no current flows through the reference electrode. By using an electrode with a stable and well-known potential as the reference electrode, such as the reversible hydrogen electrode, it can be used as a point from which the potential of the working electrode can be measured and controlled.[109] This allows various experiments to be performed in which the current response across the working electrode is measured as a function of applied potential. Examples of these experiments include cyclic and linear sweep voltammetry, which are discussed in the following sections.

Photos of the working electrode in its spin-drier (used to spin the electrode as the ink dries) and the three-electrode cell set up used throughout this work is presented in Fig. 3-14.

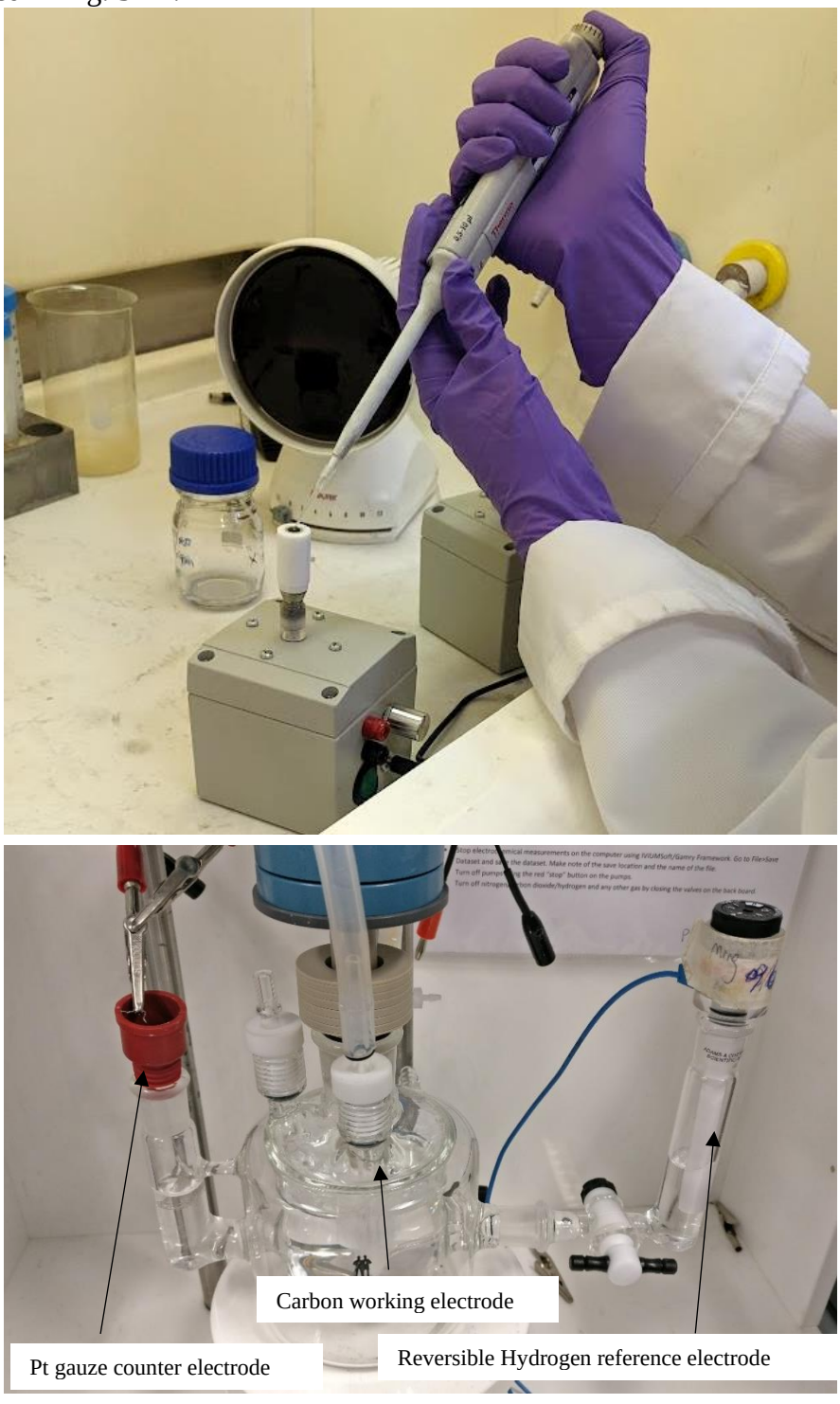

Figure 3-14 top) A photograph of examples of glassy carbon disk eletrode and rotating ring disk electrode used throughout this thesis. bottom) A photograph of the three-electrode cell used in rotating disk and rotating ring-disk experiments throughout this work.

3.5.2 Cyclic Voltammetry

In cyclic voltammetry, the potential applied to the working electrode is increased linearly from an initial value to an upper limit, and then decreased linearly to a set final limit. The current response measured at the working electrode is plotted against the applied potential, producing a cyclic voltammogram (CV) from which information can be extracted. This is because the current at the working electrode is produced as a result of the transfer of electrons due to the reaction occurring at its surface. The rate of this reaction depends on the kinetics of the reaction itself, and the rate at which electroactive material is transported to and from the surface of the working electrode.

The electron rate transfer constant for a reduction process, k_f is dependent on the applied voltage, E, and is given in Equation 3.7.

$$\boldsymbol{k_f = k^0 exp\left(\frac{-\alpha nF}{RT}\left(E - E^{0'}\right)\right)} \qquad \textbf{(3.7)}$$

Here, k_0 is the standard electron-transfer rate constant (dependent on the reaction and the electrode surface used); $E^{0'}$ is the formal electrode potential; n is the number of electrons transferred per molecule; R is the universal gas constant; T is the temperature measured in Kelvin and α is the transfer coefficient. The rate is therefore exponentially dependent on the applied potential and produces an initial steep rise in the current. Because the working electrode is left stationary for cyclic voltammetry experiments, after its initial sharp increase the current is controlled by the diffusion of reactants to the working electrode surface. This results in mass transport becoming the rate-limiting step. This produces a maximum in the current produced by the reaction, and as the depletion zone increases further, the distance reactant molecules have to travel increases. A decrease in the current follows as a result. This behaviour produces peaks in the cyclic voltammogram that are characteristic of the reactions being analysed.[109,110]

3.5.2.1 Cyclic Voltammetry of Platinum for ORR

Cyclic voltammetry is an important tool in benchmarking the activity of a platinum catalyst toward the catalysis of the ORR.[108,111] Fig. 3-15 shows a set

of typical CVs for a commercial platinum on carbon catalyst (from Ref. [108]) for a "good", "intermediate" and "bad" catalyst film on the working electrode. The CVs were recorded at 20 mVs^{-1} in 0.1 M $HClO_4$ saturated with nitrogen. It can be seen that the size of the peaks varies with the quality of the film, where a "good" film is defined as having a uniform thickness across the entirety of the disk, whereas a "bad" film's thickness varies across the surface. On the initial sweep, the first peak is due to Pt-H oxidation, followed by the formation of Pt-OH and Pt-O. O_2 evolution can be observed to begin at 1.2 V_{RHE}. On the reverse sweep, Pt-O is reduced, and Pt-H adsorption occurs, with H_2 evolution beginning to occur close to 0 V_{RHE}.

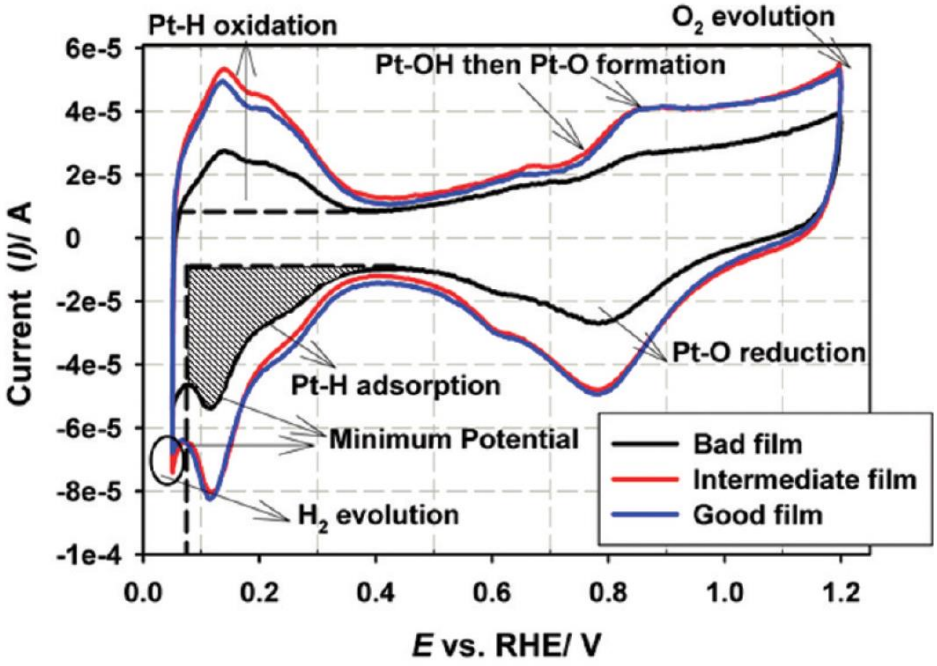

*Figure 3-15 CVs obtained from the cycling of a commercial platinum on carbon catalyst for a "good", "intermediate" and "bad" film. Figure taken from Ref. [*108*].*

Of these peaks, the most important for benchmarking catalyst activity is the Pt-H adsorption peak. By assuming that each catalytically active Pt site can have one H adsorbed, it is possible to calculate the electrochemical surface area ($ECSA_{Pt}$), measured in m^2 per gram of platinum ($m^2\ g_{Pt}^{-1}$).

$$ECSA_{Pt}(m^2 g_{Pt}^{-1}) = 10^5 . \left[\frac{Q_{H-adsorption}(C)}{210\ (\mu C\ cm_{Pt}^{-2}) .\ L_{Pt}(mg_{Pt} cm^{-2}).\ A_g(cm^2)} \right] \quad (3.8)$$

210 μC cm_{pt}^{-2} is the charge of a full coverage of clean, polycrystalline platinum and is used as a conversion factor.[108] L_{pt} is the loading weight of platinum present on the surface of the working electrode normalised by surface area, and A_g is the geometric surface area of the electrode. $Q_{H\text{-}adsorption}$ is calculated from the area contained within the Pt-H adsorption peak, as shaded in Fig. 3-7, using the following equation:

$$\boldsymbol{Q_{H-adsorption} = \frac{1}{V}\int_{E=0.075V_{RHE}}^{E=0.4V_{RHE}} I.\,dE} \qquad \boldsymbol{(3.9)}$$

Here, V is the scan rate in V s^{-1}, I is the measured current (A), and E is the potential (V_{RHE}). The ECSA is a common metric used in evaluating a catalyst, with larger ECSA suggesting better catalytic activity.

3.5.3 Linear Sweep Voltammetry

In a rotating disk electrode experiment in which linear sweep voltammetry is performed, the electrode is rotated at a set rate. Unlike in the stationary case used in cyclic voltammetry, the rotation creates a forced convection, driving reactants to the surface of the electrode. The applied potential is increased linearly from an initial voltage to a final voltage, and the current response at the working electrode surface is measured. The current is again dependent on both the mass transport, driven by the rotation, and the kinetics of the reaction itself. It can be described by the Koutecky-Levich (K-L) equation:

$$\frac{1}{j} = \frac{1}{j_K} + \frac{1}{j_L} = \frac{1}{j_K} + \frac{1}{B}\omega^{-1/2} \qquad (3.10)$$

The current densities j, j_K and j_L are the current density measured on the disk, the kinetic current density, and the mass-transport limited current density respectively[112]. Whereas j_K is independent of rotation rate ω, it can be seen from Equation 3.11 that j_L is proportional to the square root of the rotation rate, and the constant of proportionality B is defined in Equation 3.11.

$$B = 0.62D^{2/3}v^{-1/6}nFC^{*} \qquad (3.11)$$

D is the diffusion coefficient of the reactant, v is the kinematic viscosity of the electrolyte, F is the Faraday constant, and C^* is the concentration of the reactant in the electrolyte. Thus, by obtaining multiple linear sweep

voltammograms (LSVs) at different rotation rates, $1/J$ for a given potential can be plotted as a function of $\omega^{-1/2}$. The plot can then be fitted with a straight line, where the intercept and the slope can be used to derive the kinetic current and the number of electrons transferred for the chosen potential.

These values are often used as benchmarks with which to compare one catalyst sample with another, with a higher kinetic current indicating better catalytic activity. However, despite its widespread use in the literature, other work, summarised by Zhou *et al.*, has recognised that the K-L equation is only valid for one-step reactions, and that the ORR can occur via a process with more than one step.[113] This results in the gradient of the line fitted to the K-L plot displaying a dependence on both angular velocity and potential, neither of which are taken into account in the constant *B*, as predicted by the K-L equation. Furthermore, the surface coverage of catalyst on the working electrode has also been shown to affect the K-L plot.[114] Therefore, despite its common use, this method of determining the kinetic current and the number of electrons transferred isn't valid. Zhou *et al.* go on to point out that various "high-impact" papers have chosen to omit K-L analysis, in favour of focusing on the RRDE method, the background of which is explained in the following section.[112]

Garsany also describes the use of two further values to benchmark performance: mass activity and specific activity.[108] Both values are obtained by first calculating the kinetic current at 0.9 V_{RHE} (I_K) using the Equation 3.12 below, and then dividing by the mass of platinum (mass activity) or the electrochemical surface area (specific activity).

$$I_k(A) = \frac{I_{lim}(A) \times I(A)}{I_{lim}(A) - I(A)} \quad (3.12)$$

Where I_{lim} is the limiting current, and I is the current at 0.9 V_{RHE}.

3.5.3.1 Rotating Ring Disk Electrochemistry

A rotating ring-disk electrode experiment proceeds similarly to an RDE experiment, but with the addition of the measurement of the current generated across the ring electrode adjacent to the disk. The ring is held at a fixed potential, typically 1.2 V_{RHE} for ORR, such that any hydrogen peroxide produced as a result of the ORR proceeding via the two-step mechanism is oxidised to water, producing the current observed at the ring. By comparing the currents measured at the disk and the ring for a given potential, the percentage of hydrogen peroxide produced can be calculated from Equation 3.13.

$$\%(H_2O_2) = 100 \times \frac{I_R/I_D}{N} \qquad (3.13)$$

I_R is the current at the ring, I_D is the current at the disk, and N is the collection efficiency of the ring, typically provided by the manufacturer. The number of electrons transferred in the reaction at a given potential, n, can be calculated from Equation 3.14.

$$n = 4 \times \frac{I_D}{I_D + I_R/N} \qquad (3.14)$$

3.5.3.2 Tafel Analysis

A further analysis that is often conducted is known as Tafel analysis. Tafel observed experimentally[115] that the experimentally applied overpotential varied linearly the log of current density:

$$\eta = a + b \log(j) \qquad (3.15)$$

where η is the overpotential, the difference between the electrode and the standard potential (i.e. $\eta = E\text{-}E^{0\prime}$), j is the current density and b is the Tafel slope. The Tafel plot is a graph of η against $log(j)$, and as such can be fitted with a straight line with gradient ("Tafel slope") b and intercept a. Typically in the literature the gradient b is measured and compared between samples to give an insight to the reaction mechanisms.[115] Theoretically, the Butler-Volmer equation can be used to model redox reactions, such as those that

occur on the catalyst during the RDE experiment. The Butler-Volmer equation is presented below.

$$j = j_0 \left[\exp\left(\frac{\alpha_1 nF}{RT}\eta\right) - \exp\left(\frac{-\alpha_2 nF}{RT}\eta\right)\right] \quad (3.16)$$

Where j_0 is the exchange current density, $\alpha_{i=1,2}$ are the charge transfer coefficients, F is Faraday's constant, R is the universal gas constant, and T is temperature. By considering the case where the rate of the forward reaction is sufficiently larger than the backward rate of reaction, such as is the case for sufficiently large positive or negative η, one of the two exponential terms in the Butler-Volmer equation will become negligible. By then rearranging the Butler-Volmer equation for η and by comparing it with Equation 3.15, we find that

$$a = \frac{RT}{\alpha_i nF}\ln j_0 \quad (3.17)$$

$$b = -\frac{RT}{\alpha_i nF} \quad (3.18)$$

Thus, from the Tafel slope and intercept it is possible to determine the exchange current and the charge transfer coefficient. However, the vast majority of the literature tends to simply calculate the value of the Tafel slope, where a lower Tafel slope indicates a higher value of α_i, and therefore better catalytic activity.[115–122]

3.5.3.3 Linear Sweep Voltammetry of Platinum for ORR

Typical linear sweep voltammograms for a commercial platinum on carbon catalyst are shown below, for "good", "intermediate" and "bad" films at various scan rates.[108]

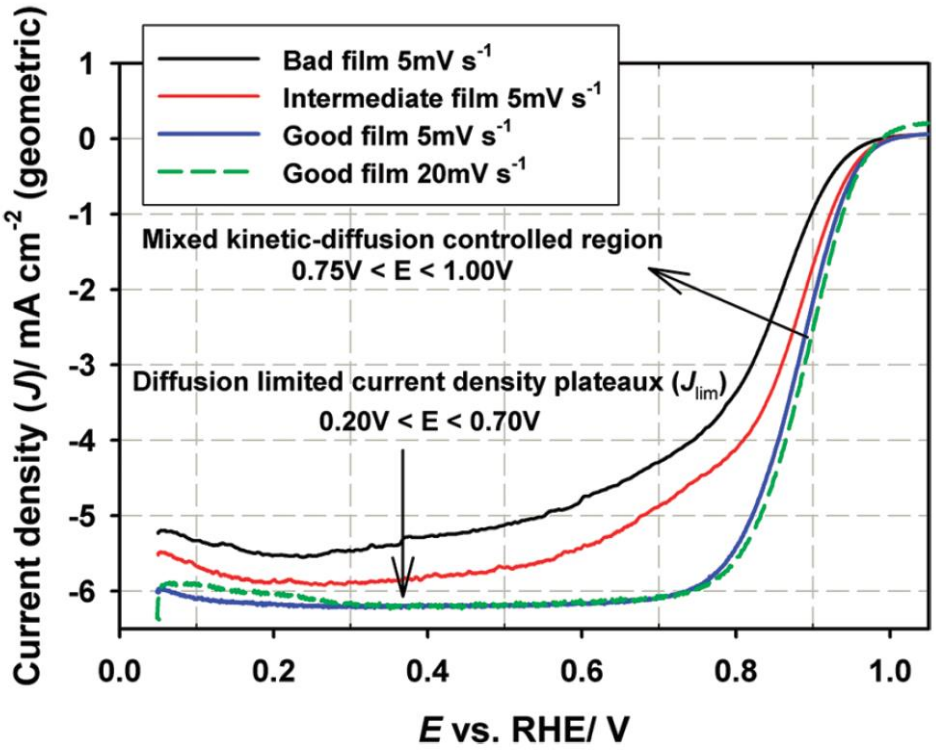

Figure 3-16 *LSVs obtained from the analysis of a commercial platinum on carbon catalyst for "good", "intermediate" and "bad" films at different scan rates. Figure taken from Ref. [*108*].*

Very close to the onset potential, the potential at which the current density first increases away from 0 mA cm^{-2}, only a small amount of reactant is required and as such the reaction is not limited by the ability of forced convection to provide reactant: the reaction is therefore only limited by its kinetics.[10] Following this, the curve enters a mixed kinetic-diffusion controlled region, in which the mass-transport has an increasing impact on the rate of the reaction, before reaching the diffusion-limited current (J_{lim}) plateaux, where the mass-transport becomes the rate-limiting factor. Typically, the onset potential, the half-wave potential $E_{1/2}$ (the potential where the current density is half of J_{lim}) and the diffusion-limited current density J_{lim} are used to compare the LSVs of various samples. The "good" film shown in Fig. 3-16 shows the best catalytic activity of the set, as the onset potential and $E_{1/2}$ are the largest, indicating superior kinetics. Furthermore, its

J_{lim} is the largest and the region in which the reaction is limited by mass-transport shows a clear plateaux, indicating better transport of reactant through the catalyst materia.[108,111]

The small improvement in activity observed between the 5 mV s^{-1} and 20 mV s^{-1} scan rates is in part due to contamination of the electrode at lower scan rates and to hysteresis in the adsorption of OH on Pt, resulting in lower activity toward the ORR at lower scan rates.[111]

3.5.4 Rotating Ring Disk Electrochemistry Experimental Procedures and Analysis

In the results presented in Chapter 5, a 40 µl aliquot of metal-graphene catalyst THF ink was dropped onto a 0.1963 cm^2 glassy carbon electrode, polished (using Al_2O_3 micro-polish, Bueler) and then 8 µl of 0.02 wt% Nafion ionomer solution was added to the surface of the electrode, serving as a binder. In Chapter 6, after filtering, GD-Pt/G-2 powder was dispersed in a standard solution of 0.02 wt% Nafion in 50%/50% water/IPA mixture at a concentration of 2 mg ml^{-1} via 30 minutes of sonication. 10 µl of the resultant ink was dropped on to the glassy carbon electrode, and no further Nafion was added. In all cases, electrodes were dried using a rotating holder to improve film quality.[108]

This was used with a standard three-electrode cell, containing 0.1 M $HClO_4$ electrolyte solution, a reversible hydrogen electrode (Gaskatel) and a Pt mesh counter electrode. For commercial Pt on carbon (Johnson Matthey HiSpec4000, 40wt% platinum) samples, 1 mg of the catalyst was dispersed in 1 ml of 0.02 wt% Nafion in 75%/25% water/IPA mixture. A loading of 35 μg_{Pt} cm^{-2} was deposited onto the glassy carbon electrode.

Working electrodes were first electrochemically activated via rapid cyclic voltammetry cycles (500 mV s^{-1}) between 0.05 V_{RHE} and 1.2 V_{RHE}, until no further change was observed in the CV features (typically 50-100 cycles). Following the activation step, cyclic voltammograms were obtained by cycling the working electrode between 0.025 V_{RHE} and 1.2 V_{RHE} at room temperature, under N_2 flow, at a scan rate of 20 mV s^{-1}.

In order to investigate ORR activity, linear sweep voltammetry was performed at room temperature under constant O_2 flow at 1600 RPM. The scans were performed at 20 mV s^{-1} between -0.01 V_{RHE} and 1 V_{RHE}.

Rotating ring-disk experiments were performed by obtaining linear sweep voltammograms across the disk of the electrode as described above, while the chronoamperometric hold of 1.2V was applied to the ring of the electrode. The collection efficiency of the electrode is determined by the ratio of the surface area of the ring to the surface area of the disc, and was 37%, as provided by the manufacturer.

To examine the durability of the platinum nanoparticles and the graphene support, corrosion experiments were carried out across both 0.6-1 V_{RHE} and 1-1.6 V_{RHE} ranges. Here, the working electrode was cycled at 100 mV s^{-1}, and then at various intervals a full CV was taken between 0.025-1.2 V_{RHE} at 20 mV s^{-1}. A total of 30,000 cycles was carried out for each durability test, as specified by, or surpassing, DoE targets.[35,46,58]

Data was analysed using Gamry Echem software and Python code.

3.6 Fuel Cell Membrane Electrode Assembly Testing

In fuel cell testing, the novel catalyst material is deposited onto a GDL to produce the cathode-side catalyst layer.[21] A commercial Nafion membrane is then sandwiched between an anode-side commercial Pt/C catalyst layer and the novel catalyst material cathode-side catalyst layer and hot pressed together, to produce the membrane electrode assembly. This is then assembled with the other components of the fuel cell, as described in Chapter 2, ready for testing.

The primary method for bench marking the in-situ activity of an MEA is the polarisation curve, in which a current density is drawn from the cell and the voltage response is measured. The regions of the polarisation curve are covered by Section 2.1.3 in this thesis. By multiplying the potential measured by the current density at each step, a power density curve can be derived. The peak power density or the current density at 0.3 V are commonly used to compare MEAs.[21] Shown in Figure 3-17 is an example of a polarisation curve and its associated power density curve for a fuel cell with a commercial Pt/C catalyst cathode, obtained in this work at a platinum loading of 0.2 mg_{pt} cm^{-2}. The full operating conditions are detailed in the following experimental procedures section.

The features of the polarisation curve are intrinsically tied to the properties of the MEA, including the materials used and the structures obtained upon preparation of the MEA. Comparing the differences between polarisation curves obtained from different MEAs allows for insight to be derived into the limitations of one MEA from the other.[21]

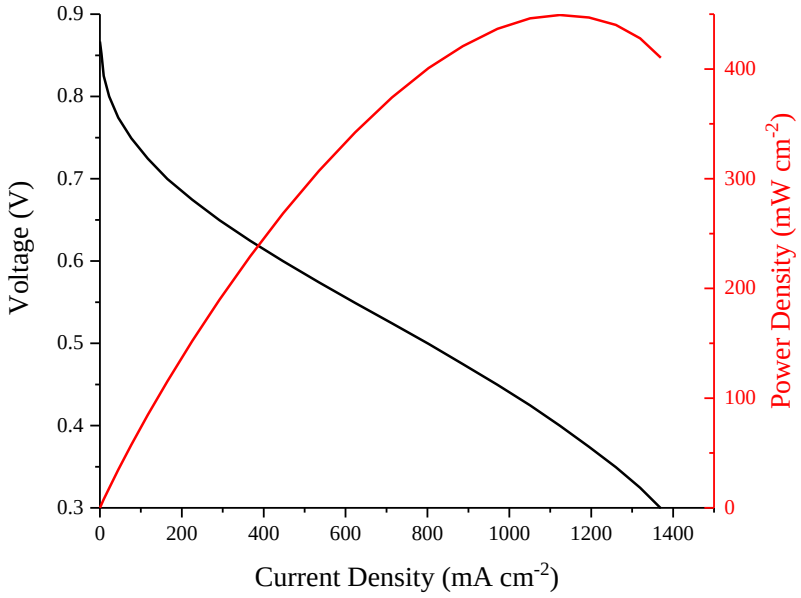

Figure 3-17 *an example of a polarisation curve and associated power density curve for a fuel cell with a commercial Pt/C catalyst at both the anode and the cathode. The cell was constructed using a 25cm^2 MEA, and operated under H_2/air with no backpressure, at a temperature of 80 °C. The loading of platinum on the cathode used was 0.2 mg cm^{-2}.*

3.6.1 Membrane Electrode Assembly testing experimental procedures

Graphenide-derived Pt/G powder was obtained via filtering of solutions, as described in Chapter 3. Commercial Pt/C was used as purchased (40wt% Pt, Vulcan XC72R, Alfa Aesar, Ward Hill, Mass., USA). To produce the catalyst ink, catalyst powder, Nafion solution (11wt% Nafion, Dupoint Fluoroproducts (Richmond, VA, USA), deionised water and propan-2-ol were added to a 100 mL Mason Jar and were ultrasonicated using a probe sonicator (Fisherbrand Model 505 Sonic Dismembrator, Fisher) in intervals 5s on, 5s off for two minutes (1 minute of sonication in total). The final ink was composed of 8:10 Nafion:carbon by weight, 1:1 ratio of water to propan-2-ol and an overall concentration of 1 mg_{solid}/ml. Following a method developed by Suter *et al.*, sacrificial urea spacer was added to one of the sample inks before sonication in the mass ratio of 2:1 urea:GD-Pt/G, which was the optimum ratio found by Suter *et al.* in work conducted on a similar graphene-supported catalyst. [123]

To produce the cathode side of the MEA, commercial gas diffusion layers H23C7 (Freudenberg, Weinheim, Germany) were cut to be slightly larger

than 5 x 5 cm^2 and placed on the bed of an ultrasonic robotic spray coater system (Sono-Tek ExactaCoat, Sono-Tek Corporation, NY, USA). Immediately after preparation, catalyst inks were sprayed directly onto GDLs across an area of 25 cm^2 at a rate of 0.4 mL min^{-1}, with the bed of the spray coater system held at 100 ˚C to aid drying of the ink. The change in mass of the GDL was measured at periodic intervals during spraying, with spraying stopped when a loading of ca. 0.2 mg_{Pt} cm^{-2} was achieved. The GDE prepared with ink containing urea was then left to soak in deionised water overnight to dissolve the urea crystals, leaving voids within the graphene structure in their place, before being left to dry at room temperature for 24 hours. The catalyst ink was sprayed onto a GDL rather than directly onto the membrane to avoid causing the membrane to swell during fabrication, particularly in the case of the sample with urea added in which the coated GDL is soaked in water overnight.[123]

Following the preparation of the cathode-side GDEs, MEAs were prepared by hot pressing a commercial 0.4 mg_{pt} cm^{-2} HyPlat GDE, Gore Select membrane and the cathode-side GDE together. The GDEs and membrane were cut by hand, with the GDEs cut to 5 x 5 cm^2, and the membrane cut slightly larger to ensure that it completely separated the GDEs. Hot pressing was performed at a pressure of 360 psi at 150 ˚C for 3 minutes. Hot pressed MEAs were then assembled with current collector plates, flow field plates and end plates as described in Chapter 2. The cell assembly was then sealed with bolts at a torque of 4 Nm.

Fuel cell testing was carried out using a Scribner 850e test system under air/H_2 at 100% relative humidity, 80 ˚C, without back pressure. The H_2/O_2 stoichiometric flow was set to 1.5/3. Before testing, it is necessary to condition the cell to "activate" the MEA by instigating physical changes, such as hydrating the ionomer content.[21] To achieve this, cells were initially purged with Ar/Ar for 10 minutes, followed by an OCV hold under air/H_2 for 5 minutes. A combination of CVs (0.06 – 1 V, 20 mV s^{-1}) and "fast" polarisation curves (0 – 0.3 V, 0.05 V pt^{-1}, 10 sec pt^{-1}) were performed until the current density stabilised. "Slow" characterisation polarisation curves were then obtained at 0.05 V/pt and 30 s/pt.

Chapter 4: Characterisation of GD-Pt/G

In this Chapter, the results of characterisation studies of potassium-intercalated graphite and graphene-derived platinum nanoparticles supported by graphene are presented.

4.1 Potassium-Intercalated Graphite

The first step in the synthesis of GD-Pt/G is the intercalation of graphite with potassium and ammonia, as detailed in Section 3.2.1. X-ray diffraction and Raman spectroscopy was used to ensure that graphite powders were intercalated before dissolution and reaction.

4.1.1 X-Ray Diffraction

Figure 4-1 presents X-ray powder diffraction patterns in Q space, obtained for the initial starting graphite used in this work, and graphite powder intercalated with potassium and ammonia.

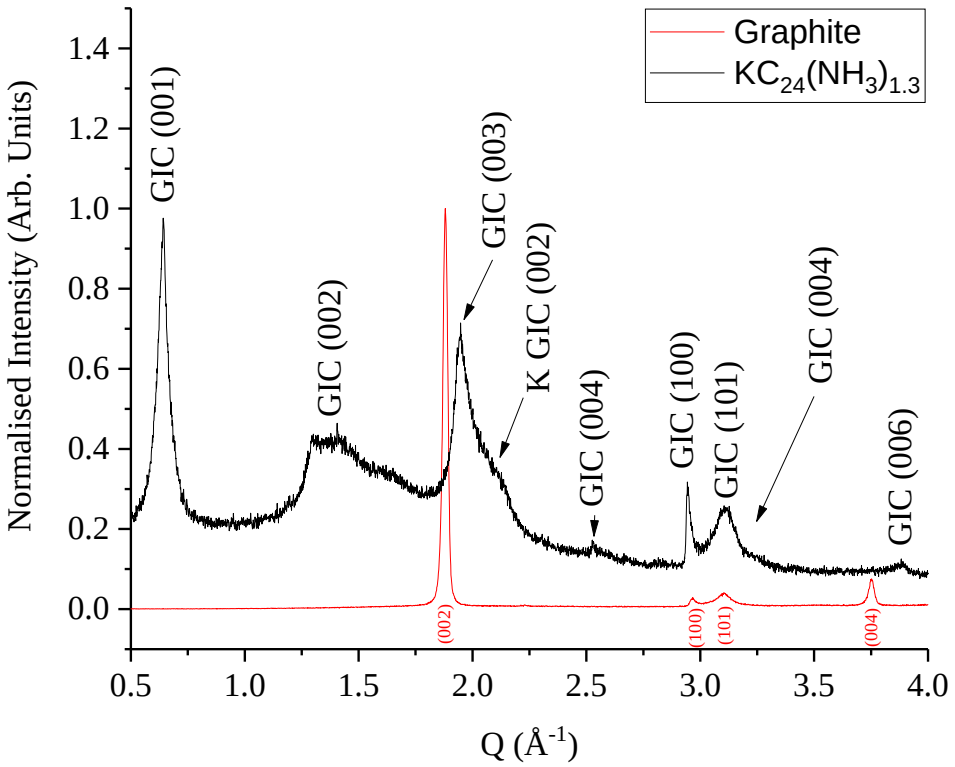

Figure 4-1 *Powder XRD patterns obtained for initial starting graphite and graphite intercalated with potassium and ammonia. Graphite planes are labelled in red. Intercalation compound planes are labelled in black: labels prefixed GIC correspond to K-NH_3 ternary GIC planes, and KGIC to binary K GIC planes*

The powder XRD pattern of starting graphite powder displays four peaks in this Q range, the most intense of which is the (002) peak at 1.88 $Å^{-1}$, corresponding to an interlayer spacing of 3.3 Å. The powder XRD pattern of the intercalated compound is more complex, with features that appear to be a convolution of reflections associated with both binary potassium GICs and ternary potassium-ammonia GICs, the labels of which are prefixed with KGIC and GIC respectively in Figure 4-1. The peaks associated with the (00L) planes of the ammoniated graphite intercalation compound are present at regular intervals of 0.64 $Å^{-1}$, the lowest of which is the (001) plane, corresponding with a distance in the c-direction of the unit cell of 9.8 Å. This distance is consistent with a stage two graphite intercalation compound where the galleries are occupied by potassium and ammonia ions, resulting in gallery spacing of 6.5 Å between the pairs of bilayer graphene.[124]

The small shoulder in the peak at ca. 2.2 $Å^{-1}$ is likely to be the reflection of the binary K-GIC (KC_{24}), which suggests that the powder is not entirely homogenous, and that there is a mixture of both binary and ternary GIC present. It is also possible that there is a mixture of staging present within the sample. Although peaks in Figure 4-1 have been indexed with labels corresponding to the stage 2 compound planes, a number of the planes corresponding to the stage 1 compound closely overlap in position with the stage 2 planes, and therefore the features in the powder XRD pattern may be a convolution of stage 1 and stage 2 compound peaks.[124] As such, Raman spectroscopy was also used to further investigate the graphite intercalation compound, the results of which are presented in the following section.

4.1.2 Raman Spectroscopy

Typical spectra measured for graphite and $KC_{24}(NH_3)_{1.3}$ are presented in Figure 4-2.

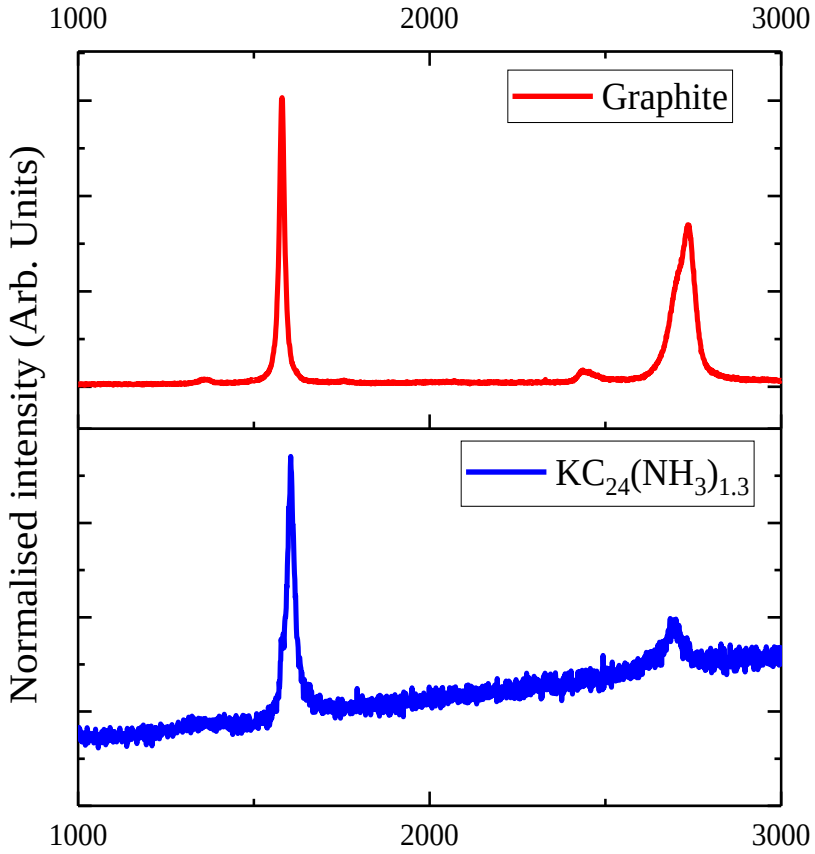

Figure 4-2 *Representative Raman spectra of the starting graphite (red) and $KC_{24}(NH_3)_{1.3}$ GIC (blue).*

In graphite, the G band, associated with in-plane bond stretching, can be observed at ca. 1580 cm^{-1} [93]. In the case of the GIC sample, the G peak is shifted to ca. 1605 cm^{-1}, with a small shoulder present at ca. 1580 cm^{-1}. This shift arises due to the doping of the material with potassium, with the shoulder indicating the presence of some inhomogeneity in the doping of the material.[97] The inhomogeneity in the doping of the material may explain why some of the powder produced during the intercalation process does not dissolve, and settles out to the bottom of the vial after sonication: any graphite that is not intercalated would not be negatively charged, and so would not remain suspended by the polar solvent.

The 2D peak, observed at ca. 2700 cm^{-1}, is an overtone of the disorder-induced D peak[93] and its shape and position vary depending on the nature of the graphitic material (see Section 3.4.1). Furthermore, the ratio of the G to 2D peak intensities, I(G)/I(2D), can be used to infer the number of layers present, with a value above 1 for bulk graphite.[99] In the case of the spectra of graphite presented in Figure 4-2(a), a primary peak is observed at *ca.* 2725 cm^{-1}, with a shoulder at ca. 2680 cm^{-1}. The 2D peak present in the spectrum of $KC_{24}(NH3)_{1.3}$ is much less intense than the 2D peaks observed in the graphite spectra. This is because the double resonance process which produces the 2D peak is greatly supressed for charged graphene layers, and isn't typically present in $KC_{24}(NH3)_{1.3}$.[97,125] Its presence in Figure 4-2 is further evidence to suggest the powder was not homogenously doped during the intercalation process.

To further investigate this inhomogeneity, a map of Raman spectroscopy measurements was taken. At each point in the spatial map, the convoluted G peak was fitted with two curves, the first of which was found to be centred on average 1578 cm^{-1}, and the second at 1604 cm^{-1}, corresponding with the "graphitic" G peak and the "GIC" G peak respectively. The intensity of each of the peaks was measured and the ratio of the graphitic G peak and the GIC G peak at each spatial point is shown as a map in the Figure 4-3.

A section of the map is shaded grey because the experiment had to be interrupted and so no data was taken at these coordinates. While it can be observed that in the spatial map the graphitic G peak at 1580 cm^{-1} was present in the spectra in every data point, its associated intensity was always lower than that of the GIC G peak: the mean intensity ratio was 5.2 with a standard deviation of 1.9. Therefore, it was decided that the powders contained sufficient intercalated graphite that they could be used for further reactions.

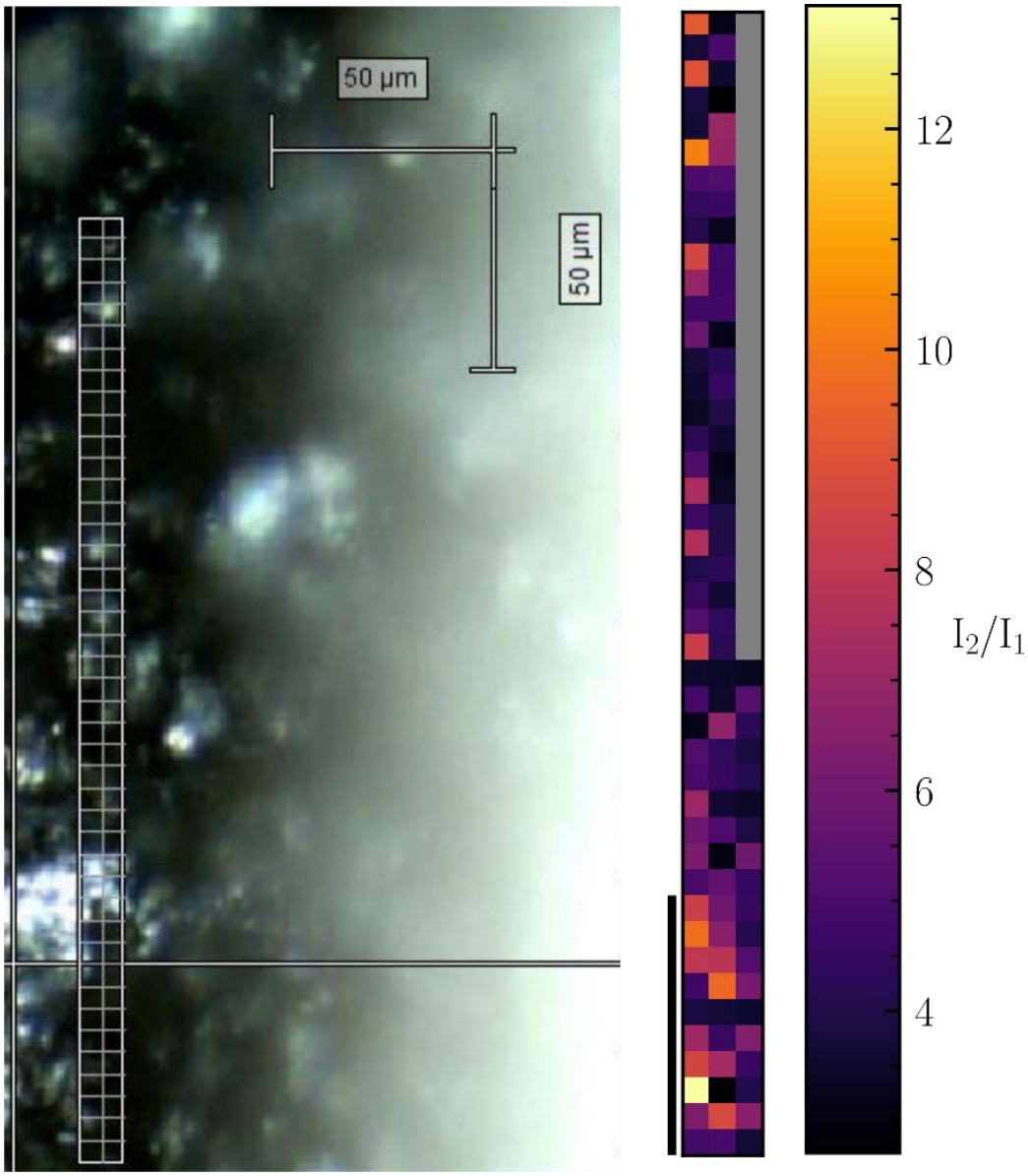

Figure 4-3 *Spatial map of potassium-intercalated graphite. An image of the powder within a capillary with the map grid is shown on the left, with the associated map on the right, with each square representing the ratio of the internsities of the intercalated graphite G peak (I_2) to the graphitic G peak (I_1)*

4.2 Graphenide-derived Platinum on Graphene

Following the intercalation of graphite with potassium and ammonia, the intercalation compound was dissolved in THF and reacted with platinum (II) chloride, as described in Chapter 3. The characterisation of the resultant material is presented in the following sections.

4.2.1 Raman Spectroscopy

Raman spectra of the starting graphite powder, the intercalated GIC $KC_{24}(NH_3)_{1.3}$ compound, and GD-Pt/G produced via the reaction of the GIC with $PtCl_2$ are exhibited in Figure 4-4.

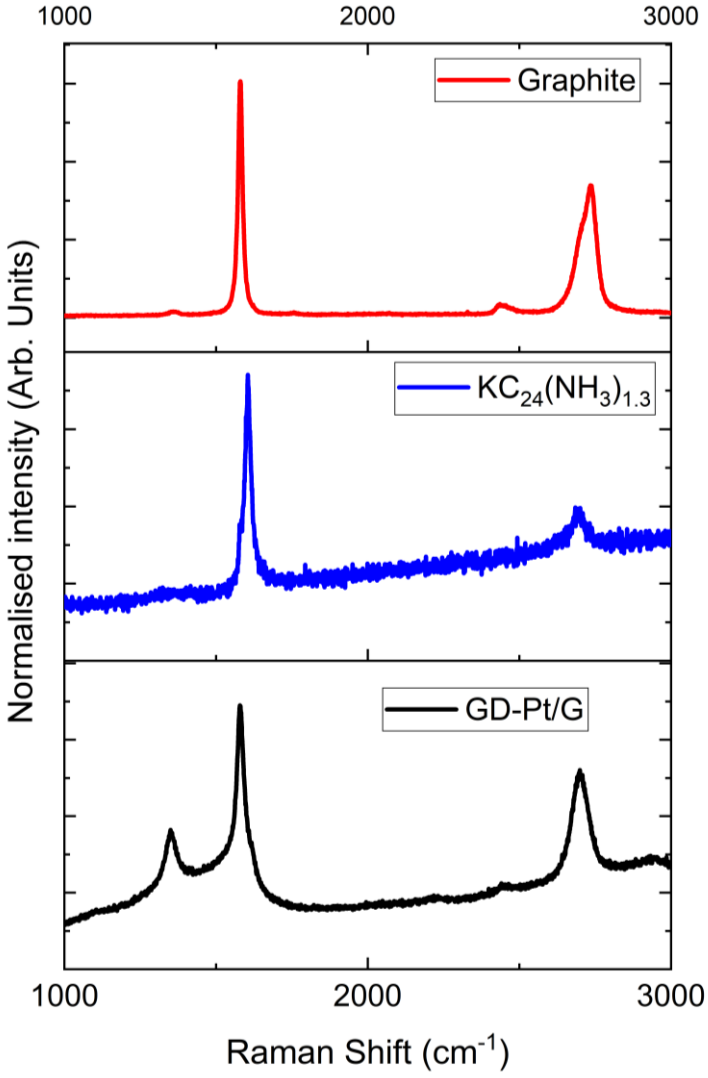

Figure 4-4 *Raman spectra of the starting graphite, the $KC_{24}(NH_3)_{1.3}$ graphite intercalation compound and GD-Pt/G*

It can be seen that for the GD-Pt/G spectra, the shoulder seen in the 2D peak of graphite is missing and the peak instead can be fitted with a single Lorentzian peak centred on *ca.* 2700 cm^{-1}, with a FWHM of *ca.* 67 cm^{-1}. The measured I(G)/I(2D) ratio was found to be *ca.* 0.57. This suggests that the Pt/graphene sample is composed of turbostratically restacked few-layer graphene.[93,95,126,127].

In the GD-Pt/G spectra, the D peak can be observed at *ca*. 1350 cm^{-1}. The introduction of defects throughout the synthesis process and the introduction of platinum nanoparticles are likely to be responsible for the increase in D peak intensity relative to the starting material and the potassium-doped graphite.[56,103] The ratio of the intensities of the D to G peak, I(D)/I(G), increases with disorder[128], and by comparing the integrated areas under the peaks, was found to be *ca.* 0.33. This is smaller than an I(D)/I(G) ratio of 1, therefore indicating a high level of graphetisation.[53,129,130] Furthermore, the I(D)/I(G) ratio for GD-Pt/G is smaller than that of similar catalysts seen in the literature in which rGO is used as the support material.[53,56,103,122,131] It is known that during cycling, the mechanism for carbon corrosion begins at defect sites in the supporting carbon material, and as such a smaller number of defects is desirable as it should result in better resistance to corrosion via this mechanism.[68]

4.2.2 Transmission Electron Microscopy

Figure 4-5 presents TEM micrographs of GD-Pt/G, obtained via the reaction of sonication-aided dissolution of $KC_{24}(NH_3)_{1.3}$ with $PtCl_2$.

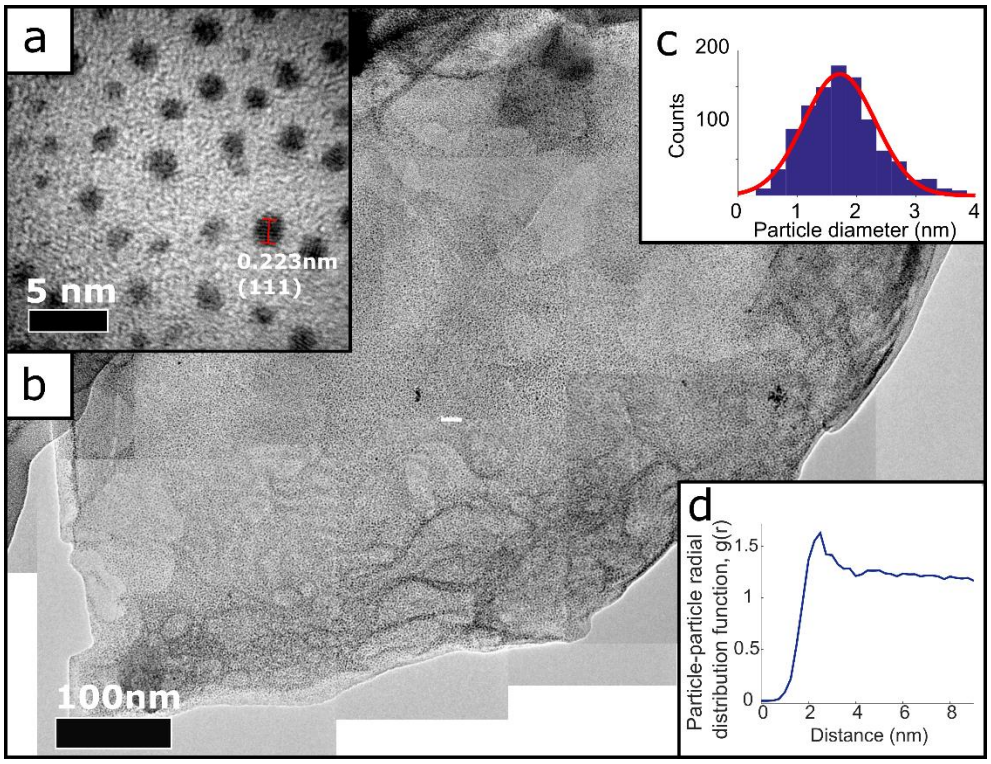

Figure 4-5 *(a) Single transmission electron micrograph of the same sheet exhibited in Figure 4-5(b) showing the (111) distance of a platinum nanoparticle. Figure 4-5(b) Composite transmission electron micrograph of a graphene sheet decorated with Pt nanoparticles. 4-5(c) A histogram of 100 nanoparticle diameters measured manually from Figure 4-5(a), fit with a Gaussian. Figure 4-5(d) Radial distribution function, g(r), calculated using centres of particles detected using image processing software (methods).*

The resultant material consists of ~micron-sized layered structure covered uniformly with a high density of nanometre-sized objects. Figure 4-5(a) shows a close-up image of the GD-Pt/G sheet. Analysis of the lattice planes, shown in Figure 4-6, confirms the nanoparticles to be metallic Pt as expected, with the (111) planes of the Pt nanoparticles marked on the micrograph. This suggests that the Pt nanoparticles are formed by the on-sheet reduction of $PtCl_2$ by the delocalised charge present on the graphene sheets.

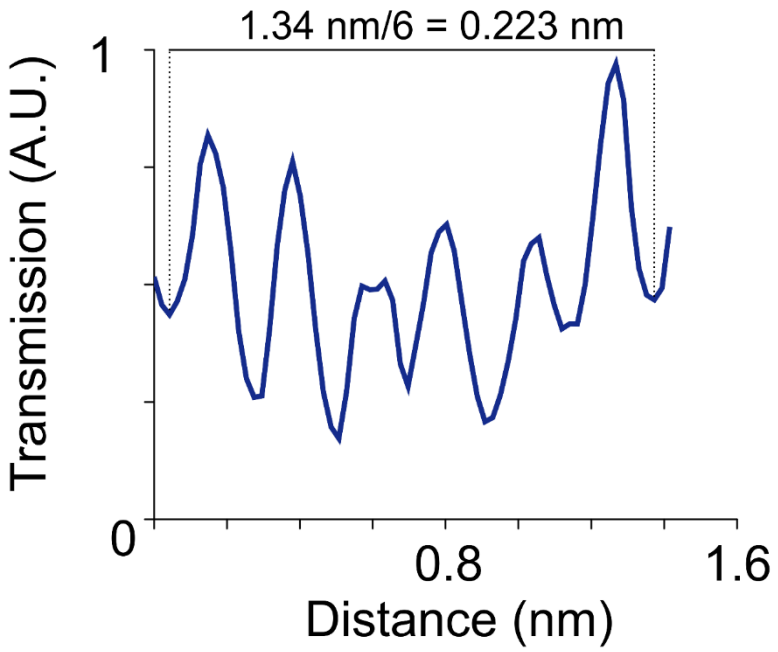

Figure 4-6 *Line profile of platinum nanoparticle planes, visible in Figure 4-2a. The distance measured across seven planes was found to be ca. 1.34 nm, resulting in an interplanar distance of 0.223 nm. This corresponds with the (111) Pt interplanar spacing.*

By manually measuring 1034 nanoparticles in Figure 4-5(a), the particle diameter distribution displayed in Figure 4-5(c) has been obtained. The histogram is well-fitted by a Gaussian function from which the mean diameter of the Pt was calculated to be (1.7 ± 0.6) nm. By stitching together many nanometre-resolution micrographs, it was possible to produce a composite TEM micrograph, allowing for the high resolution required to distinguish individual nanoparticles to be realised across a much larger area (ca. 1 μm^2). Figure 4-5(b) demonstrates the homogeneity of the distribution of the nanoparticles on the graphene surface, with very few examples of agglomerate particles.

The distribution of the nanoparticles was investigated by calculating the Pt-Pt site-centre, site-centre radial distribution function, g(r), of the Pt nanoparticles (Figure 4-5(d)). The g(r) demonstrates that the Pt particles are well ordered with respect to one another. The distribution has a clear peak at 2.5 nm, corresponding to the average inter-particle nearest neighbour distance, and a smaller second peak at 4.75 nm. As well as the size of the particles, the edge-to-edge distance between nanoparticles makes a significant difference in catalytic activity, with a significant increase in

specific activity as the separation decreases below 1 nm.[132] With an average edge-to-edge distance of 0.8 nm, this proximity effect may contribute to GD-Pt/G's strong electrocatalytic performance (as discussed in Chapter 5).

4.2.3 X-ray Photoelectron Spectroscopy

X-ray photoelectron spectroscopy was used to determine the percentage of platinum in GD-Pt/G. A high-resolution Pt XPS spectrum and broader survey spectrum obtained from GD-Pt/G are shown in the Figure 4-7.

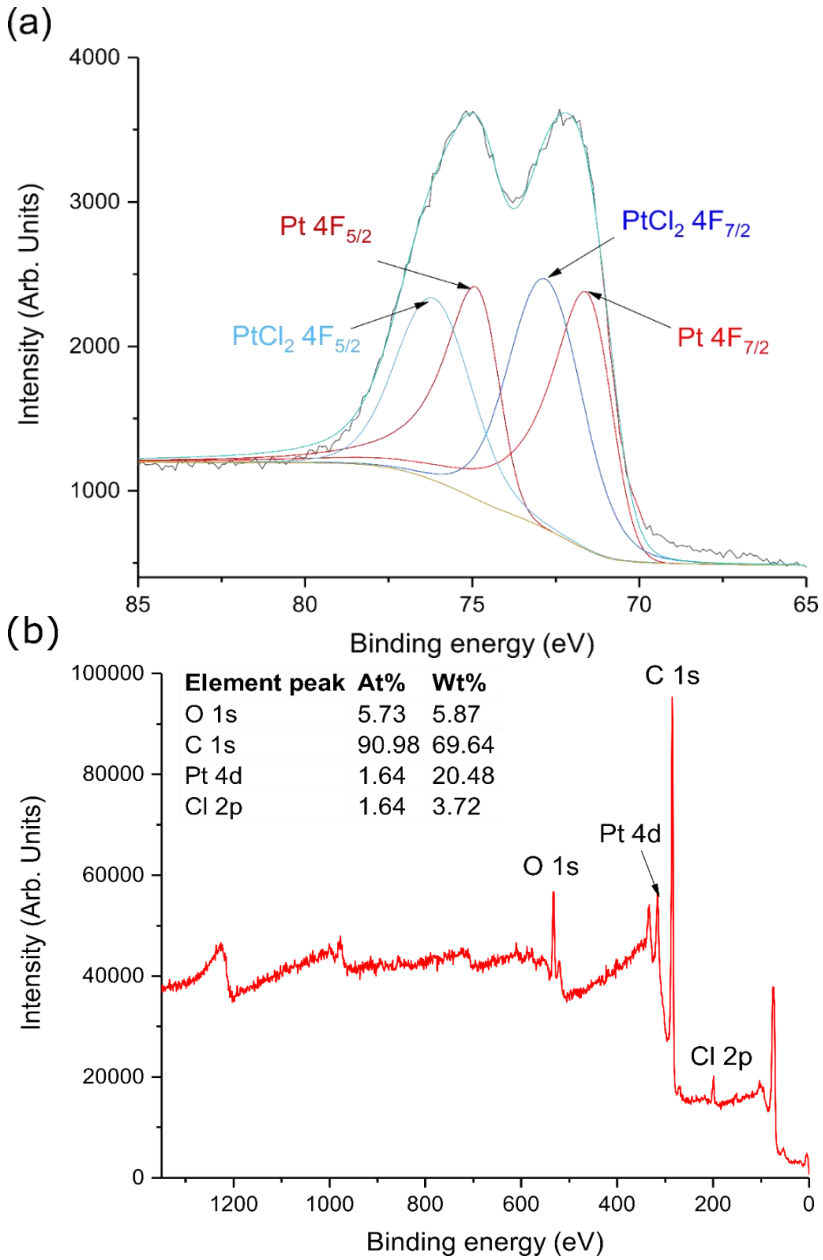

Figure 4-7 *(a) XPS high resolution scan of the Pt 4F region of GD-Pt/G powder. (b) XPS Survey spectrum of GD-Pt/G powder with elemental quantification table inset*

Figure 4-7(a) shows a high-resolution scan of the Pt 4f region of a sample of GD-Pt/G powder. The peaks can be deconvoluted into a combination of platinum and platinum chloride peaks. The platinum $4f_{7/2}$ peak lies at 71.0 eV, with a well-separated spin-orbit component, $4f_{5/2}$, at 74.45 eV. $PtCl_2$ has peaks at 72.4 eV and 75.75 eV ($4f_{7/2}$ and $4f_{5/2}$ respectively). Figure 4-4(b) is a broader survey scan of the sample, with the O 1s, C 1s, Pt 4d and Cl 2p peaks labelled, and a quantification table inset.

Using the areas under each of the fitted curves, quantification of these peaks suggests a 50:50 mixture of platinum and unreacted platinum chloride. In the survey measurement, the chlorine atomic percentage can be halved to calculate the amount of platinum present as $PtCl_2$ in the sample, as there are twice as many chlorine atoms as platinum in $PtCl_2$. As the At% can be seen to be 1.64 for both platinum and chlorine, the 50:50 ratio of Pt:$PtCl_2$ obtained from the analysis of the high-resolution spectra consistent with the At% obtained from the quantification of the survey XPS spectrum. Quantification of the spectrum, used in combination with the high-resolution Pt 4F scan, suggests that GD-Pt/G has a Pt loading weight of 11.5 wt%. XPS is a surface technique, and as such XPS measurements are only representative of the surface of a given sample. However, the Pt loading weight determined by XPS was used to quantify electrochemical activity measured using rotating disk electrochemistry, which makes use of a thin film (*i.e.*, it is also a surface technique). Therefore, XPS measurements suitably reflect the amount of platinum available for catalysis in an RDE experiment.

4.3 Conclusion

A material comprised of platinum nanoparticles supported by graphene was synthesised via the reaction of platinum chloride salt with a graphenide solution.

XRD and Raman spectroscopy have been used to characterise the graphite intercalation compounds synthesised using the metal-ammonia method, as compared to the initial starting graphite. XRD analysis showed that the graphite had been intercalated with potassium and ammonia. This was further verified by the obtained Raman spectra: the overall shift in the G peak position measured using Raman mapping suggests that graphite had successfully been intercalated with potassium and therefore that $KC_{24}(NH_3)_{1.3}$ had been obtained. Following the reaction with platinum chloride, the resultant GD-Pt/G material was also characterised using Raman spectroscopy. The G peak was observed to return to its original position, matching the starting graphite, and a small D peak was measured, indicating that the material was no longer doped with potassium and that the synthesis process had introduced only a low number of defects. The shift of the D peak, along with its symmetrical nature, was evidence for the restacking of graphene sheets in the GD-Pt/G material.

Transmission electron microscopy was used to further investigate the nature of the GD-Pt/G material. It was found that the average nanoparticle size was (1.7 ± 0.6) nm, and the average nearest neighbour distance was 2.5 nm. The average distance between the nanoparticles was calculated to be 0.8 nm. The nanoparticles are ideally sized and spaced for ORR catalysis.

The mass percentage of metallic platinum present in the material was measured using X-ray photoelectron spectroscopy. High-resolution spectra of the platinum 4F region showed that ca. half of the platinum present in the sample was metallic, and half was excess platinum chloride. The overall weight percentage was then determined from a survey spectrum of the material, and found to be 11.5 wt_{pt}%.

Chapter 5: Electrochemical testing of GD-Pt/G

This Chapter describes the benchmarking of the catalytic activity of graphenide-derived platinum on graphene using rotating disk electrochemistry. Accelerated stress tests and identical location TEM are used to assess the durability of the catalyst.

5.1 Catalytic Activity of Platinum Graphenide-derived catalysts

Rotating disk and rotating ring-disk electrode experiments were carried out to investigate the ORR catalytic performance of the various catalysts synthesised in Chapter 4.

5.1.1 Cyclic Voltammetry

Cyclic voltammograms of GD-Pt/G compared with $PtCl_2$ and commercial Pt/C control samples are presented below. CVs were carried out between 0.025 and 1.2 V_{RHE}, at a scan rate of 20 mV s^{-1} in N_2 saturated 0.1 M $HClO_4$.

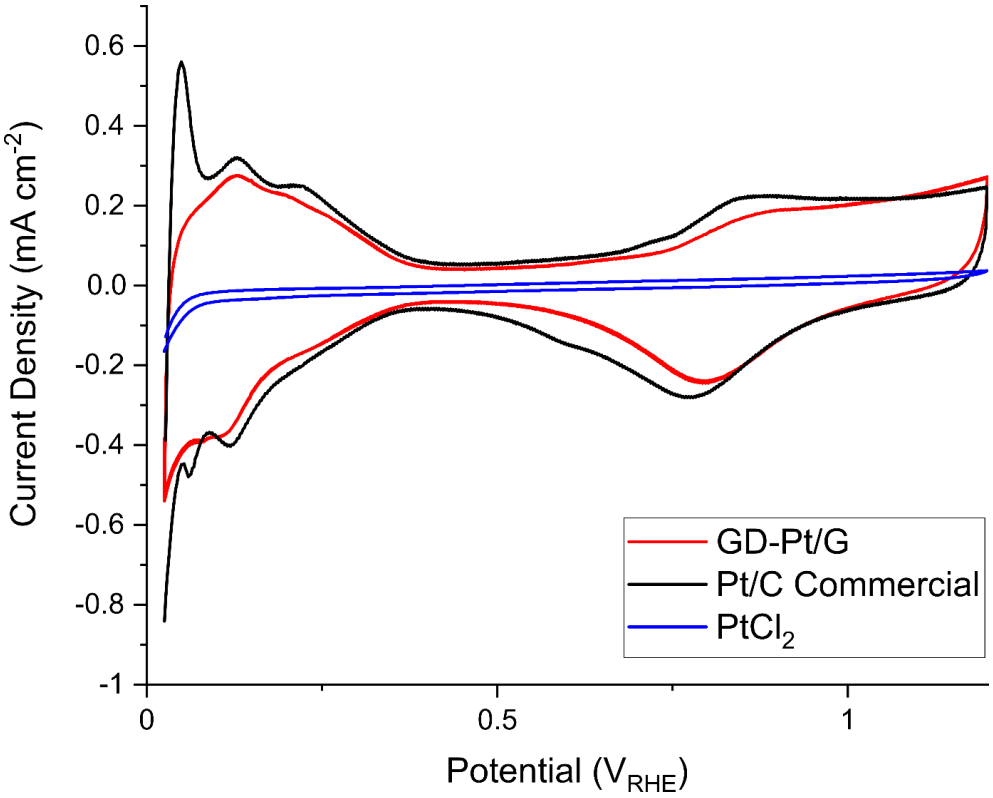

Figure 5-1 *Cyclic voltammograms of GD-Pt/G and commercial Pt/C electrodes, in N_2 saturated 0.1 M $HClO_4$, scan rate 20 mV s^{-1}.*

ECSAs for GD-Pt/G and Pt/C commercial were calculated using the Equation 3.8 and are shown in the Table 5-1.

Table 5-1. *Summary of the electrochemical surface area of GD-Pt/G compared with a commercial Pt/C catalyst.*

Material	***ECSA (m^2 g_{pt}^{-1})***
GD-Pt/G	**94.0**
Pt/C	**54.8**

The ECSA of GD-Pt/G was found to be 94.40 m^2 g_{pt}^{-1}, which compares favourably with the ECSA of Pt/carbon, 58.21 m^2 g_{pt}^{-1}. The high ECSA can be attributed to the fine distribution of platinum nanoparticles in GD-Pt/G. The $PtCl_2$ control sample, with an ECSA of 0.29 m^2 g_{pt}^{-1}, shows that any contribution to excess $PtCl_2$ to catalytic activity, when compared to GD-Pt/G, is negligible. Furthermore, there are no features of platinum in the $PtCl_2$ CV, only double layer capacitance.

5.1.2 Linear Sweep Voltammetry

Figure 5-2 presents the linear sweep voltammograms and associated Tafel plots obtained for GD-Pt/G and commercial Pt/C electrodes, measured at a rotation rate of 1600 RPM in 0.1 M $HClO_4$, with a scan rate of 20 mV s^{-1} in accordance with DOE protocols.

In Figure 5-2(a) it can be seen that the GD-Pt/G electrode closely matches the onset and half-wave potentials and limiting current of the highly optimised commercial Pt/C electrode. Specific and mass activities were calculated from the kinetic current, obtained from the current measured at 0.9 $V_{RHE,}$ as decribed by Garsany *et al.*[108] Although specific activities were found to be similar (465 and 413 μA cm_{Pt}^{-2} for GD-Pt/G and Pt/C respectively), the mass activity of GD-Pt/G was approximately twice as large of the commercial sample, as shown in Table 5-2. The observed increased mass activity suggests that the graphene support improves the utilisation of the available platinum nanoparticles, likely due to its facilitation of the formation of well-dispersed,

smaller Pt nanoparticles compared with Pt/C (typical nanoparticle size 5 nm[13]), and its high electrical conductivity.[90,133,134]

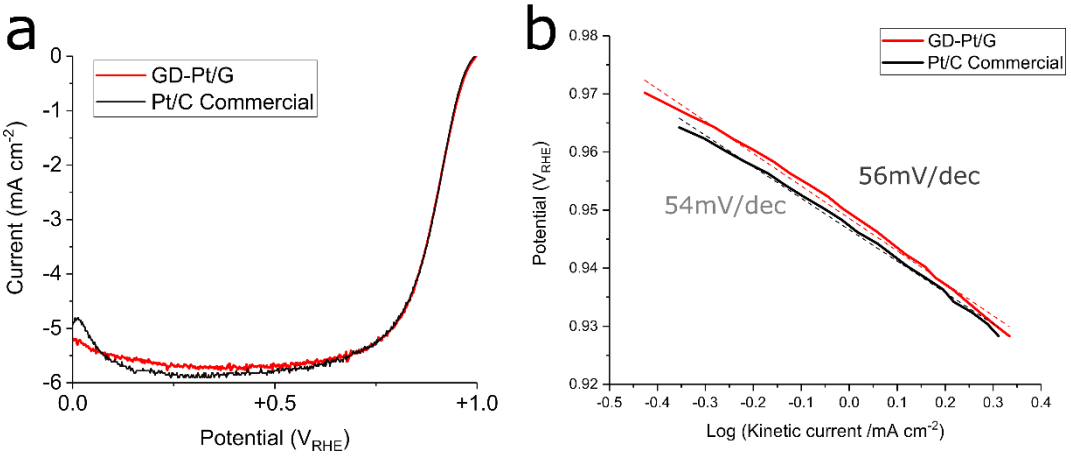

Figure 5-2(a) *Linear sweep voltammograms for ORR in O_2 saturted 0.1 M $HClO_4$, comparing the activity of GD-Pt/G with a commercial Pt/C catalyst, rotation rate 1600 RPM, scan rate 20 mV s^{-1}. (b) Tafel plots derived from 3(a) for ORR on GD-Pt/G and Pt/C electrodes*

The Tafel plots displayed in Figure 5-2(b) were obtained from Figure 5-2(a) by calculating mass-transport corrected kinetic current densities and plotting these against potential. The associated Tafel slopes were estimated to be 56 mV dec^{-1} for GD-Pt/G, and 54 mV dec^{-1} for commercial Pt/C. These values suggest that for both catalysts, the ORR proceeds via the preferred 4-electron pathway, for which the coverage of the adsorbed oxygen intermediates is the rate-limiting factor.[20,115,118]

Material	**Mass Activity ($A\ mg_{pt}^{-1}$)**	**Specific Activity ($\mu A\ cm_{Pt}^{-2}$)**
GD-Pt/G	**0.44**	**465**
Pt/C	**0.24**	**413**

Table 5-2. Summary of specific activity and mass activity of GD-Pt/G compared with a commercial Pt/C catalyst.

Rotating ring-disk experiments were used to further investigate the ORR mechanism catalysed by GD-Pt/G. Linear sweep voltammetry between 0.1 to 1 V_{RHE} was conducted on the disk of the electrode while the ring of the electrode was held at a voltage of 1.2 V_{RHE}, as explained in Chapter 3. Figure

5-3, below, shows the measured disk and ring current densities as the disk potential was swept from at a rate of 20 mV s^{-1} in O_2 saturated 0.1 M $HClO_4$.

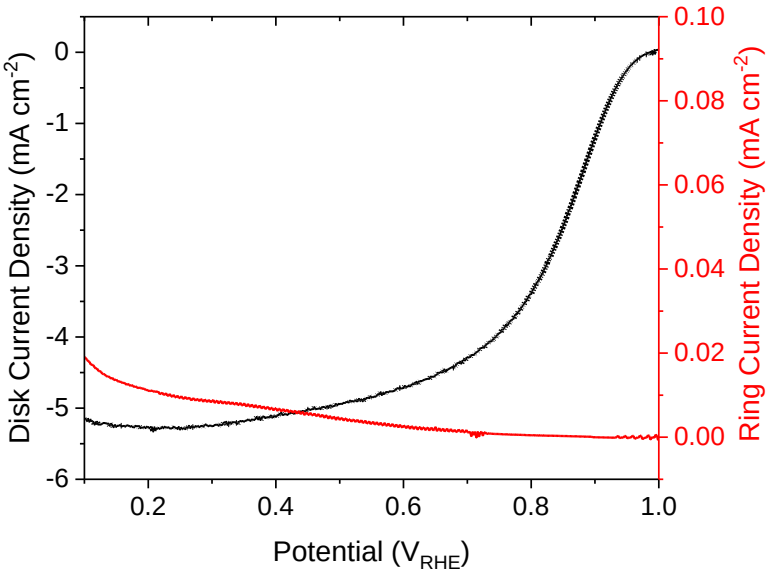

Figure 5-3 *Linear sweep voltammogram obtained using a rotating ring-disk experiment for GD-Pt/G. This was performed in 0.1 M $HClO_4$ at a scan rate of 20 mV s^{-1}.*

By using the ratios of disk and ring current density measured, the number of electrons transferred and the percentage of H_2O_2 produced were calculated as functions of applied potential (see Chapter 3.5.4). These are shown in Figure 5-4.

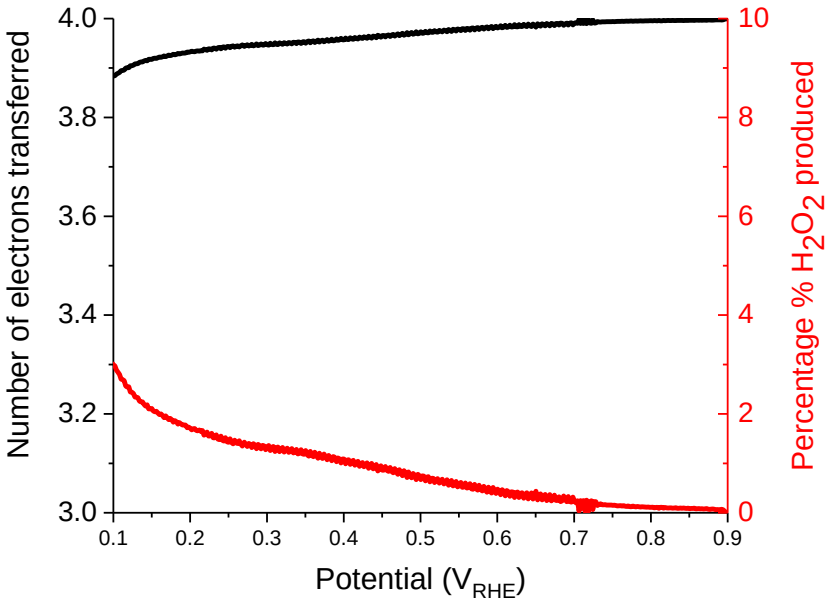

Figure 5-4 *Number of electrons transferred and H_2O_2 yield calculated from Figure 5-3*

It can be observed Figure 5-4 that the number of electrons transferred was found to be above 3.9 across the entirety of the potential range, and the percentage of H_2O_2 produced remained below 3%, which is further evidence to suggest that the ORR is proceeding via the "4 electron" pathway. A small increase in H_2O_2% is observed at low potentials (<0.2 V_{RHE}), which is in part due to an increase in disk current as a result of hydrogen evolution reaction, and as such does not fully represent the H_2O_2% produced as a result of ORR at these potentials.

5.1.3 **Accelerated Stress Tests**

To assess the durability of the GD-Pt/G catalyst, accelerated stress tests were carried out for 30,000 cycles between both 0.6-1 V_{RHE} and 1-1.6 V_{RHE} based on DoE accelerated stress tests (see Chapter 3).

The cyclic voltammograms, the ORR polarisation curves and the associated relative change in the normalised electrochemical surface areas (ECSAs), are shown in Figure 5-5. Figure 5-5(a) and Figure 5-5(d) show the cyclic voltammograms measured for GD-Pt/G at 10,000 cycle intervals, from which the hydrogen adsorption peaks (0.075-0.4 V_{RHE}) were used to calculate the ECSAs.

The ECSA values were then normalised to the initial ECSA and plotted against the number of accelerated stress test cycles, presented in Figure 4(b) and Figure 4(e). From these figures, it can be seen that, across the 30,000 cycles, the ECSA of commercial Pt/C sample degraded by as much as 30 % and 50 % during the 0.6-1 V_{RHE} and 1-1.6 V_{RHE} tests respectively.

Meanwhile, GD-Pt/G maintained its activity remarkably well, showing a comparatively small ECSA loss of 21% and 19% for the same number of cycles. The stability is further reflected in the ORR polarisation curves shown in Figure 4(c) and Figure 4(f), which show a negligible change in the onset potentials, and very little change in half-wave potentials and limiting currents after 30,000 cycles (Table 5-3). The changes in half-wave potentials and limiting currents measured after 30,000 cycles for commercial Pt/C are shown in Table 5-4.

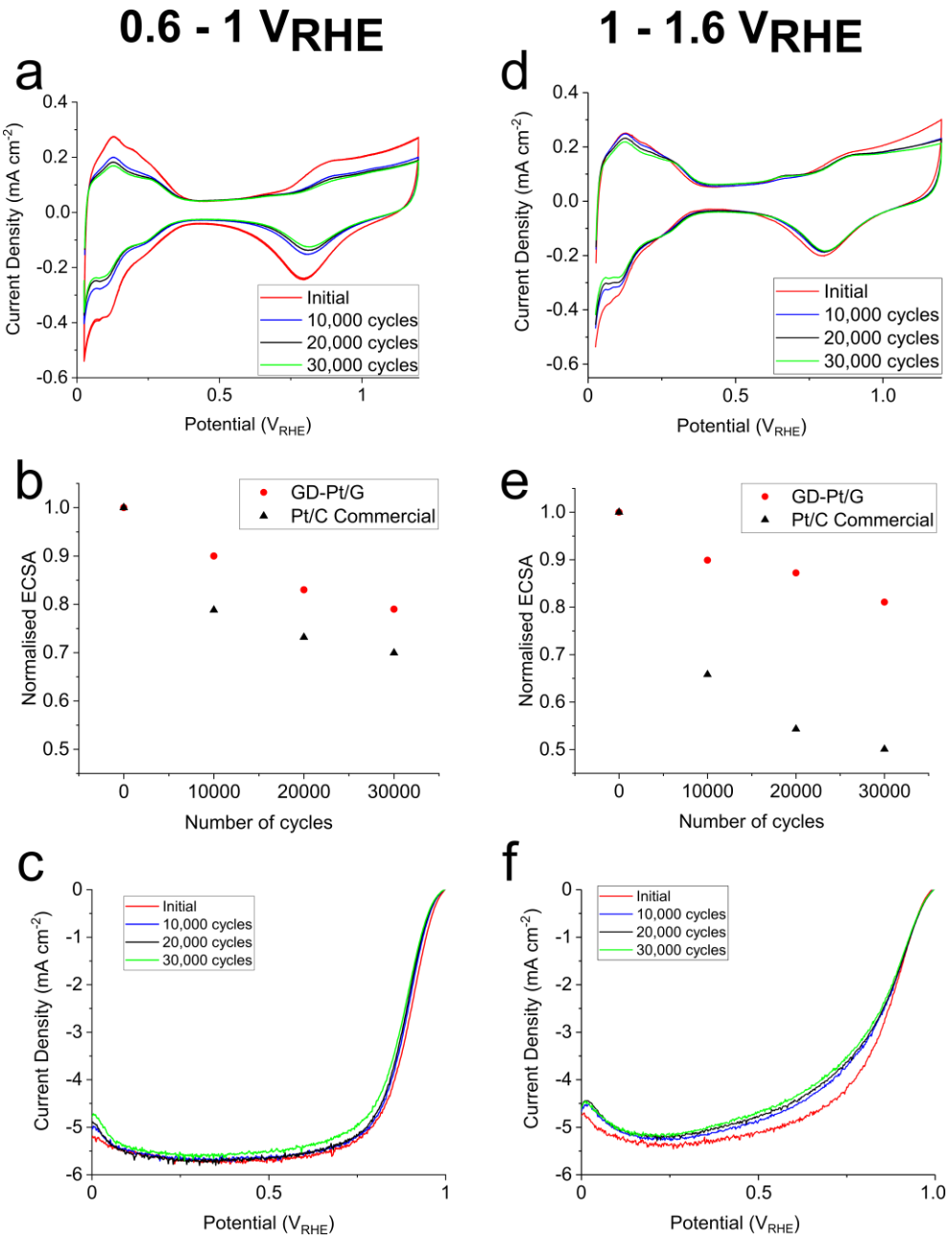

Figure 5-5 *(a) Cyclic voltammograms for GD-Pt/G measured across the 0.6-1 V_{RHE} accelerated stress test, with associated normalised change in electrochemical surface area, compared with Pt/C, and polarisation curves shown in (b) and (c) respectively. (d) Cyclic voltammograms for GD-Pt/G measured across the 1-1.6 V_{RHE} accelerated stress test, with associated normalised change in electrochemical surface area, compared with Pt/C, and polarisation curves shown in (e) and (f) respectively.*

Number of cycles	Limiting current density (mA cm^{-2})	Change in limiting current (mA cm^{-2})	Half wave potential (mV_{RHE})	Half wave potential shift (mV)
0.6 – 1 V_{RHE}				
0	5.71	0	894	0
30,000	5.58	-0.13	876	-18
1 - 1.6 V_{RHE}				
0	5.23	0	865	0
30,000	4.92	-0.31	850	-15

Table 5-3. Limiting current density, half wave potential and relative changes after 30,000 cycles for GD-Pt/G.

Number of cycles	Limiting current density (mA cm^{-2})	Change in limiting current (mA cm^{-2})	Half wave potential (mV_{RHE})	Half wave potential shift (mV)
0.6 – 1 V_{RHE}				
0	5.84	0	836	0
30,000	5.7	-0.14	874	38
1 - 1.6 V_{RHE}				
0	5.23	0	865	0
30,000	4.92	-0.31	850	-15

Table 5-4. Limiting current density, half wave potential and relative changes after 30,000 cycles for commercial Pt/C.

These results show that the GD-Pt/G material displays excellent durability when compared to any platinum graphene-based ORR catalyst reported in the literature as summarised in Table A1.

Upon cycling, the decrease in catalytic activity in typical Pt/C catalysts is due to the corrosion of the carbon and the change in the distribution of the platinum within the system. Suggested mechanisms for these changes are: size increase of platinum nanoparticles via 3D Ostwald ripening, migration / agglomeration of platinum nanoparticles, platinum dissolution into the electrolyte and the detachment of platinum nanoparticles from the carbon support due to carbon corrosion, as detailed in Chapter 3.[13,32,135]

5.1.4 Identical Location Transmission Electron Microscopy

The effects of these mechanisms can be observed using identical location TEM (ILTEM), which offers the unique ability to image the same area of material before and after cycling, where the TEM grid is directly used as the working electrode.[13] To further investigate the durability of GD-Pt/G, ILTEM was performed to give a qualitative assessment of which corrosion mechanisms were responsible for activity loss. Gold ILTEM grids were prepared via drop-casting GD-Pt/G ink and examined before and after 30,000 0.6-1 V_{RHE} potential cycles. Figure 5-6 shows composite TEM micrograph stitches of the same area of a sample of overlapping sheets of GD-Pt/G at various length scales, before and after the accelerated stress test.

Figures 5-6(a) and 5-6(d) present ca. 1 μm length of material. At this resolution, it can be seen that the GD-Pt/G remains almost completely unchanged, showing clear resistance to the typical corrosion mechanisms seen in commercial Pt/C catalysts.[13] The structure of the nanoparticle distribution appears to be unaffected by the cycling: in order to find any differences it is necessary to evaluate the sample at much higher resolutions. The areas highlighted by red rectangles in Figs. 5-6(a) and (d), are shown at a higher resolution in Figs. 5-6(b) and (e) respectively. The sections in blue are then shown at an even higher resolution in Figs. 5-6(c) and (f), where the composites are built from atomic resolution micrographs. At this resolution, it is possible to observe small changes in the distribution of the nanoparticles. In Figures 5-6(c) and 5-6(f), examples of platinum nanoparticle

agglomeration have been highlighted in red. As these particles can be seen to have moved small distances to agglomerate, it appears that this has occurred via the migration mechanism rather than via Ostwald ripening. Importantly, there are no distinguishable cases of nanoparticle detachment. The blue area along the edge of the graphene sheet shown in Figure 5-6(f) highlights the presence of the Nafion added as part of the accelerated stress test.

The changes in platinum nanoparticle distribution and graphene sheets shown in Figure 5-6 are much less significant than what is typically observed with commercial Pt/C catalysts[13], where extensive nanoparticle agglomeration and loss of up to half of the nanoparticles can be observed in as few as 4 hours of cycling.[136] This is consistent with the small relative decrease in the activity of the GD-Pt/G catalyst. In the majority of methods, nanoparticles are formed via the reduction of a platinum precursor by a secondary reducing agent and interact with the supporting material via van der Waals force. Previous studies[88,90] have suggested that the distribution of nanoparticles is due to the limited supply of charge available to reduce the platinum precursor. By making use of the metal-ammonia method to intercalate graphite, it has been possible to obtain a stage 1 GIC ($KC_{24}(NH_3)_{1.3}$) in which the graphene sheets have lower charge density than for the typical stage 1 compound KC_8.[88,90] The lower charge ratio may explain the production of smaller nanoparticles, well-suited for electrocatalysis.

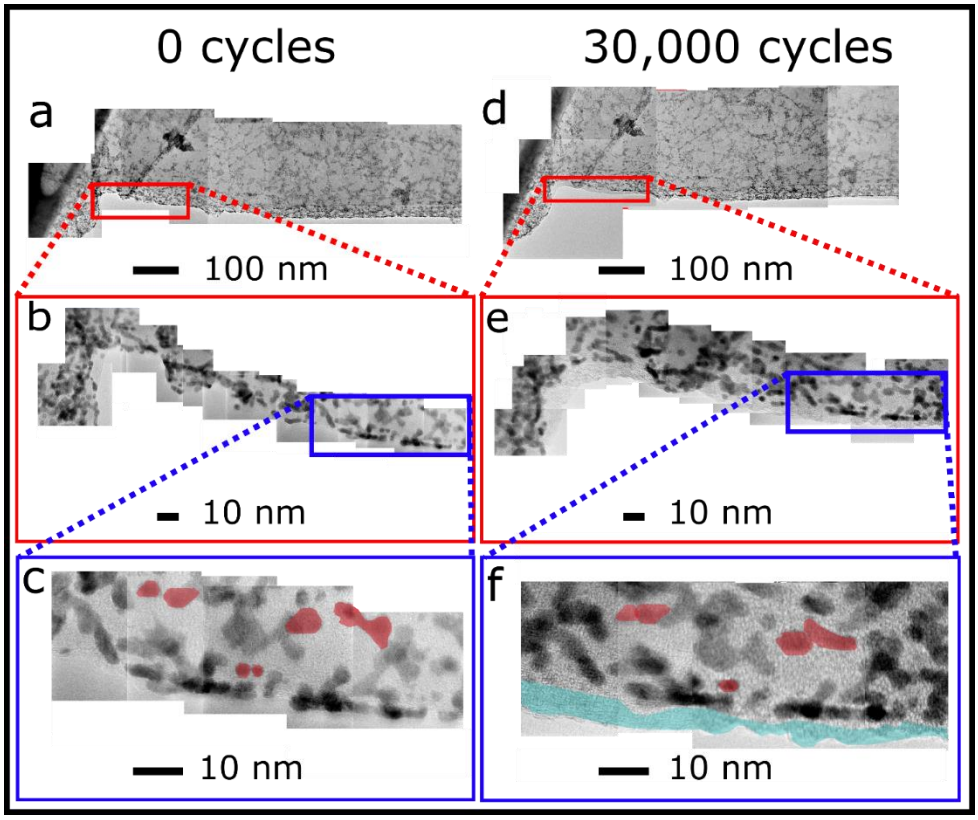

Figure 5-6 *Identical Location TEM images at varying length scales. (a) and (d) show a micron length stitch before and after corrosion, respectively. (b) and (e) correspond to the highlighted red boxes in (a) and (c), showing an area two hundred nanometres across, built-up of atomic resolution images. (c) and (f) correspond to the highlighted blue boxes in (b) and (e), where examples of nanoparticle migration and agglomeration are highlighted in red and the added Nafion layer shown blue.*

5.2 Conclusion

The novel GD-Pt/G material was tested for its catalytic activity toward the oxygen reduction reaction using rotating disk electrochemical techniques. The electrochemical surface areas of GD-Pt/G, $PtCl_2$ and a commercial Pt/C catalyst were measured using cyclic voltammetry. It was found that PtCl2 showed a negligible ECSA compared with GD-Pt/G and Pt/C, and so it concluded that excess $PtCl_2$ had a negligible impact on the catalytic activity of GD-Pt/G. The ECSA of GD-Pt/G 94.40 $m^2\ g_{pt}^{-1}$, was greater than that of the ECSA of Pt/C, 58.21 $m^2\ g_{pt}^{-1}$, with the improvement attributed to the size and distribution of the platinum nanoparticles in GD-Pt/G.

ORR activity was directly measured using linear sweep voltammetry. Linear sweep voltammograms for GD-Pt/G and Pt/C overlapped closely, with very similar limiting currents, onset potentials and half-wave potentials. In the case of GD-Pt/G, this was achieved by a lower loading of platinum on the electrode, resulting in a higher mass activity than that of Pt/C (0.44 A mg_{pt}^{-1} vs 0.24 A mg_{pt}^{-1} respectively). Tafel analysis and RRDE measurements confirmed that the ORR was occurring via the preferred 4-electron pathway.

Following the benchmarking of GD-Pt/G's catalytic activity, accelerated stress tests were carried out following adapted DOE protocols to assess the material's durability. In the "platinum corrosion" test, conducted between 0.6 and $1V_{RHE}$, the ECSA of GD-Pt/G decreased by 21% (Pt/C: 30%) and in the "carbon corrosion test", 1-1.6 VRHE the ECSA decreased by 19% (Pt/C: 50%). The improved durability of GD-Pt/G was attributed to the graphitic, largely defect-free nature of the restacked-graphene support which impedes carbon corrosion mechanisms, and the direct reduction of the platinum salt by the graphene sheets themselves, which may lead to stronger bonding between the nanoparticles and the support material. The stability of the nanoparticles was further evidenced using identical location TEM, where a sample was imaged before and after 30,000 platinum corrosion cycles and only small changes in nanoparticle size and distribution were observed.

Chapter 6: Scale up of GD-Pt/G

Having used rotating disk electrochemistry to show that GD-Pt/G is active for the oxygen reduction reaction and more durable than a commercial catalyst, the next step was to scale up the synthesis of the material so that enough could be produced for testing in a fuel cell membrane electrode assembly.

This chapter first details the changes made to the synthesis process to solve a number of difficulties with the original method. The description of the developed method is then followed by characterisation and electrochemical testing of the resultant material (GD-Pt/G-2). Finally, initial MEA tests are presented.

6.1 Synthesis of GD-Pt/G-2

To produce enough GD-Pt/G for MEA testing, for the sake of scalability it was desirable to modify the original synthesis method (Chapter 3). The material produced via the modified synthesis method is referred to within this chapter as GD-Pt/G-2.

Although sonication was used in the method detailed in Chapter 3, adapting work by Milner *et al*., it was preferable to remove this energy-intensive step. In the original method, after sonicating, only the supernatant of the solution was used to ensure only fully exfoliated graphene was used. However, this meant that the overall concentration of the reacted solutions was low (*ca.* 0.3 mg ml^{-1}). As a result, obtaining the amounts of powder needed for MEA testing would require many litres of solvent, which was neither practical nor cost-efficient. Therefore, it was decided that the use of stirring (instead of sonicating) and the entire solution (instead of just the supernatant) should be investigated as a method for producing graphene in quantities large enough for scale up. All of the graphite intercalation compound in the solution, not just that which had been exfoliated was charged, and as such it was theorised that all of it should take part in the reaction with a platinum salt.

A further difficulty to address was that $PtCl_2$ did not dissolve in THF and so had to be ultrasonicated to obtain a dispersion. This introduced an additional energy-intensive step and made any excess $PtCl_2$ difficult to remove from the synthesised material. As such, the platinum salt cis-dichlorobis(dimethyl sulfoxide)platinum(II) ($Pt(DMSO)_2Cl_2$) was chosen to replace $PtCl_2$ as it is soluble in THF.

The full, developed method was carried out as follows. Graphite intercalation compound $KC_{24}(NH_3)_{1.3}$ was synthesised as described in Chapter 3. Graphenide solutions were prepared by stirring THF and GIC together at a concentration of 5 mg ml^{-1}. A 5 mg ml^{-1} solution of $Pt(DMSO)_2Cl_2$ in THF was prepared by stirring. Both solutions were stirred for 24 hours and then reacted immediately by adding $Pt(DMSO)_2Cl_2$/THF directly to the bottle of graphenide solution stoichiometrically. After the reaction, the resultant solutions were removed from the glovebox and vacuum filtered and washed with THF and IPA to obtain GD-Pt/G-2 powder, which was left to dry at room temperature for at least 12 hours before use. Figure 6-2 shows a photograph of a batch of GD-Pt/G-2.

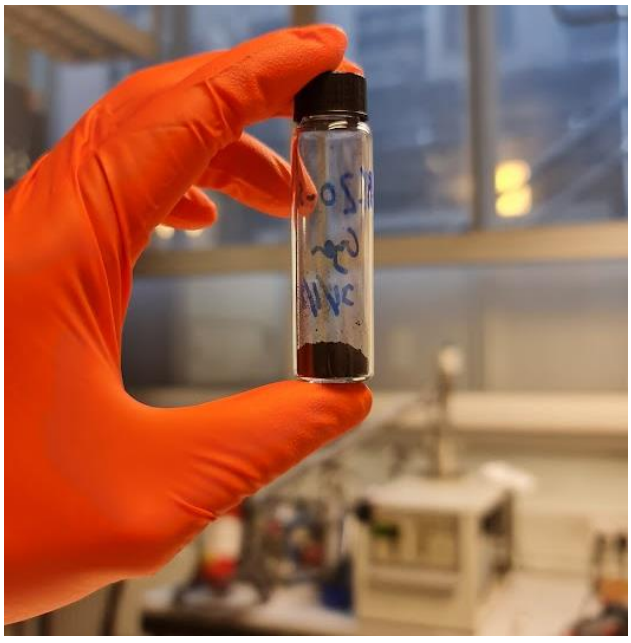

Figure 6-1 *ca. 60 mg of GD-Pt/G-2 powder*

6.2 Characterisation of GD-Pt/G-2

Having obtained a dry powder, Raman spectroscopy, transmission electron microscopy and thermogravimetric analysis were used to characterise the GD-Pt/G-2.

6.2.1 Raman Spectroscopy of GD-Pt/G-2

Representative Raman spectra of the starting graphite powder, GD-Pt/G and GD-Pt/G-2 are shown in Figure 6-2.

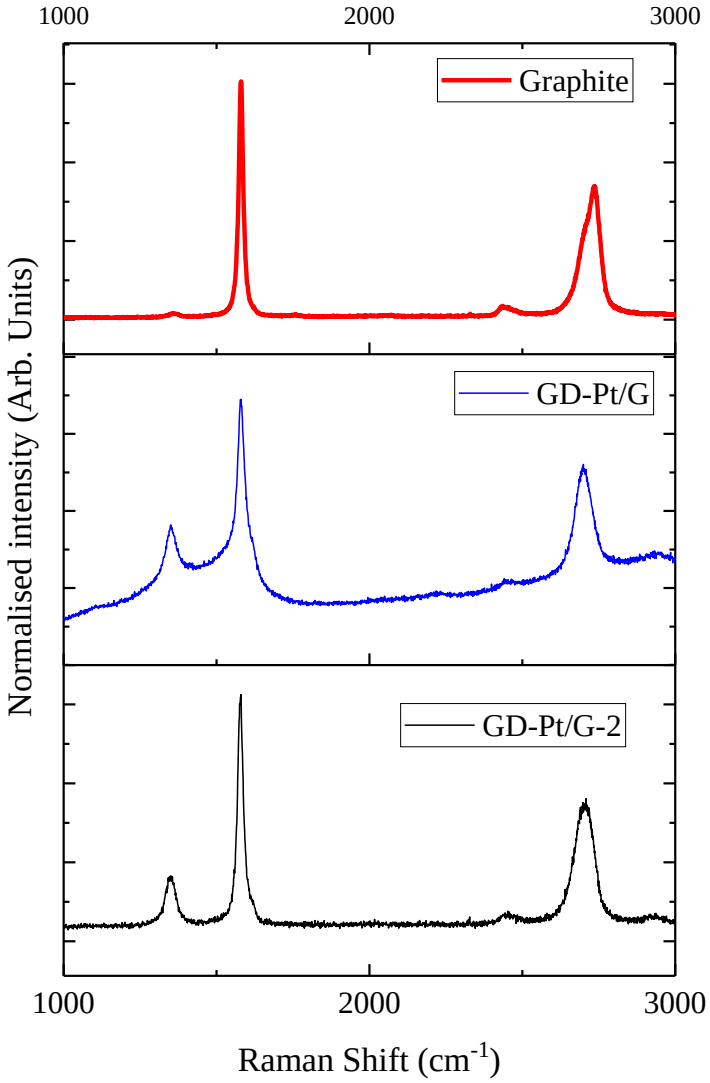

Figure 6-2 *representative Raman spectra of the initial bulk graphite, GD-Pt/G and GD-Pt/G-2*

It can be seen that the spectrum of GD-Pt/G-2 shares similar features to that of GD-Pt/G, as described in Section 4.1.1. There is a 2D peak comprised of a single Lorentzian peak at ca. 2700 cm^{-1}, a D peak at 1350 cm^{-1} that is greater in relative intensity than that of the D peak in the starting graphite, and a G peak at ca. 1580 cm^{-1} with a small shoulder at *ca.* 1605 cm^{-1}.

Using a spatial map scan, a larger area of the GD-Pt/G-2 powder sample was investigated and the I(D):I(G) and I(G):I(2D) ratios were calculated. The resultant maps of the ratios of the intensities can be seen in Figure 6-3 below; data points that are shaded in grey correspond with spatial points where no spectra were obtained.

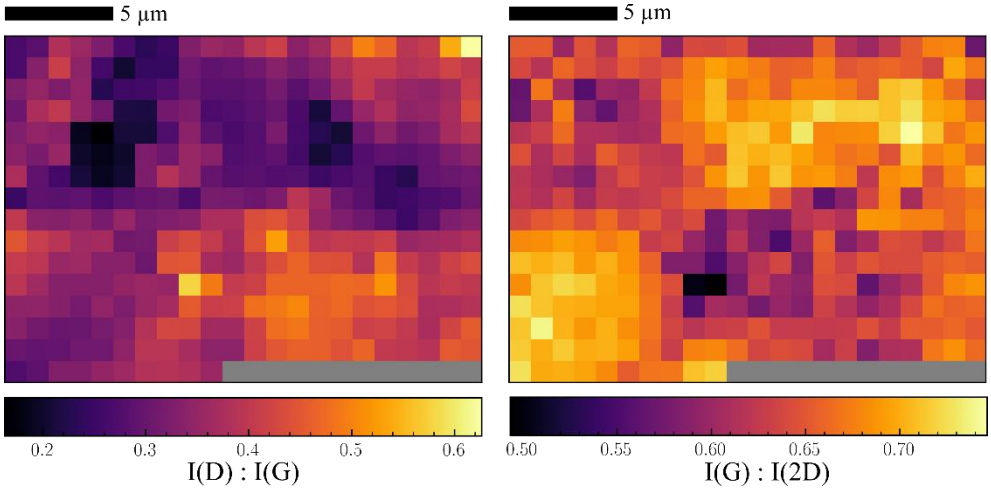

Figure 6-3 *Spatial maps showing the variation in I(D):I(G) and I(G):I(2D) ratios across a sample of GD-Pt/G-2*

The mean ratio values and their associated standard deviations are presented in Table 6-1.

	Mean	**Standard Deviation**
I(D):I(G)	**0.36**	**0.06**
I(G):I(2D)	**0.65**	**0.04**

Table 6-1. *Summary of I(D):I(G) and I(G):I(2D) ratios and associated standard deviation values of an area of GD-Pt/G-2.*

Following analogous reasoning as described in Section 4.2.1, the I(G):I(2D) ratio suggests that GD-Pt/G-2 is composed of restacked graphene layers.[93,95,126,127] The increase in the I(D):I(G) ratio is as a result of defects introduced through the synthesis process and the addition of platinum nanoparticles. [56,103]

6.2.2 Transmission Electron Microscopy of GD-Pt/G-2

A number of representative TEM micrographs and an accompanying STEM image and EDS map of GD-Pt/G-2 are shown below.

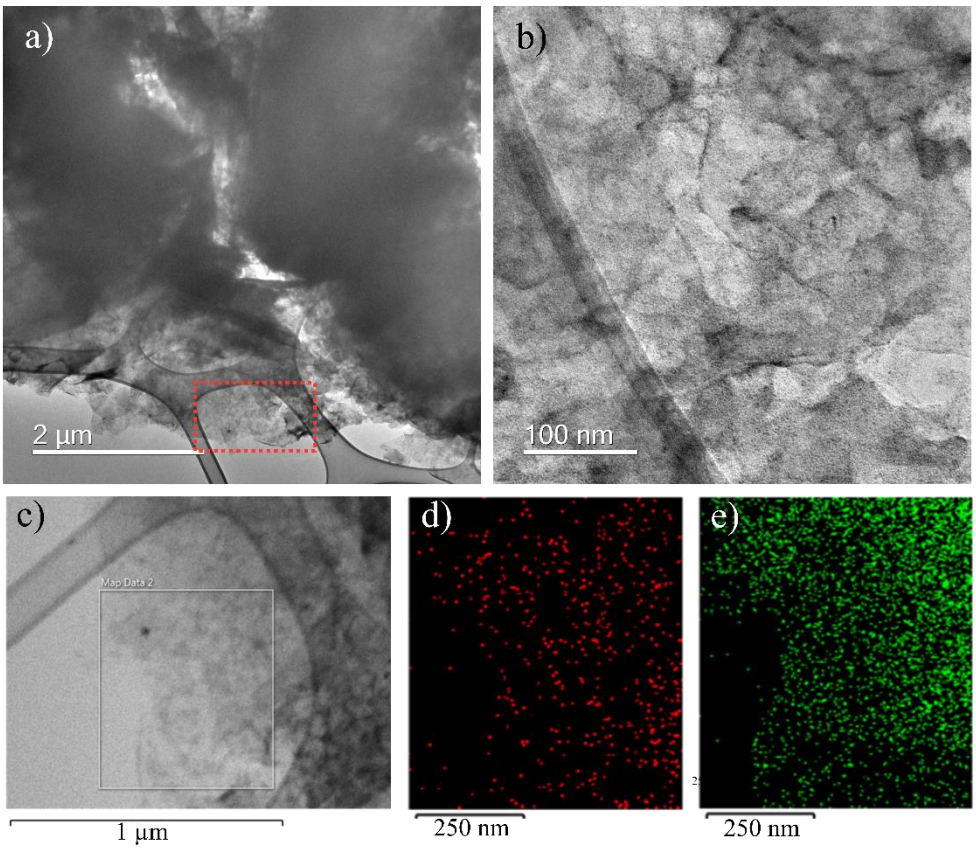

Figure 6-4 (a) and (b) *correspond to lower and higher magnification micrographs of the same area of a GD-Pt/G-2 sample, indicated by the rectangle, showing restacked graphene decorated with platinum nanoparticles. An EDS map was taken of the area indicated in the STEM micrograph (c), with corresponding distributions of platinum and carbon displayed in (d) and (e) respectively*

As can be observed in Figure 6-4(a), GD-Pt/G-2 is composed of turbostratically restacked graphene with the contrast of the image, and therefore the number of graphene layers, varies greatly across even small spatial areas. Considering the contrast qualitatively, it appears that GD-Pt/G-2 consists of a greater number of restacked layers than GD-Pt/G. Figure 6-4(b) is a higher magnification micrograph of the area indicated in red in (a). Black nanoparticles are seen to decorate the surface of the graphene sheet and were confirmed to be platinum through the use of EDS, the results of which are shown in Figure 6-4 (c-e). Figure 6-4 (c) is a STEM micrograph of the area indicated by the red box in 6-4(a) (rotated by 90 ° by the instrument) from which the EDS map measurement was taken. The elemental maps

displayed in Figures 6-4 (d) and (e) confirm that platinum was present across the entire area of graphene examined.

In order to obtain a particle size distribution, 277 platinum nanoparticles were manually measured from a higher magnification micrograph of Figure 6-5(b). The higher magnification micrograph is presented below alongside the obtained histogram of nanoparticle size.

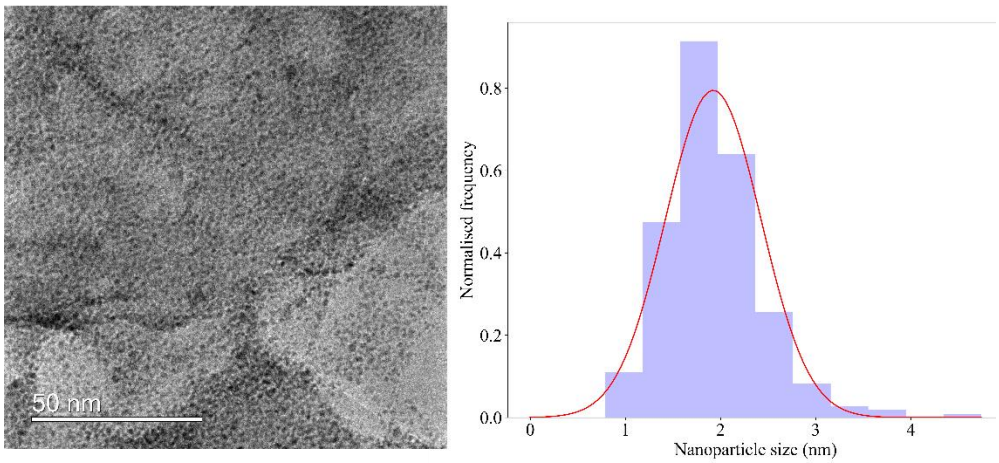

Figure 6-5 *A representative high magnification micrograph of GD-Pt/G-2 from which the diameters of the nanoparticles were measured and the presented histograph was obtained.*

The average measured particle size is (1.9 ± 0.5) nm, which is similar to the average particle size obtained for GD-Pt/G in Section 4.2.3. This particle size has been shown to be optimum for the catalysis of ORR, with larger nanoparticles bonding too weakly with oxygen, and smaller particles bonding too strongly, as described in Section 2.2.[30]

A significant difference between the two methods presented in Chapter 3 and this chapter is the use of $PtCl_2$, which does not dissolve in THF, and $Pt[DMSO]_2Cl_2$, which does. Despite the difference in platinum salts used, the similarity in nanoparticle size suggests that the reduction of $Pt[DMSO]_2Cl_2$ by the graphenide solution in the modified method produces a similar platinum nanoparticle-decorated, restacked-graphene material to that synthesised and tested in Chapter 4 and 5. The resultant material was therefore likely to be suitable for ORR catalysis, and its catalytic activity is presented in Section 6.3.

6.2.3 Thermogravimetric Analysis

Figure 6-6 presents the normalised masses of initial graphite material and synthesised GD-Pt/G-2 powder against temperature and time obtained from the same TGA experiment. The experiments were conducted under an air blanket, with an initial temperature ramp of 2 °C to 900 °C, followed by a thermostatic hold for 6 hours. The normalised mass was obtained by dividing the measured mass at each point by the initial mass.

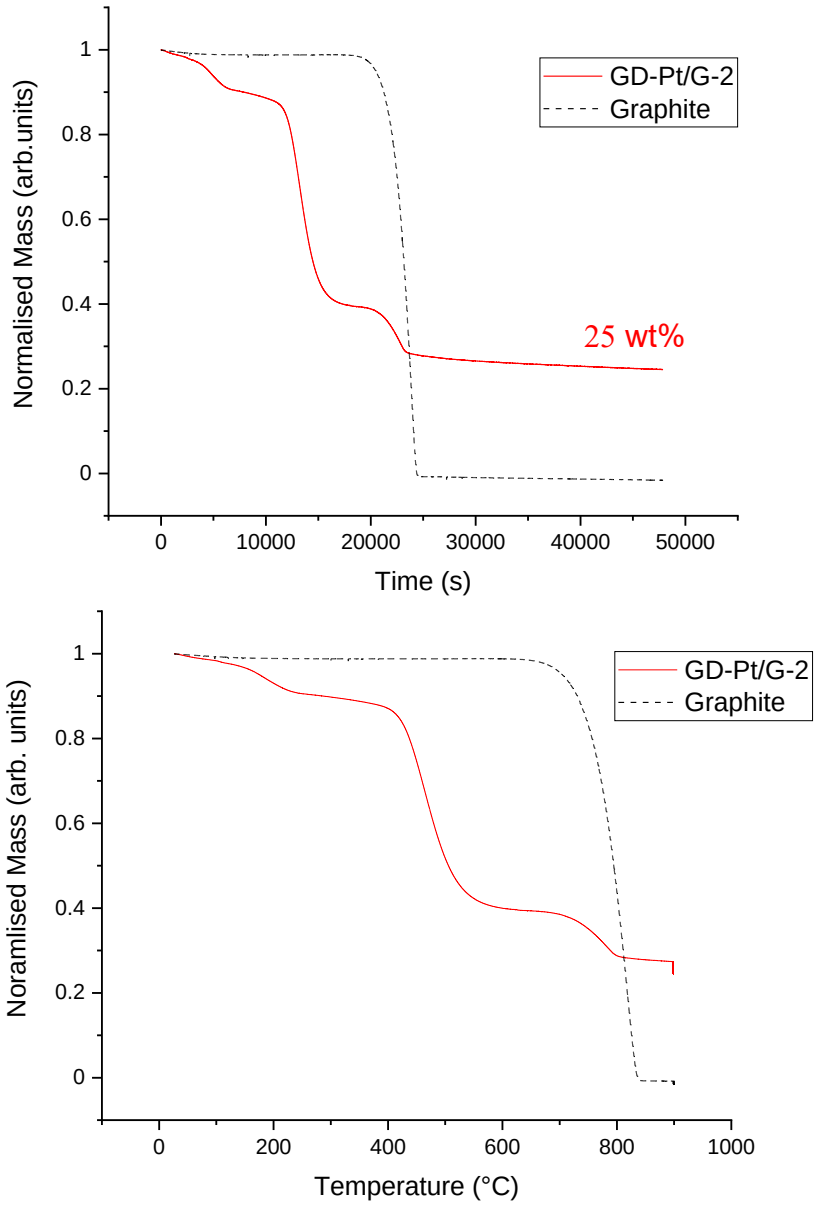

Figure 6-6 *Thermograviemtric analysis plots of GD-Pt/G-2 compared with graphite: normalised mass against time (top) and temperature (bottom).*

TGA was used to determine the platinum loading weight of GD-Pt/G-2. Although this was attempted with GD-Pt/G, the presence of excess platinum chloride meant that the residual platinum mass left at the end of the experiment was a mixture of platinum that had been reduced by the graphene to form nanoparticles, and platinum produced via the thermal decomposition of platinum chloride. In the modified synthesis method, the $Pt[DMSO]_2Cl_2$ readily dissolves in THF, and is not added in excess, and so it was assumed that after filtration and washing the only platinum mass left was from platinum nanoparticles.

The graphite powder mass shows a small initial decrease due to the evaporation of adsorbed water. This is followed by a large decrease once the temperature reaches 700 °C, where it combusts in air and the normalised mass decreases to zero.

In the GD-Pt/G-2 graphs, similar decreases in mass due to residual solvent and water evaporating can be initially observed before a significant decrease in mass at ca. 500 °C. This decrease is thought to be the restacked graphene decorated with platinum nanoparticles: the lower combustion temperature relative to graphite is a result of the catalytic property of the platinum nanoparticles, and the decrease in the lateral size of the flakes.[137] There is then a second significant decrease of ca. 10% at ca. 700 °C, which corresponds to the combustion of unreacted graphite remaining in the sample. The final relative mass is ca. 0.25, which therefore suggests a platinum loading of 25 wt_{pt}%.

6.3 Catalytic activity of GD-Pt/G-2

Before taking GD-Pt/G-2 to the fuel cell testing level, rotating disk electrochemistry was used to screen the material to ensure it was suitable for use in MEA fabrication. As such, detailed optimisation of the sample for RDE testing, such as the optimisation of water:IPA:Nafion ratios in the RDE catalyst ink *etc.* [108,138] are beyond the scope of this Chapter.

6.3.1 Cyclic and Linear Voltammetry

Figure 6-7 presents cyclic voltammograms obtained for GD-Pt/G-2 and commercial Pt/C electrodes, measured in 0.1 M $HClO_4$, with a scan rate of 20 mV s^{-1}. The CVs were obtained under a nitrogen atmosphere.

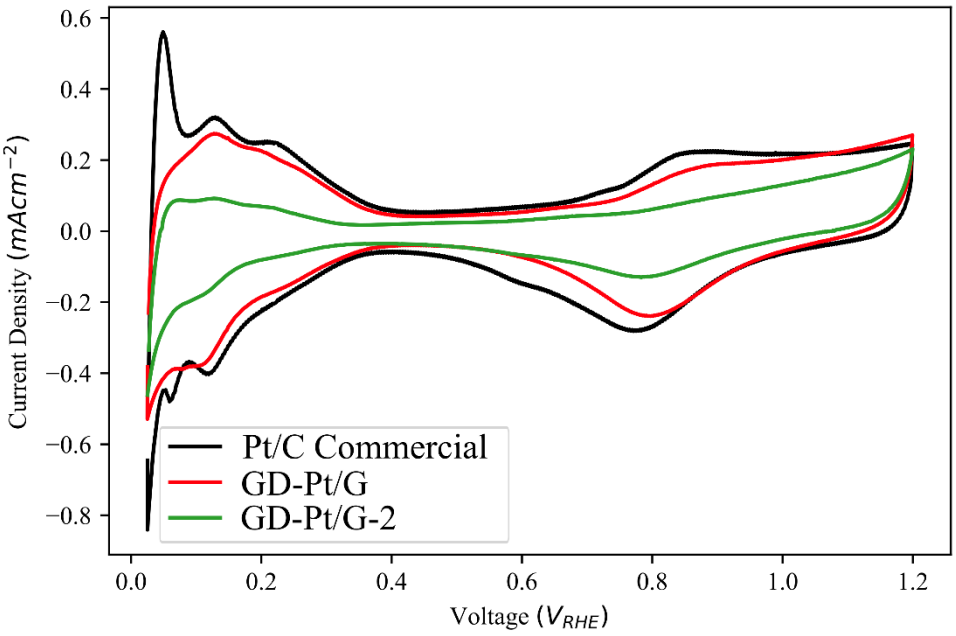

Figure 6-7 *Cyclic voltammetry of GD-Pt/G-2 compared with a commercial Pt/C catalyst and GD-Pt/G.*

In Figure 6-7 it can be observed that the integrated area of the H_{ads} peak of GD-Pt/G-2 is smaller than that of the commercial sample, resulting in a lower measured ECSA. The measured ECSA values are shown in the Table 6-2.

Material	*ECSA (m^2 g_{pt}^{-1})*
GD-Pt/G-2	**15.3**
Pt/C	**54.8**

Table 6-2. *Summary of electrochemical surface area of GD-Pt/G-2 compared with a commercial Pt/C catalyst.*

A lower ECSA suggests that there are fewer active platinum sites present in GD-Pt/G-2, when compared with Pt/C and GD-Pt/G-2. This was not observed for GD-Pt/G, where excess platinum salt was used in the reaction to ensure all graphene present was decorated with platinum nanoparticles. However, as observed in the thermogravimetric analysis of GD-Pt/G-2 presented in Section 6.2.3, it is likely that there is unreacted graphite present in the catalyst powder. It was also observed that the platinum nanoparticles in GD-Pt/G-2 were larger than those of GD-Pt/G, and less uniformly dispersed. Therefore, the lower ECSA is likely to be a result of the combination of these two factors: the nanoparticle size difference between the sample and the unreacted graphite impeding access to some of the platinum nanoparticles. Furthermore, the quality of the film has an impact on the ECSA value and associated performance measured using RDE. Ink formulation optimisation could be carried out for GD-Pt/G-2 in the same way that has been done in the literature for commercial Pt/C, in order to improve dispersion, film quality and therefore RDE performance.[108,138]

Despite a lower ECSA being obtained for GD-Pt/G-2, the activity measured using linear sweep voltammetry resulted in similar performance between the novel and commercial samples. This can be observed by the comparable onset potentials and limiting currents in Figure 6-8. The similarity in performance is reflected in the similar mass activity calculated for the two samples at 0.9 V_{RHE}, as presented in Table 6-3.

Material	**Mass Activity ($A\ mg_{pt}^{-1}$)**	**Specific Activity ($\mu A\ cm_{Pt}^{-2}$)**
GD-Pt/G-2	**0.24**	**1600**
Pt/C	**0.24**	**413**

Table 6-3. *Summary of electrochemical surface area of GD-Pt/G-2 compared with a commercial Pt/C catalyst, calculated at 0.9 V_{RHE}*

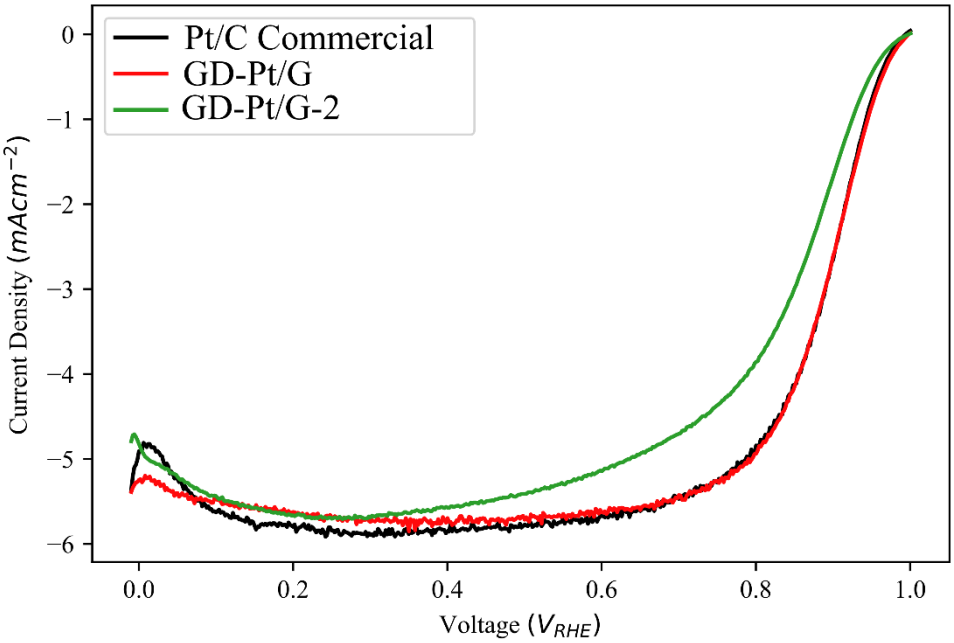

Figure 6-8 *Linear sweep voltammetry of GD-Pt/G-2 compared with a commercial Pt/C catalyst and GD-Pt/G.*

The specific activity is obtained by normalising the calculated kinetic current at 0.9 V_{RHE} to the electrochemical surface area, and as such the lower ECSA of GD-Pt/G-2 results in a higher specific activity at 0.9 V_{RHE} compared with the commercial Pt/C. Although similar, the two voltammograms in Figure 6-9 are not identical: the GD-Pt/G-2 has a lower half-wave potential than the Pt/C sample (0.86 V_{RHE}, 0.89 V_{RHE} respectively) and requires a larger overpotential to achieve its limiting current, which is also lower than that of Pt/C (5.71 mA cm^{-2}, 5.92 mA cm^{-2} respectively).

The combination of having similar kinetic activity but poorer half-wave potential and diffusion-limited current suggests that mass transport of reactants and products of the ORR through the GD-Pt/G-2 sample is worse than through the Pt/C or GD-Pt/G samples. This is consistent with the lower ECSA measured using cyclic voltammetry: GD-Pt/G-2 is effective at catalysing the ORR at low overpotentials but not all of the platinum present in the sample appears to be easily accessible for catalysis.

6.3.2 Membrane Electrode Assembly Testing

Following positive results from RDE testing, GD-Pt/G-2 was prepared as an ink and spray coated onto GDLs for MEA testing, as described in Section 3.6. After conditioning, polarisation curves were obtained at 80 °C under H_2/air, with no back pressure, using a Scribner fuel cell test station. A representative polarisation curve and its associated power density curve obtained from the testing of GD-Pt/G-2 is presented in the Figure 6-9.

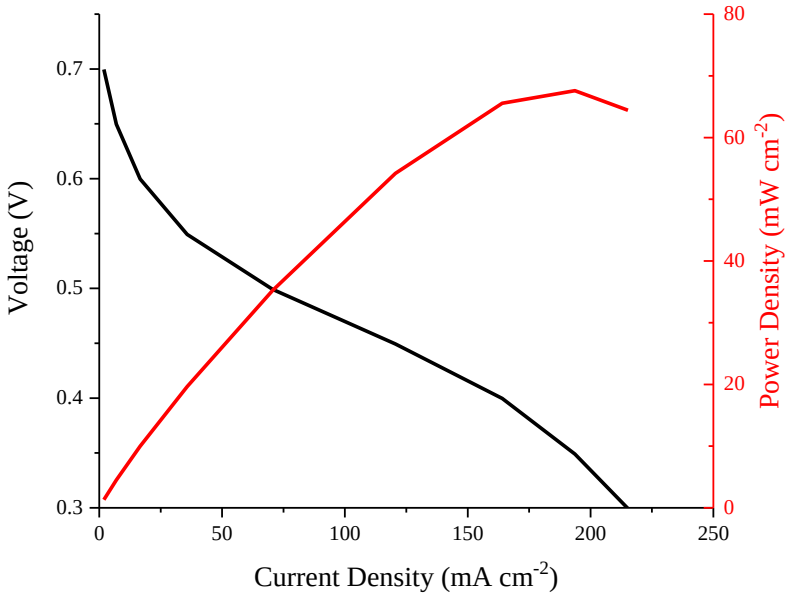

Figure 6-9 *A representative polarisation curve and power curve of GD-Pt/G-2, tested as a 25 cm^2 MEA, under H_2/air with no backpressure, at a temperature of 80 °C. The loading of platinum used was 0.2 mg cm^{-2}.*

With no current load applied to the cell, GD-Pt/G-2 has an open circuit voltage (OCV) of 0.7 V. As the current load is increased the voltage decreases rapidly, showing significant voltage losses across the curve. The current density achieved at 0.3 V is 215 mA cm^{-2}. The maximum power density measured is 67.6 mW cm^{-2}, at a current density of *ca.* 194 mA cm^{-2}. The OCV, current density at 0.3 V and the maximum power density are all significantly lower than what was measured for a commercial Pt/C catalyst, shown in Figure 3-17 presented in Chapter 3, where the OCV is *ca.* 0.87 V, the current density at 0.3 V is *ca.* 1370 mA cm^{-2}, and the maximum power density is *ca.* 446 mW cm^{-2}.

The measured OCV is the minimum overpotential required to catalyse the ORR reaction and is largely defined by the choice of metal used. It is lower than the theoretical OCV (which is equal to the reversible cell potential[10]) due to a combination of irreversible potential losses that arise in part as a result of fuel crossover. In fuel crossover, a small amount of hydrogen permeates the membrane and reacts with O_2 to produce a corresponding cathodic current density that decreases the cathodic potential.[10]

As platinum is used in both GD-Pt/G-2 and in commercial Pt/C MEAs, the reduced OCV in GD-Pt/G-2 cannot be explained by the choice of catalyst metal. It is known that in the case of low loadings of platinum, the potential loss that arises due to fuel crossover is more significant, as the activation losses are considerable.[10,21] The platinum loading "as-sprayed" of 0.2 mg_{pt} cm^{-2} should not lead to such a large decrease in OCV compared with what is typically expected for a platinum catalyst. Therefore, the decrease in OCV is evidence that a proportion of the platinum nanoparticles deposited on the GDL were not able to form triple phase boundaries, likely because of the restacking of the graphene layers blocking platinum nanoparticles from being contacted by ionomer. [21,123]

This is further supported by the rapid decrease in voltage in the kinetic region of the polarisation curve (between 0.7 and 0.5 V), in which the losses are dominated by the available electrochemical surface area of the platinum. The following Ohmic loss region, which is dominated by the ion and electron transport across the MEA, isn't clearly defined and is instead convoluted with mass transport losses (0.5 – 0.3 V), suggesting that reactants and products are being impeded from their transport through the catalyst layer. This again is likely to be the result of the restacking of the graphene layers, a problem common to graphene support materials that has been covered in detail in Section 2.3.

To improve the performance of GD-Pt/G-2, an initial attempt to introduce a spacer during the ink formulation was made. Although there are many different ways to introduce spacers and to design sophisticated graphene-based architectures, as detailed in Section 2.3.3, a method developed in-house by Suter *et al.*[123] was chosen due to its simplicity, scalability and cost-effectiveness. It had been shown previously to improve the performance of a similar graphene-supported platinum catalyst without damaging the graphene support or poisoning the platinum catalyst.[123] In this method, urea crystals are added to the ink before the sonication step, so that when the ink is spray coated onto the GDL, urea crystals deposit between the layers of the graphene, impeding the graphene's tendency to restack. The sprayed GDE is then left in DI water overnight to wash out the majority of the urea, leaving voids between the graphene layers. Before measuring polarisation curves, it is necessary to carry out additional conditioning to remove any remaining urea present in the catalyst layer.

Figure 6-10 presents the polarisation and power curves for the GD-Pt/G-2 samples with and without the urea spacer added.

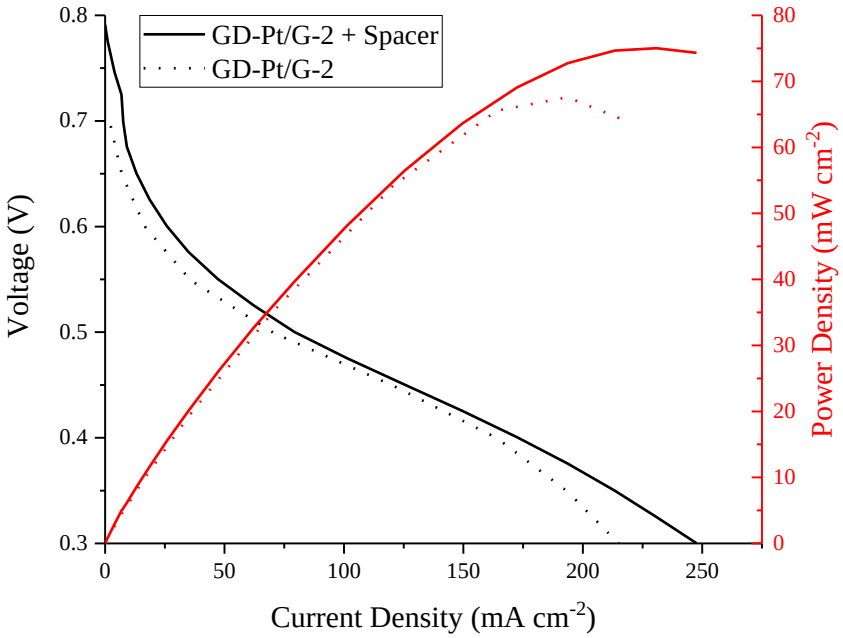

Figure 6-10 *Polarisation curves and power curves of GD-Pt/G-2 with and without a urea additive spacer, denoted by dotted and solid lines respectively*

The polarisation curve of the sample in which a spacer had been added shows a performance improvement, reflected by the increase in OCV (0.791 V), increased maximum power density (75.0 mW cm^{-2}), and larger current density measured at 0.3 V (248 mA cm^{-2}). The increased OCV suggests that the fuel crossover losses are smaller relative to the cathodic potential, compared with the sample without a spacer. It is probable that the introduction of a spacer has improved the accessibility of platinum nanoparticles, increasing their utilisation via an increase in triple-phase boundaries formed. This in turn reduces the activation losses and increases the cathodic potential.

The improvement in current density obtained in 0.4 – 0.3 V likely results from the improved porosity of the material, which facilitates greater mass transport through the catalyst layer. [123]. The differences in the two catalyst layers, with and without the addition of the urea spacer, was investigated using cross-sectional scanning electron microscopy.

6.3.3 Cross-Sectional Scanning Electron Microscopy

Samples were prepared by first cutting a small strip from each of the MEAs after they had been tested. The strips were then set in epoxy resin and polished, as described in Chapter 3. The results obtained from cross-sectional SEM and accompanying EDS maps for the MEA prepared without the addition of the urea spacer are presented in the following Figure 6-11. The SEM image presented was obtained via the measurement of secondary electrons.

In the centre of the image is the Nafion membrane, which is more clearly distinguished by the dense, *ca.* 20-micron strip of fluorine visible in the fluorine (green) EDS map. The deformation and delamination highlighted by dotted red ellipses are thought to have been produced as a result of the SEM sample polishing processes. Below the Nafion membrane is the anode, consisting of the commercial Pt/C catalyst layer deposited on a GDL. The catalyst layer is *ca.* 15 μm thick across the length of the sample, and can be seen to have a roughly uniform distribution of platinum nanoparticles and Nafion from the EDS maps shown in purple (Pt) and green (F) respectively.

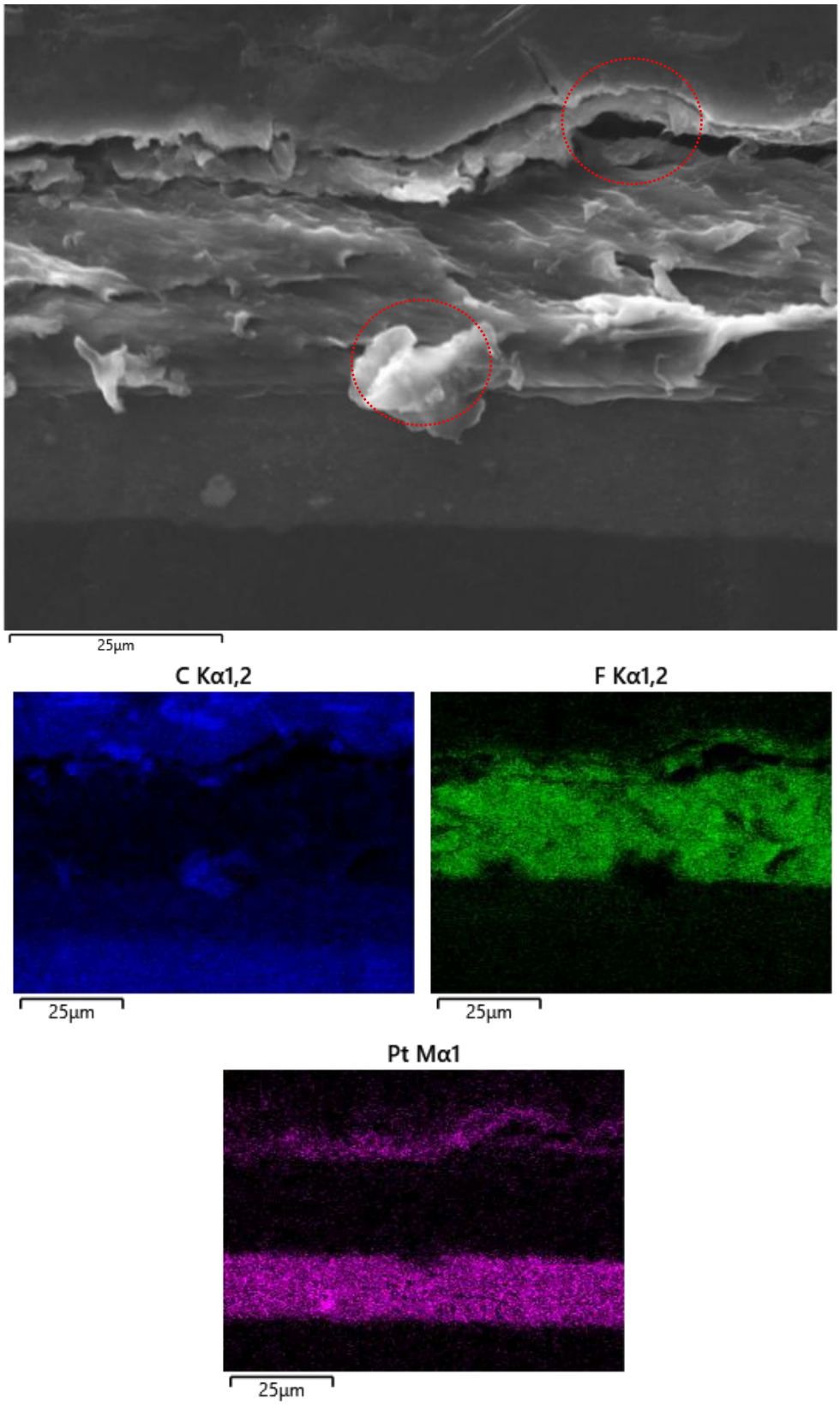

Figure 6-11 *Cross-sectional scanning electron microscopy of the MEA composed of a GD-Pt/G-2 cathode (0.2 mg_{pt} cm^{-2}), Nafion membrane and commercial Pt/C anode (0.4 mg_{pt} cm^{-2}) accompanied by corresponding EDS maps of carbon, flourine and platinum in blue, green and purple respectively*

The catalyst layer of GD-Pt/G-2 mixed with Nafion ionomer can be seen above the central Nafion membrane. As previously mentioned, the catalyst layer appears buckled, and has likely been delaminated from the Nafion membrane and the GDL by the SEM sample preparation process. The thickness of the catalyst layer was measured from the left side of the image (away from the area of delamination) and found to be *ca*. 4.6 μm. This is in agreement with the data presented in the corresponding platinum EDS map (purple), which shows that the catalyst is distributed over a much smaller area as compared to the commercial Pt/C anode. This is as expected of turbostratically restacked graphene materials, which are much less porous than the carbon black materials used in commercial Pt/C catalysts.[123] The decreased brightness of platinum observed on the cathode side compared to the anode side of the map is reflective of the lower loading weight of platinum used: the anode loading weight (0.4 mg_{pt} cm^{-2}) was dictated by the commercial anode material available, and the cathode loadings were calculated to be 0.2 mg_{pt} cm^{-2} due to experimental limitations (the spraying efficiency was lower than anticipated).

Cross-sectional SEM micrographs and accompanying EDS maps of the modified GD-Pt/G-2 MEA that was produced using the sacrificial urea spacer method is presented in Figure 6-12. The micrograph on the left was derived from secondary electron (SE) measurements, and the micrograph on the right from backscattered electrons (BSEs). The SE image shows only a small level of contrast between features, owing to the low roughness of the sample. The low roughness is likely due to a combination of factors, including the local variation in the structure of the MEA and the polishing during the preparation of the sample. BSE images have higher sensitivity to differences in atomic number, thus providing clearer insight into the structure of the sample in this case. The images are rotated by 90 degrees anticlockwise relative to the micrograph in Figure 6-11, with the Nafion membrane layer visible as a vertical strip in the middle of the image, sandwiched between the cathode on its left and the anode on its right. Again, the polishing involved in the sample preparation appears to have caused delamination of the catalyst layer from the Nafion membrane, resulting in cracks visible on the left (cathode) side of the membrane.

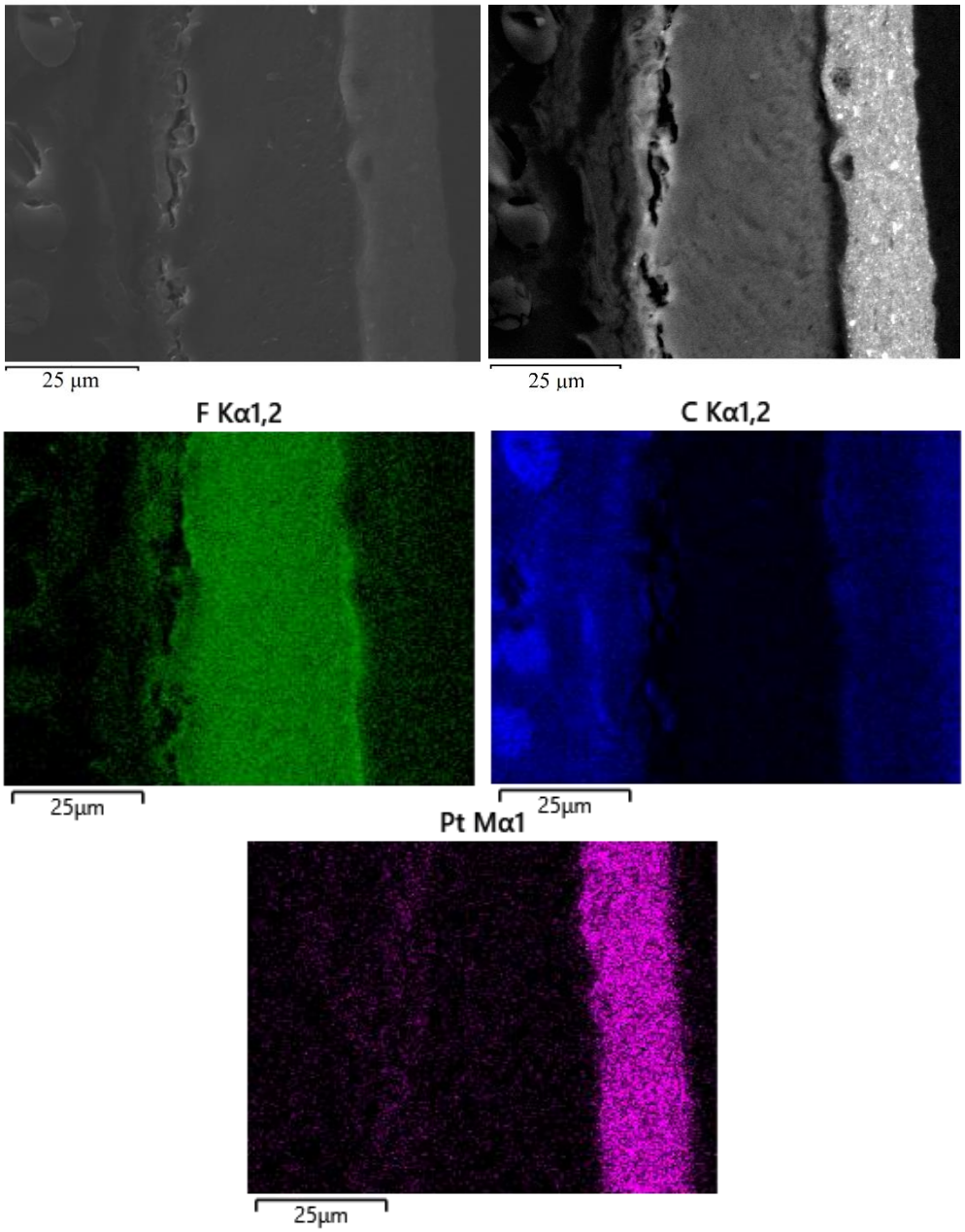

Figure 6-12 *Crossectional SEM micrographs and accompanying maps of the MEA prepared using GD-Pt/G-2 combined with a sacrificail urea additive as a spacer. The micrograph on the left was obtained from the measurement of secondary electrons, the micrograph on the right from backscattered eletrons. EDS maps of flourine, carbon and platinum are shown in green, blue and purple respectively.*

In the BSE image and the fluorine EDS map, it can be observed that the GD-Pt/G-2 catalyst layer is thicker than the in the MEA prepared without the urea spacer (as in Figure 6-11), stretching from the membrane to the left hand edge of the image, across *ca.* 25 µm. There are small gaps present in the catalyst layer that are not clearly observable in the SE image. The fact that they are not clear in the SE image or obvious in the carbon (blue) EDS map suggests that the gaps were formed during the manufacture of the MEA, and then

became filled with epoxy resin during the preparation of the SEM sample. These gaps are therefore likely to have formed by the washing out of urea crystals rather than the polishing steps of the SEM sample preparation. Platinum is observed across the catalyst layer; although the signal is not much higher than the background signal of the detector, it is possible to distinguish the same features in the Pt EDS map as in the F map and the BSE image.

These results suggests that the process of adding urea crystals to the catalyst ink and then removing them by washing the sprayed GDEs with DI water does increase the porosity of the catalyst layer. This is consistent with the small improvements observed in all regions of the polarisation curve presented in Figure 6-10, where a more porous structure could explain the increase in platinum utilisation and mass transport of reactants and products through the catalyst layer. It is also consistent with the findings of Suter *et al.*, whose work this method is adapted from.[123] However, the gaps in the catalyst layer that can be observed in the BSE image and Pt and F EDS maps would be expected to reduce the number of triple phase boundaries formed and therefore be detrimental for catalytic activity. This may therefore be the reason that the addition of spacers only led to a modest improvement in MEA performance, and as such the amount of urea added needs to be varied (likely reduced) to minimise the formation of these larger gaps in the catalyst layer.

6.4 Conclusion

Following the publication of the results presented in Chapters 5 and 6, the next step for GD-Pt/G was to address a number of difficulties in its synthesis method to allow it to be scaled up for testing in a full fuel cell MEA.

The adapted method removed the need for sonication in the production of the graphenide solution and made use of the entire solution, rather than just the supernatant. Although this meant that there was some non-intercalated graphite present in the samples, this greatly increased the concentration of the solution and thereby the amount of product that could be reasonably produced in a lab, from masses on the order of single milligrams to tens and hundreds of milligrams. By substituting $PtCl_2$ with $Pt(DMSO)_2Cl_2$, the sonication required to produce the platinum salt/THF mixture was also removed. Using a platinum salt that is soluble in THF had the further advantage of allowing any excess platinum salt to be easily removed from the products through filtering and washing.

Following the development of the synthesis method, it was necessary to characterise the new material produced, referred to as GD-Pt/G-2. Raman spectroscopy revealed that, similarly to GD-Pt/G, GD-Pt/G-2 consisted of restacked graphene with a low number of defects. TEM was combined with EDS to show that the sample again consisted of platinum nanoparticles decorated on the restacked graphene sheets and the average nanoparticle size was found to be (1.9 ± 0.5) nm. As it was significantly easier to obtain much more powder via the new method than the original one, and because excess platinum salt was removed from the product during the filtration step, it was possible to use thermogravimetric analysis to directly measure how much platinum was present in GD-Pt/G-2. It was found that approximately 10 wt% of the sample consisted of unreacted graphite, and the loading weight of platinum in the sample was 25 wt%.

The catalytic activity of GD-Pt/G-2 toward the ORR was assessed using cyclic and linear sweep voltammetry, and compared with that of the same commercial Pt/C sample as used in Chapter 5. The measured ECSA for GD-Pt/G-2 was lower than that of GD-Pt/G and Pt/C. This may be as a result of excess graphite hindering the performance of the catalyst by blocking access to platinum nanoparticles and the increased size of the platinum nanoparticles compared with GD-Pt/G.

Despite the decreased ECSA, GD-Pt/G-2 showed comparable activity in direct measurements of ORR carried out using linear sweep voltammetry, with similar onset potentials and limiting currents to those of Pt/C and GD-Pt/G. However, the half-wave potential is left-shifted compared to that of Pt/C, and the diffusion-limited current plateau is less well developed, which is further evidence to suggest that mass transport to platinum nanoparticles is a problem for this material. The specific activity at 0.9 V_{RHE} was found to be four times greater than that of Pt/C, but this is a reflection of how the specific activity is calculated: the kinetic current at 0.9 V_{RHE} is normalised to the available ECSA, which is lower for GD-Pt/G-2 than Pt/C. As such, the greater specific activity at 0.9 V_{RHE} of GD-Pt/G-2 does not fully represent the catalytic activity of the sample across the whole potential range. At 0.9 V_{RHE} it appears that there is enough accessible platinum to provide enough active sites to catalyse a similar amount of ORR as the Pt/C, but this does not continue at lower potentials where mass-transport effects dominate.

To test the performance of GD-Pt/G-2 in a full fuel cell, an MEA was produced by spray coating a commercially available GDL with an ink consisting of GD-Pt/G-2, water, IPA and Nafion polymer, forming the cathode-side catalyst layer of the MEA. This was hot pressed together with a commercial Pt/C catalyst layer and a Nafion membrane and tested using a Scribner fuel cell test station. The polarisation curve obtained for GD-Pt/G-2 confirmed the sample had platinum present and was active toward ORR, but that the performance was greatly limited by the common, expected difficulty of platinum nanoparticle-accessibility and mass-transport through a restacked-graphene electrode.

To alleviate this issue, another MEA was prepared with urea crystals added as an additional, sacrificial "spacer" following a method developed in-house by Suter *et al*. Following the spray-coating of the ink, the MEA was left in DI water overnight to wash out the urea crystals. The polarisation curve and power curve obtained showed an improvement in activity, with a greater OCV suggesting more platinum nanoparticles were now accessible, and smaller polarisation losses throughout the curve suggesting improved mass-transport. Cross-sectional SEM was used to determine the impact of the addition of the urea spacer to the resulting MEA structure, and it was found that the method did increase the porosity of the catalyst layer. However, larger gaps were also observed in the catalyst layer that are likely to have had a negative impact on the performance of the electrode through the reduction in the number of triple phase boundaries. Therefore, future experiments should investigate how the catalyst layer structure and MEA performance change with varying ratios of urea to catalyst present in the catalyst ink.

Overall, compared with the MEA without the spacer method, the improved MEA achieved a maximum power density of 75.0 mW cm^{-2}, and slightly improved current density measured at 0.3 V of 248 mA cm^{-2}. As such there are many aspects of the catalyst design beyond the addition of urea that are in need of optimisation and improvement, suggestions for which are discussed in the Future Work section of Chapter 7.

Chapter 7: Conclusions

As governments and industries around the world accelerate our transition to a green and sustainable future, hydrogen looks highly likely to play a fundamental role in the energy mix. For this to be successful, hydrogen fuel cells must decrease in price and increase in working lifetime, which in turn requires innovation in the design and synthesis of catalyst-support materials.

Although graphene's unique properties make it a promising catalyst-support material that has been widely researched for many years, the field has yet to produce a material that has reached the commercial market. Graphene is outcompeted in price and ease of synthesis by the already well-established commercial carbon black materials, and as such any graphene material that is to realistically improve the performance or lifetime of a functioning fuel cell, it has to both be produced via a scalable synthesis method and show significant improvements in rigorous accelerated stress tests. In this thesis, work towards this goal is presented through the development and testing of graphenide-derived platinum on graphene, GD-Pt/G.

GD-Pt/G was synthesised via the reaction of platinum chloride with the supernatant of a graphenide solution produced via the sonication of an ammoniated potassium-intercalated graphite, $KC_{24}(NH_3)_{1.3}$. The material was characterised using Raman spectroscopy and transmission electron microscopy, which together suggested it was composed of platinum nanoparticles decorated on graphene sheets that had then restacked turbostratically. The nanoparticles were found on average to be 1.7 nm with an edge-to-edge distance of 0.8 nm, an ideal size and distribution for oxygen reduction reaction catalysis. The loading weight of platinum was estimated by XPS to be 11.5 wt%. This calculation was made more convoluted by the presence of excess $PtCl_2$, which was difficult to remove, and limited by the small amount of GD-Pt/G that could be produced at any one time due to the very low concentration of the supernatant of the graphenide solutions used during the reaction step of the synthesis process.

Electrochemical testing of GD-Pt/G was carried out using rotating disk electrochemical techniques in a three-electrode cell. Solutions of reacted GD-

Pt/G in THF were used as synthesised as the catalyst ink, with a small amount of Nafion solution deposited on top of the electrode as a binding layer. Cyclic voltammograms revealed that while $PtCl_2$ had no discernible features, GD-Pt/G showed peaks characteristic of platinum-hydrogen adsorption/desorption and Pt oxidation/PtO reduction, and as such the electrochemical surface area of GD-Pt/G could be determined. It was found to be greater than that of a commercial Pt/C sample tested under the same conditions, which may be due to the optimal size and distribution of the platinum nanoparticles. The ORR activity was benchmarked using linear sweep voltammetry and obtained voltammograms showed GD-Pt/G's excellent activity toward the ORR, matching the catalytic reaction mechanism of the commercial Pt/C catalyst while surpassing it in activity benchmarks.

Following adapted RDE DoE protocols, accelerated stress tests were carried out across both the "startup/shutdown" (0.6 – $1V_{RHE}$) and "continuous-operation" (1-$1.6V_{RHE}$) potential ranges, which target platinum corrosion and carbon corrosion respectively. GD-Pt/G was shown to demonstrate very high stability, showing smaller decreases in ECSA and performance compared to Pt/C across a larger number of cycles in the "continuous-operation" potential range than previously reported. The improvement in the stability of platinum nanoparticles was further evidenced using identical location TEM, which showed very little change in the nanoparticles before and after 30000 cycles. This was suggested to be due to the nanoparticle deposition method used, in which the platinum salt is directly reduced by the negatively charged graphene sheets without the need for a further reduction agent. The carbon corrosion stability was attributed to the high-quality nature of the restacked graphene support, which was demonstrated to have a low number of defects by the ratio of the D and G peaks obtained through Raman spectroscopy.

While the results presented in Chapters 4 and 5 demonstrated that GD-Pt/G was both catalytically active and highly stable for oxygen reduction reaction at a three-electrode cell level, it was necessary to make a number of changes to the synthesis method before it could be tested in a full fuel cell. To simplify the complications surrounding excess platinum chloride that was difficult to remove, a platinum salt that was soluble in THF, $Pt(DMSO)_2Cl_2$, was used. This meant that any excess salt could be washed through during filtration of

the solutions. To improve the scalability of the synthesis method, sonication was replaced with stirring, and the full graphenide solution was used in-place of just the supernatant. This increased the concentration of the resultant GD-Pt/G-2 solutions by an order of magnitude compared with the GD-Pt/G solutions, and could be reasonably filtered to obtain a working quantity of powder. Characterisation of GD-Pt/G-2 with Raman spectroscopy revealed the material was comprised of restacked graphene with a low number of defects, similar to GD-Pt/G. TEM and EDS were used together to show that the graphene sheets were decorated with platinum nanoparticles, but the material was found qualitatively to be thicker than GD-Pt/G, likely due to excess unreacted graphite remaining in the sample. The nanoparticles were on average larger than those of GD-Pt/G (1.9 nm vs 1.7 nm), although still an appropriate size for ORR catalysis. TGA measurements showed that approximately 10% of the mass of the powder was unreacted graphite and that the platinum loading weight was *ca.* 25 wt%.

Fuel cell tests were conducted with GD-Pt/G-2. Polarisation and power density curves showed that the material was active for ORR, but was greatly limited by the restacking of graphene. The restacking impeded both the mass-transport through the electrode layer and the formation of triple phase boundaries by blocking platinum nanoparticles. To improve performance, an in-house method developed by Suter *et al.* was implemented. Urea crystals were added to the ink before spray coating, and then removed via washing with water, leaving voids in the catalyst layer structure. Polarisation and power curves reflected a modest improvement in performance across the full potential range, with cross-sectional SEM showing that the structure had been successfully spaced by the addition and removal of urea crystals. As such, the performance improvement is attributed to the improvement of porosity throughout the catalyst layer, improving the utilisation of the platinum nanoparticles and the mass-transport of reactants and products through the material.

7.1 Ongoing and Future work

The work presented in Chapters 4 and 5 of this thesis was conducted prior to the outbreak of Covid-19 in March 2020. The work was patented and published in the journal Nanoscale during the first UK lockdown. The following period was greatly disrupted by further Covid-19 waves and lockdowns, greatly limiting access to labs, with "normal" lab work not resuming until April 2021. As such, there are a number of different threads of work for which preliminary results were obtained but were not sufficiently developed in the timeframe of this project to be included in the thesis. This section details future work and, where relevant, describes initial investigations that were carried out relevant to the ideas presented for future experiments.

7.1.1 Graphenide-Derived Materials

In Chapter 4, IL TEM was presented as evidence for the stability of platinum nanoparticles after 30000 0.6 and 1 V_{RHE} cycles. However, it was not possible to obtain an equivalent set of ILTEM images in the "carbon corrosion" range of 1-1.6 V_{RHE} as at high potentials, as the gold TEM grids are not stable above 1.4 V_{RHE}, and are known to produce gold nanoparticles. Therefore, it would be valuable to investigate the carbon corrosion of GD-Pt/G materials using other experiments. One possibility that was very briefly explored was the use of electrochemical atomic force microscopy (EC AFM), where the sample is electrochemically cycled while being imaged with AFM. This has a further advantage over ILTEM that it is an in-situ technique, meaning that any changes in the graphene sheets could be observed in real-time as cycling is performed.

There are a range of characterisation techniques that could be further applied to better understand the GD-Pt/G materials. Surface area measurements could be obtained using Brunauer–Emmett–Teller (BET) analysis. Microwave plasma atomic emission spectroscopy (MP-AES) was attempted to further verify the platinum loading weight present in GD-Pt/G-2, but the technique as performed in our lab failed to yield accurate values for a known

commercial Pt/C standard powder. With further improvement in experimental technique, MP-AES could provide a more accurate measurement of platinum loading weight that TGA. Similarly, inductively-coupled plasma mass spectroscopy could also be used for this purpose.

7.1.2 Fuel Cell Electrode Manufacture, Characterisation and Testing

Initial attempts at the manufacture of GD-Pt/G-2 fuel cell electrodes have been described in Chapter 6. Each step of the process requires further optimisation, as there was only time for one attempt at each electrode (without and with the urea additive). In both cases, the formulation of the ink could be varied, with the ratios of water, IPA, and Nafion optimised to improve the dispersion and stability of the ink. This in turn impacts the spraying efficiency of the ink through the spray-coater, which in-part dictates the structure of the electrode produced. The percentage of Nafion solution in the ink also impacts the number of triple-phase boundaries formed, with too much or too little resulting in reduced performance of the electrode. In the case of the electrode made with the urea additive, the mass of urea added was found to be optimum by Suter *et al*. for a different graphene material,[123] but had yet to be optimised for GD-Pt/G-2. Therefore, similar experiments would need to be conducted where the amount of urea added would be varied and the performance measured to find an appropriate mass of urea to add.

In all of the proposed optimisation experiments above, the electrodes would need to be characterised to investigate the difference between them as the parameters are varied. This could be achieved using BET analysis to measure the surface area and porosity of the electrodes, as well as cross-sectional SEM as described in this thesis. The elemental composition of the catalyst layers could also be quantified with XPS, which can be used to determine if urea is left in the sample by the change in nitrogen content before and after washing the electrode. Raman spectroscopy can be used to measure the D:G ratio of the electrodes, measuring changes in the defects of the graphene materials with the varying of parameters.

Further fuel cell testing of electrodes should be conducted. It is known that there are many ways to condition a fuel cell electrode, and a number should

be investigated to find a method that is most appropriate for GD-Pt/G-2. Experiments where the operating parameters are varied, and performance measured could be conducted to investigate the effects of temperature and pressure on the material. Beyond polarisation curves, cyclic voltammetry could be used to quantify the electrochemical surface areas of electrodes tested, and electrochemical impedance spectroscopy can be employed to calculate various resistances throughout the cell, allowing for further characterisation and understanding of the electrodes tested.

One of the most important issues for fuel cell electrodes is their stability over time, and as such accelerated stress tests, as described by the DoE, should be conducted to investigate the durability of electrodes produced. Beyond simply measuring the change in performance, as benchmarked by changes in ECSAs, polarisation curves and power density values, further characterisation of corroded electrodes is required to properly understand the degradation mechanisms of the materials being studied, something that is often neglected in the literature. As well as the list of characterisation techniques described above, *in-situ* neutron scattering experiments or X-ray computer tomography could be used to further investigate the changes in the electrode structure before, during and after cycling.

Several nanoparticle architectures are currently found in commercial fuel cell catalysts, often involving alloys with other metals. Penicaud *et al.* have published other examples of different metal salts being reduced by different graphenide solutions, and ongoing research within our group is investigating the synthesis of manganese and bismuth nanoparticles on graphene for other electrochemical applications. During this project, initial attempts were made to produce palladium nanoparticles via the reduction of palladium chloride by KC_8-based graphenide solutions, and TEM, EDS and RDE results showed that the resultant graphenide-derived palladium on graphene (GD-Pd/G) was active toward the ORR. Initial investigations into the co-reduction of palladium and platinum salt by a single graphenide solution were also conducted. Preliminary TEM and EDS results suggested the presence of both platinum and palladium in the sample, with nanoparticles decorating sheets of restacked graphene. The mixture of metallic platinum and palladium was further evidenced by linear sweep voltammograms obtained using RDE,

which showed the features of both platinum and palladium in the catalysis of the ORR and hydrogen evolution reaction. As the work was conducted with KC_8, rather than $KC_{24}(NH_3)_{1.3}$, and was not completed within the timeframe of the project due Covid-19 disruption, it was not included in the main body of this thesis. Future work should repeat these preliminary experiments with $KC_{24}(NH_3)_{1.3}$, and explore the potential for producing alloy nanoparticles, especially with commercially relevant metals such as palladium, nickel, and cobalt.

As explained in Chapters 3 and 6, the restacking of graphene is a significant issue with the manufacture of graphene-supported catalyst materials. In Chapter 6, an in-house technique made use of urea as a sacrificial spacer, which could be easily removed to introduce pores between the graphene sheets, thus improving the performance. However, this is only one of many ways that the problem of restacking can be tackled. Many works introduce an additional carbon material such as carbon black or carbon nanotubes to the system to improve porosity and thereby platinum utilisation and mass transport in the catalyst layer of the electrode. Each carbon material has its pros and cons: for example, carbon black is low-cost and readily available, but it is known to be unstable under the high potentials experienced during the start-up and shutdown of a fuel cell, whereas carbon nanotubes are much more expensive and difficult to produce, but offer high conductivity and stability. Therefore, each could be thoroughly investigated to determine which is most suitable for producing the best-performing electrodes.

In most cases presented in the literature review of this thesis, the additional carbon spacer is added to the material after the deposition of platinum nanoparticles onto graphene sheets. The method presented in this thesis offers a unique way to combine graphene with other carbon materials: it has been shown that carbon nanotubes can be charged by intercalation of alkali metals analogously to the graphite intercalation compounds used in this work, and the intercalation and charging of other amorphous carbons is currently the subject of ongoing research within the research group. By taking two different intercalation compounds, such as a GIC and intercalated carbon nanotubes, they could be mixed either directly in the same solution, or two separate charged carbon solutions could be mixed, before metal salts are added to

produce a composite catalyst material containing a mixture of carbon materials. In the case of graphene and nanotubes, this combination method is novel and distinct from any methods described by the papers reviewed in Chapter 3, and therefore should be investigated.

7.1.3 Beyond Fuel Cell Catalysts

Taking further advantage of the method of using ionic solutions of 2D materials, early investigations into mixing distinct nanomaterials in solution were conducted. Potassium-intercalated molybdenum disulphide and potassium-intercalated graphite were mixed in solution and the resultant materials were characterised with Raman spectroscopy. Although initial results were inconclusive, if this method could be developed it could provide a scalable route to the production of 2D heterostructures. These solutions of mixtures of charged 2D materials can then be reacted with metal salts to produce hybrid materials for various applications. For example, MoS_2 is known to catalyse the hydrogen evolution reaction, required for water electrolysis. Platinum decorated MoS_2 was produced during my Master's project and shown to catalyse HER using RDE, but the material's performance was impeded by the semi-conducting nature of 2H-phase MoS_2. The introduction of graphene into such a system could be an effective way to improve the conductivity of the system while also increasing the available ECSA and therefore could be the topic of future work.

Bibliography

1. Dresselhaus, M.S.; Thomas, I. . Alternative energy technologies. *Nature* **414**, 332–337 (2001).

2. Chu, S. & Majumdar, A. Opportunities and challenges for a sustainable energy future. *Nature* **488**, 294–303 (2012).

3. Aneke, M. & Wang, M. Energy storage technologies and real life applications – A state of the art review. *Appl. Energy* **179**, 350–377 (2016).

4. Schultz, M. G., Diehl, T., Brasseur, G. P. & Zittel, W. Air Pollution and Climate-Forcimg Impacts of a Global Hydrogen Economy. *Science (80-.).* **302**, 624–627 (2003).

5. Panwar, N. L., Kaushik, S. C. & Kothari, S. Role of renewable energy sources in environmental protection: A review. *Renew. Sustain. Energy Rev.* **15**, 1513–1524 (2011).

6. Zakeri, B. & Syri, S. Electrical energy storage systems: A comparative life cycle cost analysis. *Renew. Sustain. Energy Rev.* **42**, 569–596 (2015).

7. Rowley-Neale, S. J. *et al.* 2D molybdenum disulphide (2D-MoS_2) modified electrodes explored towards the oxygen reduction reaction. *Nanoscale* **8**, 14767–14777 (2016).

8. Wang, G. *et al.* Progress on design and development of polymer electrolyte membrane fuel cell systems for vehicle applications: A review. *Fuel Process. Technol.* **179**, 203–228 (2018).

9. UCL. Hydrogen Fuel Cells. https://www.ucl.ac.uk/ucell/about/hydrogen-fuel-cells-2.

10. Zhang, J. *PEM Fuel Cell Electrocatalysts and Catalyst Layers*. (Springer London, 2008). doi:10.1007/978-1-84800-936-3.

11. Sharma, S. & Pollet, B. G. Support materials for PEMFC and DMFC electrocatalysts—A review. *J. Power Sources* **208**, 96–119 (2012).

12. Zhou, X., Qiao, J., Yang, L. & Zhang, J. A Review of Graphene-Based Nanostructural Materials for Both Catalyst Supports and Metal-Free Catalysts in PEM Fuel Cell Oxygen Reduction Reactions. *Adv. Energy Mater.* **4**, 1301523 (2014).

13. Arenz, M. & Zana, A. Fuel cell catalyst degradation: Identical location electron microscopy and related methods. *Nano Energy* **29**, 299–313 (2016).

14. Novoselov, K. S. *et al.* Electric Field Effect in Atomically Thin Carbon Films. *Science (80-.).* **306**, 666–669 (2004).

15. Julkapli, N. M. & Bagheri, S. Graphene supported heterogeneous catalysts: An overview. *Int. J. Hydrogen Energy* **40**, 948–979 (2015).

16. Liu, M., Zhang, R. & Chen, W. Graphene-Supported

Nanoelectrocatalysts for Fuel Cells : Synthesis , Properties , and Applications. *Chem. Rev.* **114**, 5117–5160 (2014).

17. Böhm, S. Graphene against corrosion. *Nat. Nanotechnol.* **9**, 741–742 (2014).

18. Cullen, P. L. *et al.* Ionic solutions of two-dimensional materials. *Nat. Chem.* **9**, 244–249 (2017).

19. Milner, E. M. *et al.* Structure and morphology of charged graphene platelets in solution by small-angle neutron scattering. *J. Am. Chem. Soc.* **134**, 8302–8305 (2012).

20. Holton, O. T. & Stevenson, J. W. The Role of Platinum in Proton Exchange Membrane Fuel Cells. *Platin. Met. Rev* **57**, 259–271 (2013).

21. Suter, T. A. M. *et al.* Engineering Catalyst Layers for Next-Generation Polymer Electrolyte Fuel Cells: A Review of Design, Materials, and Methods. *Adv. Energy Mater.* **11**, 2101025 (2021).

22. Smith, M. & Savinell, R. F. MICRO FUEL CELLS. *The Electrochemical Society: Electrochemistry Encyclopedia* https://knowledge.electrochem.org/encycl/art-f05-fc-micro.htm (2013).

23. Wu, J. *et al.* Diagnostic tools in PEM fuel cell research: Part I Electrochemical techniques. *Int. J. Hydrogen Energy* **33**, 1735–1746 (2008).

24. Ghosh, S. *et al.* Recent advances in three-dimensional graphene based materials for catalysis applications. *Adv. Mater.* **60**, 203–228 (2018).

25. Seselj, N., Engelbrekt, C. & Zhang, J. Graphene-supported platinum catalysts for fuel cells. *Sci. Bull.* **60**, 864–876 (2015).

26. Abdelhafiz, A., Vitale, A. & Buntin, P. Epitaxial and atomically thin graphene–metal hybrid catalyst films: the dual role of graphene as the support and the chemically-transparent protective cap. *Energy Environ. Sci.* **11**, 1610–1616 (2018).

27. Rao, C. V. & Viswanathan, B. Monodispersed Platinum Nanoparticle Supported Carbon Electrodes for Hydrogen Oxidation and Oxygen Reduction in Proton Exchange Membrane Fuel Cells. *J. Phys. Chem. C* **114**, 8661–8667 (2010).

28. Li, Y. Y. *et al.* Stabilization of high-performance oxygen reduction reaction Pt electrocatalyst supported on reduced graphene oxide/carbon black composite. *J. Am. Chem. Soc.* **134**, 12326–12329 (2012).

29. Marković, N. M., Schmidt, T. J., Stamenković, V. & Ross, P. N. Oxygen Reduction Reaction on Pt and Pt Bimetallic Surfaces: A Selective Review. *Fuel Cells* **1**, 105–116 (2001).

30. Shao, M., Peles, A. & Shoemaker, K. Electrocatalysis on platinum nanoparticles: Particle size effect on oxygen reduction reaction activity. *Nano Lett.* **11**, 3714–3719 (2011).

31. Chung, D. Y., Yoo, J. M. & Sung, Y. E. Highly Durable and Active Pt-Based Nanoscale Design for Fuel-Cell Oxygen-Reduction Electrocatalysts. *Adv. Mater.* **30**, 1704123 (2018).

32. Dubau, L., Castanheira, L., Berthomé, G. & Maillard, F. An identical-location transmission electron microscopy study on the degradation of Pt/C nanoparticles under oxidizing, reducing and neutral atmosphere. *Electrochim. Acta* **110**, 273–281 (2013).

33. Fuel cell Technologies Office: Multi-year Research, Development and Demonstration Plan. https://www.energy.gov/sites/prod/files/2017/05/f34/fcto_myrdd_fuel_cells.pdf (2016).

34. Nagai, T., Murata, H. & Morimoto, Y. Influence of Experimental Conditions on the Catalyst Degradation in the Durability Test. *J. Electrochem. Soc.* **161**, F789–F794 (2014).

35. Riese, A., Banham, D., Ye, S. & Sun, X. Accelerated Stress Testing by Rotating Disk Electrode for Carbon Corrosion in Fuel Cell Catalyst Supports. *J. Electrochem. Soc.* **162**, F783–F788 (2015).

36. Peres, N. M., Neto, A. C. & Guinea, F. Drawing conclusions from graphene. *Phys. World* 1–5 (2006) doi:[193.171.33.83.

37. Castro Neto, A. H., Guinea, F., Peres, N. M. R., Novoselov, K. S. & Geim, A. K. The electronic properties of graphene. *Rev. Mod. Phys.* **81**, 109–162 (2009).

38. Choi, H. J. *et al.* Graphene for energy conversion and storage in fuel cells and supercapacitors. *Nano Energy* **1**, 534–551 (2012).

39. Zhu, Y. *et al.* Graphene and graphene oxide: Synthesis, properties, and applications. *Adv. Mater.* **22**, 3906–3924 (2010).

40. Jason Stafford, Andrius Patapas, Nwachukwu Uzo, Omar K. Matar, C. P. Towards Scale-up of Graphene Production via Nonoxidizing Liquid Exfoliation Methods. *VTT Publ.* **00**, 3–194 (2003).

41. Xu, Y., Cao, H., Xue, Y., Li, B. & Cai, W. Liquid-Phase Exfoliation of Graphene: An Overview on Exfoliation Media, Techniques, and Challenges. *Nanomaterials* **8**, 942 (2018).

42. Kidambi, P. R. *et al.* A Scalable Route to Nanoporous Large-Area Atomically Thin Graphene Membranes by Roll-to-Roll Chemical Vapor Deposition and Polymer Support Casting. *ACS Appl. Mater. Interfaces* **10**, 10369–10378 (2018).

43. Chen, D., Feng, H. & Li, J. Graphene oxide: Preparation, functionalization, and electrochemical applications. *Chem. Rev.* **112**, 6027–6053 (2012).

44. Hummers, W. S. & Offeman, R. E. Preparation of Graphitic Oxide. *J. Am. Chem. Soc.* **80**, 1339 (1958).

45. Tsang, A. C. H., Kwok, H. Y. H. & Leung, D. Y. C. The use of graphene based materials for fuel cell, photovoltaics, and supercapacitor electrode materials. *Solid State Sci.* **67**, A1–A14

(2017).

46. Liu, J., Ma, Q., Huang, Z., Liu, G. & Zhang, H. Recent Progress in Graphene-Based Noble-Metal Nanocomposites for Electrocatalytic Applications. *Adv. Mater.* **1800696**, 1800696 (2019).

47. Kou, R. *et al.* Enhanced activity and stability of Pt catalysts on functionalized graphene sheets for electrocatalytic oxygen reduction. *Electrochem. commun.* **11**, 954–957 (2009).

48. Yin, H., Tang, H., Wang, D., Gao, Y. & Tang, Z. Facile synthesis of surfactant-free Au cluster/graphene hybrids for high-performance oxygen reduction reaction. *ACS Nano* **6**, 8288–8297 (2012).

49. Huang, Y.-X., Xie, J.-F., Zhang, X., Xiong, L. & Yu, H.-Q. Reduced Graphene Oxide Supported Palladium Nanoparticles via Photoassisted Citrate Reduction for Enhanced Electrocatalytic Activities. *ACS Appl. Mater. Interfaces* **6**, 15795–15801 (2014).

50. Sun, L. *et al.* One-Step Synthesis of Dendritic Bimetallic PtPd Nanoparticles on Reduced Graphene Oxide and Its Electrocatalytic Properties. *Electrochim. Acta* **188**, 845–851 (2016).

51. Zheng, Y. *et al.* Component-controlled synthesis and assembly of Cu-Pd nanocrystals on graphene for oxygen reduction reaction. *ACS Appl. Mater. Interfaces* **7**, 5347–5357 (2015).

52. Xu, S. & Wu, P. Facile and green synthesis of a surfactant-free Au clusters/reduced graphene oxide composite as an efficient electrocatalyst for the oxygen reduction reaction. *J. Mater. Chem. A* **2**, 13682–13690 (2014).

53. Zhang, P. *et al.* Durability and activity tunable Pt/graphene catalyst for oxygen reduction reactions. *Int. J. Electrochem. Sci.* **11**, 10763–10778 (2016).

54. Mu, X. *et al.* Graphene-carbon nanofiber hybrid supported Pt nanoparticles with enhanced catalytic performance for methanol oxidation and oxygen reduction. *Electrochim. Acta* **253**, 171–177 (2017).

55. Wojnicki, M. *et al.* Catalytic Properties of Platinum Nanoparticles Obtained in a Single Step Simultaneous Reduction of Pt(IV) Ions and Graphene Oxide. *J. Flow Chem.* **5**, 22–30 (2015).

56. Chen, X. *et al.* Platinized Graphene/ceramics Nano-sandwiched Architectures and Electrodes with Outstanding Performance for PEM Fuel Cells. *Sci. Rep.* **5**, 1–10 (2015).

57. Wang, R. *et al.* Controlled growth of platinum nanowire arrays on sulfur doped graphene as high performance electrocatalyst. *Sci. Rep.* **3**, 1–7 (2013).

58. Speder, J. *et al.* Comparative degradation study of carbon supported proton exchange membrane fuel cell electrocatalysts – The influence of the platinum to carbon ratio on the degradation rate. *J. Power Sources* **261**, 14–22 (2014).

59. Kauffman, D. R. & Star, A. Graphene versus carbon nanotubes for chemical sensor and fuel cell applications. *Analyst* **135**, 2790–2797 (2010).

60. Du, L. *et al.* Advanced catalyst supports for PEM fuel cell cathodes. *Nano Energy* **29**, 314–322 (2016).

61. Divya, P. & Ramaprabhu, S. Platinum-graphene hybrid nanostructure as anode and cathode electrocatalysts in proton exchange membrane fuel cells. *J. Mater. Chem. A* **2**, 4912–4918 (2014).

62. Ghosh, A., Basu, S. & Verma, A. Graphene and functionalized graphene supported platinum catalyst for PEMFC. *Fuel Cells* **13**, 355–363 (2013).

63. Sui, S. *et al.* A comprehensive review of Pt electrocatalysts for the oxygen reduction reaction: Nanostructure, activity, mechanism and carbon support in PEM fuel cells. *J. Mater. Chem. A* **5**, 1808–1825 (2017).

64. Jung, J. H., Park, H. J., Kim, J. & Hur, S. H. Highly durable Pt/graphene oxide and Pt/C hybrid catalyst for polymer electrolyte membrane fuel cell. *J. Power Sources* **248**, 1156–1162 (2014).

65. Park, S. *et al.* Design of graphene sheets-supported Pt catalyst layer in PEM fuel cells. *Electrochem. commun.* **13**, 258–261 (2011).

66. Işıkel Şanlı, L., Bayram, V., Ghobadi, S., Düzen, N. & Alkan Gürsel, S. Engineered catalyst layer design with graphene-carbon black hybrid supports for enhanced platinum utilization in PEM fuel cell. *Int. J. Hydrogen Energy* **42**, 1085–1092 (2017).

67. Yarar Kaplan, B., Haghmoradi, N., Biçer, E., Merino, C. & Alkan Gürsel, S. High performance electrocatalysts supported on graphene based hybrids for polymer electrolyte membrane fuel cells. *Int. J. Hydrogen Energy* **43**, 23221–23230 (2018).

68. Shao, Y. *et al.* Highly durable graphene nanoplatelets supported Pt nanocatalysts for oxygen reduction. *J. Power Sources* **195**, 4600–4605 (2010).

69. Daş, E., Kaplan, B. Y., Gürsel, S. A. & Yurtcan, A. B. Graphene nanoplatelets-carbon black hybrids as an efficient catalyst support for Pt nanoparticles for polymer electrolyte membrane fuel cells. *Renew. Energy* **139**, 1099–1110 (2019).

70. Kim, T., Xie, T., Jung, W. S. & Popov, B. N. Development of ultra–low highly active and durable hybrid compressive platinum lattice cathode catalysts for polymer electrolyte membrane fuel cells. *Int. J. Hydrogen Energy* **42**, 12507–12520 (2017).

71. Takahashi, K., Koda, R., Kakinuma, K. & Uchida, M. Improvement of Cell Performance in Low-Pt-Loading PEFC Cathode Catalyst Layers with Pt/Ta-SnO 2 Prepared by the Electrospray Method . *J. Electrochem. Soc.* **164**, F235–F242 (2017).

72. Castanheira, L. *et al.* Carbon corrosion in proton-exchange membrane

fuel cells: Effect of the carbon structure, the degradation protocol, and the gas atmosphere. *ACS Catal.* **5**, 2184–2194 (2015).

73. Liu, P., Kong, J., Liu, Y., Liu, Q. & Zhu, H. Graphitic mesoporous carbon based on aromatic polycondensation as catalyst support for oxygen reduction reaction. *J. Power Sources* **278**, 522–526 (2015).

74. He, Q., Suraweera, N. S., Joy, D. C. & Keffer, D. J. Structure of the ionomer film in catalyst layers of proton exchange membrane fuel cells. *J. Phys. Chem. C* **117**, 25305–25316 (2013).

75. Xin, L. *et al.* Polybenzimidazole (PBI) Functionalized Nanographene as Highly Stable Catalyst Support for Polymer Electrolyte Membrane Fuel Cells (PEMFCs). *J. Electrochem. Soc.* **163**, F1228–F1236 (2016).

76. Sneed, B. T. *et al.* 3D Analysis of Fuel Cell Electrocatalyst Degradation on Alternate Carbon Supports. *ACS Appl. Mater. Interfaces* **9**, 29839–29848 (2017).

77. Şanli, L. I., Bayram, V., Yarar, B., Ghobadi, S. & Gürsel, S. A. Development of graphene supported platinum nanoparticles for polymer electrolyte membrane fuel cells: Effect of support type and impregnation-reduction methods. *Int. J. Hydrogen Energy* **41**, 3414–3427 (2016).

78. Arici, E., Kaplan, B. Y., Mert, A. M., Alkan Gursel, S. & Kinayyigit, S. An effective electrocatalyst based on platinum nanoparticles supported with graphene nanoplatelets and carbon black hybrid for PEM fuel cells. *Int. J. Hydrogen Energy* **44**, 14175–14183 (2019).

79. Han, S., Wu, D., Li, S., Zhang, F. & Feng, X. Porous graphene materials for advanced electrochemical energy storage and conversion devices. *Adv. Mater.* **26**, 849–864 (2014).

80. Yan, Z. *et al.* Progress in the preparation and application of three-dimensional graphene-based porous nanocomposites. *Nanoscale* **7**, 5563–5577 (2015).

81. Nardecchia, S., Carriazo, D., Ferrer, M. L., Gutiérrez, M. C. & Monte, F. Del. Three dimensional macroporous architectures and aerogels built of carbon nanotubes and/or graphene: Synthesis and applications. *Chem. Soc. Rev.* **42**, 794–830 (2013).

82. Zhou, X., Tang, S., Yin, Y., Sun, S. & Qiao, J. Hierarchical porous N-doped graphene foams with superior oxygen reduction reactivity for polymer electrolyte membrane fuel cells. *Appl. Energy* **175**, 459–467 (2016).

83. Liu, J., Takeshi, D., Sasaki, K. & Lyth, S. M. Defective Graphene Foam: A Platinum Catalyst Support for PEMFCs. *J. Electrochem. Soc.* **161**, F838–F844 (2014).

84. Karuppanan, K. K. *et al.* 3D-porous electrocatalytic foam based on Pt@N-doped graphene for high performance and durable polymer electrolyte membrane fuel cells. *Sustain. Energy Fuels* **3**, 996–1011 (2019).

85. Huo, C., Yan, Z., Song, X. & Zeng, H. 2D materials via liquid exfoliation: a review on fabrication and applications. *Sci. Bull.* **60**, 1994–2008 (2015).

86. Hernandez, Y. *et al.* High-yield production of graphene by liquid-phase exfoliation of graphite. *Nat. Nanotechnol.* **3**, 563–568 (2008).

87. Tristant, D. *et al.* Optical signatures of bulk and solutions of KC8 and KC24. *J. Appl. Phys.* **118**, 1–6 (2015).

88. Hof, F. & Pénicaud, A. Graphenide Solutions: A Chemical Platform for Nanoparticle-Nanocarbon Composites. *Chem. - A Eur. J.* **24**, 16246–16250 (2018).

89. Jaramillo, T. F. *et al.* Identification of Active Edge Sites for Electrochemical H2 Evolution from MoS2 Nanocatalysts. *Science (80-.).* **317**, 100–102 (2007).

90. Hof, F. *et al.* From Food Waste to Efficient Bifunctional Nonprecious Electrocatalyst. *Chem. - A Eur. J.* **23**, 15283–15288 (2017).

91. Solin, S. A. & Zabel, H. The physics of ternary graphite intercalation compounds. *Adv. Phys.* **37**, 87–254 (1988).

92. Lodge, M. T. J. H. *et al.* Multielement NMR studies of the liquid-liquid phase separation and the metal-to-nonmetal transition in fluid lithium- and sodium-ammonia solutions. *J. Phys. Chem. B* **117**, 13322–13334 (2013).

93. Ferrari, A. C. & Basko, D. M. Raman spectroscopy as a versatile tool for studying the properties of graphene. *Nat. Nanotechnol.* **8**, 235–246 (2013).

94. Tuinstra, F. & Koenig, J. L. Raman Spectrum of Graphite. *J. Chem. Phys.* **53**, 1126–1130 (1970).

95. Ferrari, A. C. *et al.* Raman spectrum of graphene and graphene layers. *Phys. Rev. Lett.* **97**, 1–4 (2006).

96. Caņcado, L. G. *et al.* General equation for the determination of the crystallite size La of nanographite by Raman spectroscopy. *Appl. Phys. Lett.* **88**, 2–5 (2006).

97. Howard, C. A., Dean, M. P. M. & Withers, F. Phonons in potassium-doped graphene : The effects of electron-phonon interactions , dimensionality , and adatom ordering. *Phys. Rev. B* **241404**, 1–4 (2011).

98. Ni, Z., Wang, Y., Yu, T. & Shen, Z. Raman spectroscopy and imaging of graphene. *Nano Res.* **1**, 273–291 (2008).

99. Yuan, W., Li, C., Li, D., Yang, J. & Zeng, X. Preparation of single- and few-layer graphene sheets using Co deposition on sic substrate. *J. Nanomater.* **2011**, (2011).

100. Stan, C. V., Beavers, C. M., Kunz, M. & Tamura, N. X-ray diffraction under extreme conditions at the advanced light source. *Quantum Beam Sci.* **2**, 1–33 (2018).

101. Katsaras, J. *et al.* Neutron and X-Ray Scattering from Isotropic and Aligned Membranes. in *Structure and Dynamics of Membranous Interfaces* 107–134 (John Wiley & Sons, Inc., 2014). doi:10.1002/9780470388495.ch5.

102. Bard, A. J. & Faulkner, L. R. *Electrochemical methods : fundamentals and applications*. (John Wiley & Sons, 2001).

103. Zhang, M. *et al.* Improved catalytic activity of cobalt core-platinum shell nanoparticles supported on surface functionalized graphene for methanol electro-oxidation. *Electrochim. Acta* **158**, 81–88 (2015).

104. Wang, D. *et al.* Structurally ordered intermetallic platinum-cobalt core-shell nanoparticles with enhanced activity and stability as oxygen reduction electrocatalysts. *Nat. Mater.* **12**, 81–87 (2013).

105. Mazzaro, R. *et al.* Uniform Functionalization of High-Quality Graphene with Platinum Nanoparticles for Electrocatalytic Water Reduction. *ChemistryOpen* **4**, 268–273 (2015).

106. Saadatkhah, N. *et al.* Experimental methods in chemical engineering: Thermogravimetric analysis—TGA. *Can. J. Chem. Eng.* **98**, 34–43 (2020).

107. Liu, M. *et al.* Carbon supported noble metal nanoparticles as efficient catalysts for electrochemical water splitting. *Nanoscale* **12**, 20165–20170 (2020).

108. Garsany, Y., Baturina, O. A., Swider-Lyons, K. E. & Kocha, S. S. Experimental methods for quantifying the activity of platinum electrocatalysts for the oxygen reduction reaction. *Anal. Chem.* **82**, 6321–6328 (2010).

109. Mabbott, G. A. An introduction to cyclic voltammetry. *J. Chem. Educ.* **60**, 697 (1983).

110. Brett, C. M. A. & Brett, A. M. O. *Electrochemistry - Principles , Methods , and Applications*. (1994). doi:10.1002/anie.199419892.

111. Gasteiger, H. A., Kocha, S. S., Sompalli, B. & Wagner, F. T. Activity benchmarks and requirements for Pt, Pt-alloy, and non-Pt oxygen reduction catalysts for PEMFCs. *Appl. Catal. B Environ.* **56**, 9–35 (2005).

112. Zhou, R., Zheng, Y., Jaroniec, M. & Qiao, S.-Z. Determination of the Electron Transfer Number for the Oxygen Reduction Reaction: From Theory to Experiment. *ACS Catal.* **6**, 4720–4728 (2016).

113. S Treimer, A Tanga & DC Johnson. A Consideration of the Application of Koutecky-Levich Plots in the Diagnoses of Charge-Transfer Mechanisms at Rotated Disk Electrodes. *Electroanalysis* **14**, 165–171 (2002).

114. Masa, J., Batchelor-McAuley, C., Schuhmann, W. & Compton, R. G. Koutecky-Levich analysis applied to nanoparticle modified rotating disk electrodes: Electrocatalysis or misinterpretation. *Nano Res.* **7**, 71–78 (2014).

115. Shinagawa, T., Garcia-esparza, A. T. & Takanabe, K. Insight on Tafel slopes from a microkinetic analysis of aqueous electrocatalysis for energy conversion. *Sci. Rep.* **5**, 13081 (2015).

116. Xu, S., Li, D. & Wu, P. One-pot, facile, and versatile synthesis of monolayer MoS2 /WS2 quantum dots as bioimaging probes and efficient electrocatalysts for hydrogen evolution reaction. *Adv. Funct. Mater.* **25**, 1127–1136 (2015).

117. Illathvalappil, R., Unni, S. M. & Kurungot, S. Layer-separated MoS 2 bearing reduced graphene oxide formed by an in situ intercalation-cum-anchoring route mediated by Co(OH) 2 as a Pt-free electrocatalyst for oxygen reduction. *Nanoscale* **7**, 16729–16736 (2015).

118. Wang, K. *et al.* Biomass-derived activated carbon as high-performance non-precious electrocatalyst for oxygen reduction. *RSC Adv.* **3**, 12039 (2013).

119. Ye, T. N., Lv, L. B., Li, X. H., Xu, M. & Chen, J. S. Strongly veined carbon nanoleaves as a highly efficient metal-free electrocatalyst. *Angew. Chemie - Int. Ed.* **53**, 6905–6909 (2014).

120. Arif, S. *et al.* Electrostatically regulated ternary-doped carbon foams with exposed active sites as metal-free oxygen reduction electrocatalysts†. *Nanoscale* 15–21 (2018) doi:10.1039/c8nr03527j.

121. Wang, L. *et al.* Porous Carbon-Supported Gold Nanoparticles for Oxygen Reduction Reaction: Effects of Nanoparticle Size. *ACS Appl. Mater. Interfaces* **8**, 20635–20641 (2016).

122. Ahmed, M. S., Lee, D.-W. & Kim, Y.-B. Graphene Supported Silver Nanocrystals Preparation for Efficient Oxygen Reduction in Alkaline Fuel Cells. *J. Electrochem. Soc.* **163**, F1169–F1176 (2016).

123. Suter, T. A. M. *et al.* Scalable sacrificial templating to increase porosity and platinum utilisation in graphene-based polymer electrolyte fuel cell electrodes. *Nanomaterials* **11**, (2021).

124. York, B. R. & Solin, S. A. Effect of composition on charge exchange, lattice expansion, and staging in potassium-ammonia graphite intercalation compounds. *Phys. Rev. B* **31**, 8206–8220 (1985).

125. Wirtz, L., Pichler, T. & Chaco, J. C. Terms of Use Manifestation of Charged and Strained Graphene Layers in the Raman Response of Graphite Intercalation Compounds. *ACS Nano* 9249–9259 (2013) doi:10.1021/nn403885k.

126. Malard, L. M., Pimenta, M. A., Dresselhaus, G. & Dresselhaus, M. S. Raman spectroscopy in graphene. *Phys. Rep.* **473**, 51–87 (2009).

127. Lee, D. S. *et al.* Raman Spectra of Epitaxial Graphene on SiC and of Epitaxial Graphene Transferred to SiO 2. *Nanoletters* **8**, 4320–4325 (2008).

128. Ferrari, A. C. Raman spectroscopy of graphene and graphite: Disorder, electron-phonon coupling, doping and nonadiabatic effects. *Solid State Commun.* **143**, 47–57 (2007).

129. Kim, T., Jung, C., Bose, R. & Yi, S. Cobalt encapsulated in the nitrogen and sulfur co-doped carbon nanotube supported platinum for the oxygen reduction reaction catalyst. *Carbon N. Y.* **139**, 656–665 (2018).

130. Zeng, L., Cui, X. & Shi, J. A facile strategy for ultrasmall Pt NPs being partially- embedded in N-doped carbon nanosheet structure for efficient electrocatalysis. *Sci. China Mater.* 1–10 (2018) doi:https://doi.org/10.1007/s40843-018-9283-1.

131. Tamas Varga, Agnes Timea Varga, Gergo Ballai, Henrik haspel, Akos Kukovecz, zoltan konya. One step synthesis of chlorine-free Pt / Nitrogen-doped graphene composite for oxygen reduction reaction. *Carbon N. Y.* **133**, 90–100 (2018).

132. Nesselberger, M. *et al.* The effect of particle proximity on the oxygen reduction rate of size-selected platinum clusters. *Nat. Mater.* **12**, 919–924 (2013).

133. Antolini, E. Graphene as a new carbon support for low-temperature fuel cell catalysts. *Appl. Catal. B Environ.* **123**–**124**, 52–68 (2012).

134. Hof, F. *et al.* Size Control of Nanographene Supported Iron Oxide Nanoparticles Enhances Their Electrocatalytic Performance for the Oxygen Reduction and Oxygen Evolution Reactions. *J. Phys. Chem. C* **123**, 20774–20780 (2019).

135. Shao, Y., Yin, G. & Gao, Y. Understanding and approaches for the durability issues of Pt-based catalysts for PEM fuel cell. *J. Power Sources* **171**, 558–566 (2007).

136. Mayrhofer, K. J. J. *et al.* Fuel cell catalyst degradation on the nanoscale. *Electrochem. commun.* **10**, 1144–1147 (2008).

137. Hof, F. *et al.* From Food Waste to Efficient Bifunctional Nonprecious Electrocatalyst SUpporting information. *Chem. - A Eur. J.* **23**, 15283–15288 (2017).

138. Garsany, Y., Ge, J., St-Pierre, J., Rocheleau, R. & Swider-Lyons, K. E. Analytical Procedure for Accurate Comparison of Rotating Disk Electrode Results for the Oxygen Reduction Activity of Pt/C. *J. Electrochem. Soc.* **161**, F628–F640 (2014).

139. Guo, S. & Sun, S. FePt nanoparticles assembled on graphene as enhanced catalyst for oxygen reduction reaction. *J. Am. Chem. Soc.* **134**, 2492–2495 (2012).

140. Zhang, C. *et al.* Single-Atomic Ruthenium Catalytic Sites on Nitrogen-Doped Graphene for Oxygen Reduction Reaction in Acidic Medium. *ACS Nano* **11**, 6930–6941 (2017).

141. He, D., Jiang, Y., Lv, H., Pan, M. & Mu, S. Nitrogen-doped reduced graphene oxide supports for noble metal catalysts with greatly enhanced activity and stability. *Appl. Catal. B Environ.* **132**–**133**, 379–388 (2013).

142. Fortunato, G. V., De Lima, F. & Maia, G. Oxygen-reduction reaction

strongly electrocatalyzed by Pt electrodeposited onto graphene or graphene nanoribbons. *J. Power Sources* **302**, 247–258 (2016).

143. Bai, S. *et al.* Etching approach to hybrid structures of PtPd nanocages and graphene for efficient oxygen reduction reaction catalysts. *Nano Res.* **8**, 2789–2799 (2015).

144. Suh, W. kyo, Ganesan, P., Son, B., Kim, H. & Shanmugam, S. Graphene supported Pt–Ni nanoparticles for oxygen reduction reaction in acidic electrolyte. *Int. J. Hydrogen Energy* **41**, 12983–12994 (2016).

145. Li, S. S. *et al.* Facile synthesis of PdPt@Pt nanorings supported on reduced graphene oxide with enhanced electrocatalytic properties. *ACS Appl. Mater. Interfaces* **6**, 10549–10555 (2014).

146. Seselj, N., Engelbrekt, C., Ding, Y., Hjuler, H. A. & Ulstrup, J. Tailored Electron Transfer Pathways in Au core / Pt shell – Graphene Nanocatalysts for Fuel Cells. *Adv. Energy Mater.* **1702609**, 1–12 (2018).

147. Daş, E., Alkan Gürsel, S., Işıkel Şanlı, L. & Bayrakçeken Yurtcan, A. Thermodynamically controlled Pt deposition over graphene nanoplatelets: Effect of Pt loading on PEM fuel cell performance. *Int. J. Hydrogen Energy* **42**, 19246–19256 (2017).

148. Barakat, N. A. M., El-Deen, A. G., Ghouri, Z. K. & Al-Meer, S. Stable N-doped & FeNi-decorated graphene non-precious electrocatalyst for Oxygen Reduction Reaction in Acid Medium. *Sci. Rep.* **8**, 1–11 (2018).

149. Liang, Y. *et al.* Co3O4 nanocrystals on graphene as a synergistic catalyst for oxygen reduction reaction. *Nat. Mater.* **10**, 780–786 (2011).

150. Zhang, S. *et al.* A Facile Method to Prepare Ultrafine Pd Nanoparticles Embedded into N-Doped Porous Carbon Nanosheets as Highly Efficient Electrocatalysts for Oxygen Reduction Reaction. *J. Electrochem. Soc.* **167**, 054508 (2020).

151. Wen, X. *et al.* Cu Nanoparticles Embedded in N-Doped Carbon Materials for Oxygen Reduction Reaction. *Chinese J. Chem.* cjoc.202000073 (2020) doi:10.1002/cjoc.202000073.

152. Sookhakian, M., Tong, G. B. & Alias, Y. In-Situ Electrodeposition of Rhodium nanoparticles Anchored on Reduced Graphene Oxide nanosheets as an Efficient Oxygen Reduction Electrocatalyst. *Appl. Organomet. Chem.* **34**, 1–11 (2020).

153. Ahmed, M. S., Begum, H. & Kim, Y. B. Iron nanoparticles implanted metal-organic-frameworks based Fe–N–C catalysts for high-performance oxygen reduction reaction. *J. Power Sources* **451**, 227733 (2020).

154. Xiong, Y. *et al.* Pt-Decorated, Nanocarbon-Intercalated, and N-Doped Graphene with Enhanced Activity and Stability for Oxygen Reduction Reaction. *ACS Appl. Energy Mater.* **3**, 2490–2495 (2020).

155. Park, C., Lee, E., Lee, G. & Tak, Y. Superior durability and stability

of Pt electrocatalyst on N-doped graphene-TiO2 hybrid material for oxygen reduction reaction and polymer electrolyte membrane fuel cells. *Appl. Catal. B Environ.* **268**, 118414 (2020).

156. Fortunato, G. V., Cardoso, E. S. F., Martini, B. K. & Maia, G. Ti/Pt–Pd-Based Nanocomposite: Effects of Metal Oxides on the Oxygen Reduction Reaction. *ChemElectroChem* **7**, 1610–1618 (2020).

157. Tong, Z. *et al.* Ultrathin and Coiled Carbon Nanosheets as Pt Carriers for High and Stable Electrocatalytic Performance. *Appl. Catal. B Environ.* **269**, 118764 (2020).

158. Ramakrishnan, S. *et al.* Ultrafine Pt Nanoparticles Stabilized by MoS 2 /N-Doped Reduced Graphene Oxide as a Durable Electrocatalyst for Alcohol Oxidation and Oxygen Reduction Reactions. *ACS Appl. Mater. Interfaces* **11**, 12504–12515 (2019).

159. Song, X. *et al.* Promotion of hydrogen peroxide production on graphene-supported atomically dispersed platinum: Effects of size on oxygen reduction reaction pathway. *J. Power Sources* **435**, 226771 (2019).

160. Kim, Y. *et al.* Enhanced electrochemical oxygen reduction reaction performance with Pt nanocluster catalysts supported on microporous graphene-like 3D carbon. *J. Electroanal. Chem.* **838**, 89–93 (2019).

161. Bertin, E. *et al.* Durability study of platinum nanoparticles supported on gas-phase synthesized graphene in oxygen reduction reaction conditions. *Appl. Surf. Sci.* **467**–**468**, 1181–1186 (2019).

162. Yan, Y., Yan, S., Yu, Z. & Zou, Z. Low-Work-Function Silver Activating N-doped Graphene as Efficient Oxygen Reduction Catalysts in Acidic Medium. *ChemCatChem* **11**, 1033–1038 (2019).

163. Wang, J. *et al.* A facile preparation of nano-Ag4Bi2O5/MnOx on wrinkled rGO as greatly enhanced ternary catalyst for oxygen reduction reaction in alkaline electrolyte. *J. Solid State Electrochem.* **23**, 2737–2746 (2019).

164. Bai, L., Hou, C., Wen, X. & Guan, J. Catalysis of Oxygen Reduction Reaction on Atomically Dispersed Copper- And Nitrogen-Codoped Graphene. *ACS Appl. Energy Mater.* **2**, 4755–4762 (2019).

165. Kong, F. D. *et al.* Fabrication of Pt/IrO2Nb2O5–rGO Electrocatalyst by Support Improvement for Oxygen Reduction Reaction. *Catal. Letters* **149**, 3041–3047 (2019).

166. Khan, K. *et al.* Fe-doped mayenite electride composite with 2D reduced Graphene Oxide: As a non-platinum based, highly durable electrocatalyst for Oxygen Reduction Reaction. *Sci. Rep.* **9**, 1–11 (2019).

167. Boone, C. V. & Maia, G. Lowering metal loadings onto Pt–Pd–Cu/graphene nanoribbon nanocomposites affects electrode collection efficiency and oxygen reduction reaction performance. *Electrochim. Acta* **303**, 192–203 (2019).

168. Hota, I. *et al.* Mn-doped ceria/reduced graphene oxide nanocomposite as an efficient oxygen reduction reaction catalyst. *J. Electroanal. Chem.* **851**, 113480 (2019).

169. Zheng, Y. *et al.* Nitrogen-Doped Carbon Nanotube-Graphene Frameworks with Encapsulated Fe/Fe3N Nanoparticles as Catalysts for Oxygen Reduction. *ACS Appl. Nano Mater.* **2**, 3538–3547 (2019).

170. Lim, D., Shim, Y., Oh, J., Kim, S. & Park, S. Well-dispersed Pt nanoparticles on borane-modified graphene oxide and their electrocatalytic performance for oxygen reduction reaction. *J. Solid State Chem.* **271**, 168–174 (2019).

171. Liu, Z. *et al.* Pt/graphene with intercalated carbon nanotube spacers introduced by electrostatic self-assembly for fuel cells. *Mater. Chem. Phys.* **225**, 371–378 (2019).

172. Zhong, H. X. *et al.* ZIF-8 derived graphene-based nitrogen-doped porous carbon sheets as highly efficient and durable oxygen reduction electrocatalysts. *Angew. Chemie - Int. Ed.* **53**, 14235–14239 (2014).

173. Meng, F. L. *et al.* Reactive Multifunctional Template-Induced Preparation of Fe-N-Doped Mesoporous Carbon Microspheres Towards Highly Efficient Electrocatalysts for Oxygen Reduction. *Adv. Mater.* **28**, 7948–7955 (2016).

174. Smith, M. & Savinell, R. F. MICRO FUEL CELLS. *The Electrochemical Society: Electrochemistry Encyclopedia* (2013).

175. Katsaras, J. *et al.* Neutron and X-Ray Scattering from Isotropic and Aligned Membranes. in *Structure and Dynamics of Membranous Interfaces* 107–134 (John Wiley & Sons, Inc., 2014). doi:10.1002/9780470388495.ch5.

Appendix: Literature Review Table

The table below presents a review of corrosion protocols and their results, tested at half-cell level, presented in a range of papers describing graphene-supported catalysts for the ORR.

Ref.	Catalyst	AST protocol	AST length	Sample stability	Pt/C Stability
This work	GD-Pt/G	0.6-1 V vs RHE, 100 mV/s	30,000 cycles	21 % in ECSA	30 % loss in ECSA
		1-1.6 V vs RHE, 100 mV/s	30,000 cycles	19 % loss in ECSA	50 % loss in ECSA
[47]	Pt/functionalised graphene	0.6 - 1V vs RHE, 50 mV/s	5000 cycles	37.6 % loss in ECSA	60 % loss in ECSA
[139]	FePt/rGO	0.4 - 0.8 V vs Ag/AgCl, 100 mV/s	10,000 cycles	Almost no change in ORR activity	"Left shifted"
[140]	Ru/N-doped graphene	0.6 - 1V vs RHE, 100mV/s	10,000 cycles	7 % decrease in limiting current, 18mV negative shift in half-wave potential	N.A.
		Chronoamperometric measuremen	10,000 s	10 % loss in current density at 0.7V vs RHE	38 % loss in current density at 0.7 V vs RHE

Appendix: Literature Review Table

		t at 0.7V vs RHE			
[48]	Au cluster/rGO	Chronoamperometric measurement at -0.2 V vs Ag/AgCl	40,000 s	16% loss in current density at -0.2 V vs Ag/AgCl	50 % loss in current density at -0.2 V vs Ag/AgCl
[122]	Ag nanocrystals/ rGO	Potential window not specified, 50 mV/s	1000 cycles	15.6 % loss in ECSA	63.1 % loss in ECSA
[49]	Pd/rGO	Chronoamperometric measurement at 0.63 V vs RHE	2000 s	ca. 93 % loss in current density at 0.63 V vs RHE	ca. 98 % loss in mass current density at 0.63 V vs RHE
		0.36 - 0.86 V vs RHE	4000 cycles	"little change in the ORR activity was observed"	N.A.
[141]	Pt/N-doped rGO	0.6 - 1.2 V vs RHE	4000 cycles	29.4 % loss in ECSA	80.8 % loss in ECSA
[50]	PtPd NPs/ rGO	Chronoamperometric measurement at 0.1 V vs RHE	10,000 s	ca. 24 % loss in current density at 0.1 V vs RHE	ca. 48 % loss in current density at 0.1 V vs RHE

Appendix: Literature Review Table

[142]	Pt/GO nanoribbons	0.6 - 1 V vs RHE, 50 mV/s	10,000 cycles	65 % loss in ECSA	N.A.
[143]	PtPd nanocage/rGO	0.6 - 1.05 V vs RHE, 50 mV/s	10,000 cycles	11.3 % loss in ECSA	N.A.
[51]	Cu-Pd/ rGO	Neither potential window nor scan speed not specified	3000 cycles	8.8 % decrease in ORR limiting current	15.6 % decrease in ORR limiting current
[52]	Au clusters/ rGO	-1 -0.2 V vs Ag/AgCl, 5 mV/s	1000 cycles	16 % loss in ECSA	27 % loss in ECSA
[144]	PtNi/rGo	-0.2 - 1.2 V vs RHE, 50 mV/s	2000 cycles	96.6 % loss in ECSA	N.A.
[145]	PdPt@Pt/rGO	Neither potential window nor scan speed not specified	1000 cycles	40 % loss in ECSA	N.A.
[130]	Pt/ carbon nanosheets	0.46-0.96V vs RHE, 50 mV/s	5000 cycles	25 mV negative shift of half wave potential	36 mV negative shift of half wave potential
[146]	Au@Pt/rGO	N.A. (single cell tests, no RDE ASTs)	N.A.	N.A.	N.A.

Appendix: Literature Review Table

[131]	Pt/N-doped GO	No durability tests	N.A.	N.A.	N.A.
[26]	Graphene capped Pt	0.4-0.75 V vs Ag/AgCl, scan rate not specified	1000 cycles	No change in ECSA after 1000 cycles	N.A. Pt monolayer they grew themselves: ca. 45 % loss in ECSA
[28]	Pt/rGO/ Carbon black	0.6- 1.1 V vs RHE, scan rate not specified	20,000 cycles	5 % loss in ECSA	51 % loss in ECSA
[147]	Pt/Graphene nanoplatelets	Chronoamperometric measurement at 1.2 V vs RHE	86,400 0 s	35.4 % loss in current density	N.A.
[148]	FeNi/ N-doped rGO	-0.2 – 1 V vs Ag/AgCl, 50 mV/s	1000 cycles	CVs shown but ECSA change not quantified	Bigger change in ECSA than for Pt/N-doped rGO
[149]	Co_3O_4 nanocrystals/ rGO	Chronoamperometric measurement at 0.7 V vs RHE	25,000 s	0 % loss in current density at 0.7 V vs RHE	35 % loss in current density at 0.7 V vs RHE
[56]	Pt/SiC/rGO	0.6-1.2 V vs RHE, scan	10,000 cycles	59.7 % loss in ECSA	79.3 % loss in ECSA

Appendix: Literature Review Table

		rate not specified			
[54]	Pt/rGO/ carbon fiber	-0.2-0.96 V vs SCE, 50 mV/s	1500 cycles	81.9 % loss in ECSA	86.4 % loss in ECSA
[53]	Pt/rGO	0-1.2 V vs RHE, scan rate not specified	10,000 cycles	68 % loss in ECSA	N.A.
[150]	Pd/N-carbon nanosheet	Chronoamperometric measuerment at 0.6 V vs RHE	35,000 s	20 % loss in current density at 0.6 V vs RHE	33 % loss in current density at 0.6 V vs RHE
[151]	Cu/N-rGO	Chronoamperometric measurement at 0.7 V vs RHE	1200s	Ca. 0% loss in current density at 0.7 V vs RHE	Ca. 50 % loss in current density at 0.7V vs RHE
[152]	Rh/rGO	Chronoamperometric measurement at unspecified potential	25,000s	10.9 % loss in current density	47.5 % loss in current density
[153]	Fe@PANI/rGO	0.2 – 1.2 V vs RHE, 50 mV/s	10,000 cycles	13 mV decrease in $E_{1/2}$	82 mV decrease in $E_{1/2}$
[154]	Pt/N-rGO + carbon	0.5 – 1 V vs RHE, scan	5000 cycles	6% loss in ECSA	40.2 % loss in ECSA

Appendix: Literature Review Table

	nanospheres	rate not specified			
[155]	Pt/N-doped TiO_2 + N-doped rGO	1 - 1.5 V vs RHE, 500 mV/s scan rate	20,000 cycles	16.9% loss in ECSA	40.1% loss in ECSA
[156]	Ti/Pt-Pd/ Graphene nanoribbons	0.4 – 1.0 V vs RHE, 1 V/s	10,800 cycles	ECSA "does not vary"	6 % loss in ECSA
		1 – 1.5 V vs RHE, 500 mV/s	5000 cycles	9.7 % loss in ECSA	N.A.
[157]	Pt/coiled carbon nanosheets	Chronoamperometric measurement at 0.68 V vs RHE	3500 s	Ca. 85% loss in current density measured at 0.68 V vs RHE	Ca. 100% loss in current density measured at 0.68 V vs RHE
[158]	Pt@MoS_2/N-rGO	0.6 – 1.0 V vs RHE, 100 mV/s	30,000 cycles	23.06 % loss in ECSA	28.02 % loss in ECSA
[159]	Pt single atoms/rGO	0.4 – 1.0 V vs RHE, 50 mV/s	2000 cycles	0.025 V negative shift in $E_{1/2}$	N.A.
[160]	Pt/ graphene-like 3D carbon	Chronopotentiometry at -3.016 mA/cm^2	7200 s	10 % decrease in mass activity at 0.8 V vs RHE	39.2 % decrease in mass activity at 0.8 V vs RHE

Appendix: Literature Review Table

[161]	Pt/graphene	0.6 - 1 V, 100 mV/s, followed by 0.6 – 1.5 V,	18,000 cycles, followed by 800 cycles	5% loss in ECSA, followed by a further 20% loss	40% loss in ECSA followed by a further 22% loss
[162]	Ag/N-doped graphene	-0.1 – 1 V, 50 mV/s	10,000 cycles	22 mV negative shift in $E_{1/2}$	86 mV negative shift in $E_{1/2}$
[84]	Pt/ N-doped rGO foam	Chronoamperometric measurement at 0.6 V vs RHE	30,000 s	14.4 % decrease in current density measured at 0.6 V vs RHE	33.1 % decrease in current density measured at 0.6 V vs RHE
		0.05 – 1.2 V vs RHE, 50 mV/s	10,000 cycles	24 mV negative shift in $E_{1/2}$	75 mV negative shift in $E_{1/2}$
[163]	$Ag_4Bi_2O_5/MnO_x$-rGO	Chronoamperometric measurement at 0.03 V vs Hg/HgO	10,800 s	14 % decrease in current density measured at 0.03 V vs Hg/HgO	42 % decrease in current density measured at 0.03 V vs Hg/HgO
[164]	Cu/N-doped rGO	Chronoamperometric measurement at 0.7 V vs RHE	25,000 s	4 % decrease in current density measured at 0.7 V vs RHE	19.5 % decrease in current density measured at 0.7 V5

Appendix: Literature Review Table

					vs RHE
[165]	Pt/$IrO_2Nb_2O_5$ - rGO	0.0 – 1.2 V vs RHE, 50 mV/s	2000 cycles	23.8 % loss in ECSA	39.4 loss in ECSA
[166]	Fe-doped mayenite/rGO	Chronoamperometric measurement at 0.87 V vs RHE	39,600 s	Current density "almost remains the same"	40 % decrease in current density measured at 0.87 V vs RHE
[167]	Pt-Pd-Cu/graphene nanoribbon	0.6 – 1 V vs RHE, 50 mV/s	10,000 cycles	Ca. 30 % decrease in mass activity	N.A.
[168]	Mn doped CeO_2/rGO	Chronoamperometric measurement at -0.35 V vs Ag/AgCl	12,500 cycles	20 % decrease in current density measured at-0.35 V vs Ag/AgCl	40% decrease in current density measured at-0.35 V vs Ag/AgCl
[169]	Fe-N-CNT/rGO	Chronoamperometric measurement at 0.8 V vs RHE	72,000 s	6 % decrease in current density measured at 0.8 V vs RHE	29 % decrease in current density measured at 0.8 V vs RHE
[170]	Pt/B-rGO	0.57 – 1.17 V vs RHE,	6000 cycles	Onset and half wave	N.A.

Appendix: Literature Review Table

		scan rate not specified		potential "close to initial cycle"	
[171]	Pt/rGO + CNT spacers	0 – 1.2 V vs RHE, 50 mV/s	2000 cycles	39 % loss in ECSA	19% loss in ECSA
[172]	ZIF-N-rGO porous nanosheets	Chronoamperometric measurement at -0.4 V vs Ag/AgCl	28,000 s	6 % decrease in current density measured at -0.4 V vs Ag/AgCl	20 % decrease in ECSA measured at -0.4 V vs Ag/AgCl
[173]	Fe-N-C microspheres	0.55 – 0.95 V vs RHE, 100 mV/s	10,000 cycles	29 mV negative shift in $E_{1/2}$	31 mV negative shift in $E_{1/2}$

Table A1│ A review of graphene supported catalysts for ORR, their associated accelerated stress test protocols, and results.